WIDE FIELD-OF-VIEW MICROSCOPES AND ENDOSCOPES FOR TIME-LAPSE IMAGING AND HIGHT-THROUGHPUT SCREENING

Thesis by
Chao Han

In Partial Fulfillment of the Requirements for the Degree
of
Doctor of Philosophy

CALIFORNIA INSTITUTE OF TECHNOLOGY
Pasadena, California
2015
(Defended Jan 27, 2015)

ACKNOWLEDGEMENTS

I would like to express my sincere gratitude to my advisor, Professor Changhuei Yang, for his guidance and advice during the past five years. Throughout my Ph.D. study in his Biophotonics Lab, I have been deeply inspired by his passion in scientific research and creative thinking for innovation. I also learned a lot from his broad vision in cross-disciplinary research, and I was very fortunate to have the chance to collaborate with great biologists and doctors in various capacities under his guidance. He has always been very supportive and available for all kinds of discussions, and always provides me the freedom and resources encouraging me to try out new ideas.

I would like to express my thanks to Professor Lily Lai for her guidance and collaboration on the wide field-of-view endoscope projects. Dr. Lai is very knowledgeable and helped me in both medical knowledge learning and hands-on experiments. I also learn a lot from her in how to design and fabricate medical devices to address clinical needs. Her passion and optimistic attitude towards research have always inspired me.

I would also like to thank Professor Yu-Chong Tai, Professor Rustem Ismagilov, Professor Hyuck Choo, and Professor Long Cai for being my thesis and/or candidacy committee. They provided me with many insightful thoughts and suggestions for the improvement of my work.

I would like to thank Professor Paul Sternberg and his lab members for the exciting collaboration in the fluorescence imaging of *C. elegans* using the Talbot microscope. Dr. Sternberg was very kind in making himself available for helping us with the experimental plan and manuscript preparation. Dr. Mihoko Kato kindly helped us in the design of the *C. elegans* experiments and the preparation of *C. elegans* samples. I would also like to thank Professor Scott Fraser for the use of his lab facilities, and Danielle Bower for helping us prepare the GFP cell lines for our longitudinal imaging experiment using the Talbot microscope. I would like to thank Dr. Karen Lencioni, Dr. Janet Baer, and their colleagues for helping us taking care of animal model experiments in our AnCam project.

I would like to specially thank two teammates I closely worked with in my Ph.D years: Dr. Shuo Pang and Professor Jiangtao Huangfu. I worked with Shuo from the beginning of my Ph.D study, and during the two years we worked as a team we finished the fluorescence optofluidic microscope and Talbot microscope projects. We overcame all the difficulties and enjoyed every successful moment together. Also, I have learned a lot from his profound knowledge in optics. I collaborated with Huangfu for the AnCam and PanCam endoscope projects, and I have always been amazed by

his broad knowledge and vision. He is very resourceful and taught me much about hardware instrumentation, and I had a great time working with him.

I am grateful for the help and companionship of all the members of the Biophotonics Lab at Caltech, including Dr. Jigang Wu, Dr. Lap Man Lee, Dr. Jian Ren, Dr. Guoan Zheng, Dr. Yangmin Wang, Dr. Seung Ah Lee, Dr. Benjamin Judkewitz, Mooseok Jang, Dr. Phil Williams (ePetri Inc.), Daniel Tran (ePetri Inc.), Xiaoze Ou, Roarke Horstmeyer, Haojiang Zhou, Jinho Kim, Dr. Haowen Ruan, Dr. Jaehee Jung, Albert Chung, Dr. Daifa Wang, Hao Deng, Joshua Brake, and Patrick Yiu. Xiaoze Ou , Daniel Tran, and Dr. Phil Williams helped me with the hardware and software debugging for the ePetri prototypes. Dr. Jaehee Jung collaborated with me for the infrared laser-controlled micro-actuators project, and I really enjoyed sharing all the happy moments with him. Patrick did a good job in helping with the cell segmentation and tracking software. I would like to thank all of them for their generous help and insightful discussions.

I would like to express my thanks to our lab manager, Anne Sullivan. She does an amazing job maintaining our lab, and I have always been taken good care of in every aspect. I would also like to thank Tanya Owen, Christine Garske, Carol Sosnowski, and Janet Couch for their administrative assistance and their help with processing our lab orders.

Finally, I would like to thank my family, especially my parents. Studying outside my city and outside my country for so many years, I am always feeling that I have so little time to be with them. It is their love that always supports me and keeps me moving forward.

ABSTRACT

Wide field-of-view (FOV) microscopy is of high importance to biological research and clinical diagnosis where a high-throughput screening of samples is needed. This thesis presents the development of several novel wide FOV imaging technologies and demonstrates their capabilities in longitudinal imaging of living organisms, on the scale of viral plaques to live cells and tissues.

The ePetri Dish is a wide FOV on-chip bright-field microscope. Here we applied an ePetri platform for plaque analysis of murine norovirus 1 (MNV-1). The ePetri offers the ability to dynamically track plaques at the individual cell death event level over a wide FOV of 6 mm × 4 mm at 30 min intervals. A density-based clustering algorithm is used to analyze the spatial-temporal distribution of cell death events to identify plaques at their earliest stages. We also demonstrate the capabilities of the ePetri in viral titer count and dynamically monitoring plaque formation, growth, and the influence of antiviral drugs.

We developed another wide FOV imaging technique, the Talbot microscope, for the fluorescence imaging of live cells. The Talbot microscope takes advantage of the Talbot effect and can generate a focal spot array to scan the fluorescence samples directly on-chip. It has a resolution of 1.2 μm and a FOV of ~13 mm^2. We further upgraded the Talbot microscope for the long-term time-lapse fluorescence imaging of live cell cultures, and analyzed the cells' dynamic response to an anticancer drug.

We present two wide FOV endoscopes for tissue imaging, named the AnCam and the PanCam. The AnCam is based on the contact image sensor (CIS) technology, and can scan the whole anal canal within 10 seconds with a resolution of 89 μm, a maximum FOV of 100 mm × 120 mm, and a depth-of-field (DOF) of 0.65 mm. We also demonstrate the performance of the AnCam in whole anal canal imaging in both animal models and real patients. In addition to this, the PanCam is based on a smartphone platform integrated with a panoramic annular lens (PAL), and can capture a FOV of 18 mm × 120 mm in a single shot with a resolution of 100─140 μm. In this work we demonstrate the PanCam's performance in imaging a stained tissue sample.

TABLE OF CONTENTS

LIST OF ILLUSTRATIONS AND/OR TABLES

Page

LIST OF FREQUENTLY USED ACRONYMS

Acronym	**Full name**
2CMC	2’-C-methylcytidine
CCD	Charge-coupled device
CCTV	Closed-circuit television
C. elegans	*Caenorhabditis elegans*
CIS	Contact image sensor
CMOS	Complementary metal–oxide–semiconductor
CPE	Cytopathic effect
CPT	Camptothecin
DBSCAN	Density-based spatial clustering of applications with noise
DOF	Depth of field
DSLR	Digital single-lens reflex
DTC	Distal tip cell
FFC	Flexible flat cable
FFT	Fast Fourier transform
FOV	Field of view
FWHM	Full-width at half maximum
GFP	Green fluorescent protein
HER2	Human epidermal growth factor receptor-2
HR	High-resolution
IDE	Integrated development environment

LED	Light-emitting diode
lp	Line pair
LR	Low-resolution
MLA	Microlens array
MNV-1	Murine norovirus 1
MTF	Modulation transfer function
N.A.	Numerical aperture
NoV	Norovirus
OD	Optical density
OTF	Optical transfer function
PAL	Panoramic annular lens
PDMS	Poly(dimethylsiloxane)
PFU	Plaque forming units
PLA	Polylactide
PMMA	Poly(methyl methacrylate)
PSF	Point spread function
RNAi	RNA interference
SBP	Space-bandwidth product
SLA	SELFOC® lens array
SLM	Spatial light modulator
SVM	Support vector machine
TEC	Thermoelectric cooler
TIR	Total internal reflection

C h a p t e r 1

INTRODUCTION

Optical microscopy has been one of the most important tools in biological research and modern clinical diagnosis. However, since its invention in the 16th century, the basic structure of the optical microscope has not changed too much from its original design. Because of its limited field-of-view (FOV), bulky size, and high cost, conventional microscopy is now becoming a bottleneck in rapidly emerging and evolving areas in life science, pharmaceutical development, and point-of-care diagnosis, where a low-cost, wide-FOV, high-resolution imaging solution is needed for the longitudinal study of living cells or tissues, such as high-throughput genetic screening [1] and time-lapse live cell imaging [2].

In this chapter, we will first review the imaging principles of conventional optical microscopes and endoscopes. We will then discuss the basic properties of the microscopes and the limitations of conventional microscopes corresponding to these properties. Next, we will review the modern wide FOV microscopy technologies. Finally, we will introduce our approach and outline the structure of this thesis.

1.1 Conventional microscopes

A microscope is an instrument that can provide magnified images of small objects that cannot be resolved by the naked eye. Although it is not easy to identify the first inventor of the optical microscope, the wide-spread use of the microscope started between the 1660s and 1670s. During this period of time, Robert Hooke published his book *Micrographia* in England, illustrating microscopic structures such as plant cells [3], while Dutch scientist Antonie van Leeuwenhoek also built microscopes that led to his discovery of many micro-organisms, including bacteria and sperm cells. Figure 1.1 shows a microscope made in France in 1751 and now exhibited in the Getty Center Los Angeles, which contains an objective lens, an eyepiece, an ocular micrometer, and a micrometric stage; also different lenses can be replaced to change magnifications. Over the centuries, a vast number of technological and manufacturing improvements have been made to improve the image quality of the microscope, however, the basic principle of the optical microscope we are using today is not much different from those early microscopes.

Figure 1.1. A microscope with replaceable lenses. This microscope was made in France around 1751 and is now exhibited in the Getty Center Los Angeles. (a) The microscope body. (b) Replaceable lenses.

The basic structure of a modern infinite-corrected microscope is illustrated in Figure 1.2. It consists of a light source, an objective lens, a tube lens, and an image sensor. The sample is illuminated by the light source and placed at the front focal plane of the objective, and an image is created at infinity behind the objective. The tube lens re-projects this image from infinity to the image plane to generate a magnified image. This image is then captured and read out by the image sensor. The objective is the central part of the microscope, since it determines the most important properties of the microscope, including resolution and field-of-view (FOV).

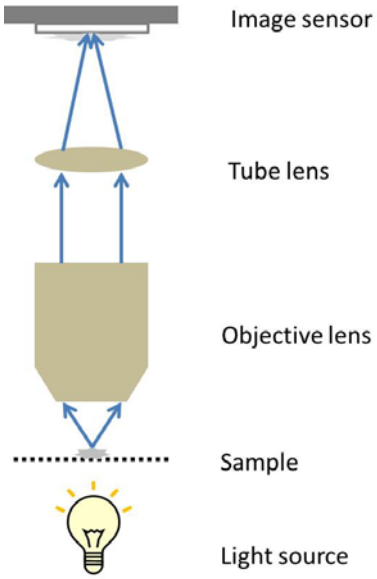

Figure 1.2. The basic setup of a conventional infinite-corrected microscope. It consists of a light source, an objective lens, a tube lens, and an image sensor.

1.2 Characteristics of a microscopic imaging system

There are many properties describing the capabilities of a microscopic imaging system to correctly recover the information from the sample. They include resolution, FOV, depth-of-field (DOF), aberrations, etc. For the scope of this thesis, we will only discuss resolution, FOV, and their relationship in detail.

1.2.1 Resolution

Resolution describes a microscope's ability to resolve details inside a given sample. In an aberration-free microscope system the optical resolution is determined by diffraction: a point source at the object plane generates a diffraction pattern at the image plane consisting of a central spot surrounded by a series of concentric diffraction rings. This pattern is named an Airy disk. Therefore, the resolution of the microscope is just the minimum separation distance of two Airy disks at the point at which they can still be distinguished. Ernst Abbe first established a resolution equation in 1873 based on the radius of the Airy disk [4]:

$$Abbe\ Resolution = \frac{\lambda}{2\ N.A.} \tag{1—1}$$

where λ is the wavelength and N.A. is the numerical aperture of the objective, which is defined as:

$$N.A. = n \cdot sin\theta \tag{1—2}$$

where n is the refractive index of the medium between the sample and the objective lens, and θ is one-half of the objective angular aperture (Figure 1.3).

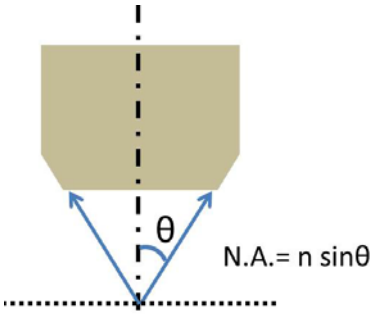

Figure 1.3. Numerical Aperture (N.A.) of a microscope objective

Lord Rayleigh refined this resolution in 1896 in a more quantitative way: two points are regarded as being resolved by the microscope if the center of one Airy disk overlaps with the first minimum of the other Airy disk:

$$Rayleigh\ Resolution = \frac{0.61\,\lambda}{N.A.} \tag{1—3}$$

This equation was derived due to the fact that the Airy disk comes from the Fraunhofer diffraction pattern of a circular aperture, and number 0.61 comes from a calculation of the first zero of a Bessel function contained in the intensity profile of the Fraunhofer diffraction pattern.

In order to establish the optical resolution, two methods are widely used. The first method is to measure the point spread function (PSF) or optical transfer function (OTF) of the system; the second one is to directly image a test target and read out the minimal discernible pattern in it. It is worth noting that the optical resolution we discussed so far is only for an aberration-free system, and the resolution can be deteriorated with the existence of an aberration. One should also notice that the overall resolution of an optical imaging

system depends on the pixel resolution of the image sensor as well, which we will cover in Section 1.2.1.3.

1.2.1.1 Optical Resolution Measurement using Point Spread Function (PSF) and Optical Transfer Function (OTF)

In the section above we discussed the Airy disk, which is actually an observation of the PSF in the microscope imaging system. By definition, the PSF is the response of an imaging system to a point source. Therefore, for an imaging system, the image is the convolution of the object with the PSF. This convolution introduces blur into the image. The sharper the PSF is, the less blur will be introduced, and the higher resolution the image will have. Therefore, the full width at half maximum (FWHM) of the PSF is often used to define the system's resolution.

For measuring the PSF, point source-like samples are often used. For example, microspheres with known diameters much smaller than the estimated resolution will be a good choice. After adjusting the sample in focus, the image of the sample can be obtained and its intensity profile can be treated as the PSF.

On the other hand, the OTF is defined as the Fourier transform of PSF. In frequency domain, the image can be simply expressed as the object multiplied by the OTF. It describes the imaging system's response to different frequency components. It is easy to discover that an imaging system acts like a low-pass filter: the amplitude of OTF drops as the frequency increases, so that the system does not have enough response at too high frequencies (as it cannot resolve too small patterns in spatial domain). The amplitude of OTF is called the modulation transfer function (MTF). Ultimately, the cutoff frequencies for a certain MTF value can also be used to establish the resolution.

To measure the MTF, a test chart having line patterns with continuously changing frequencies is often used. An MTF curve can be plotted by calculating the contrast of the image at different line frequencies. The frequency where its MTF drops to 10% of its maximum value is often treated as the cutoff frequency and labeled MTF10. Converting this frequency back into its spatial size will give the spatial resolution of the system.

It should also be noted that this thesis's scope is incoherent imaging, so the PSF and OTF discussed here are only the intensities. For coherent systems, PSF and OTF will be complex functions and therefore we have to consider both the intensity and the phase during the calculation. Although in Chapter 3 we used coherent light (laser) for fluorescence excitation, the fluorescence emission is still incoherent, so we are still working with an incoherent imaging system.

Figure 1.4 summarizes the relationship of the object, image, PSF, and OTF in spatial and frequency domain. g_{OBG} and G_{OBG} represent the object in spatial and frequency domain, respectively, and g_{IMG} and G_{IMG} represent the object in spatial and frequency domain, respectively. (x,y) are the coordinates in spatial domain, and (u,v) are the coordinates in the angular spectrum in frequency domain.

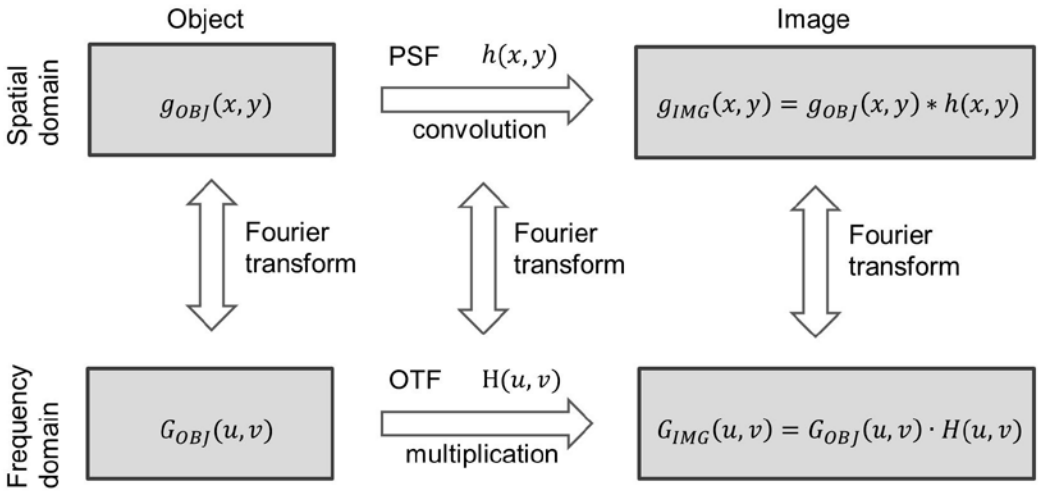

Figure 1.4. Relationship between PSF and OTF

1.2.1.2 Resolution Measurement using Test Targets

Besides the PSF/OTF measurement, standard test targets with patterns of known sizes are often used to directly read out the resolution limit of the microscopic system. There are many choices of test targets, such as the USAF 1951 target, NBS 1952 target, NBS 1010a target, etc. Among them, the USAF 1951 target has been widely used in microscopy and also in our thesis, so we will describe its principle in detail. The USAF 1951 target consists of horizontal and vertical bars organized in groups and elements. There are twelve groups

in total (numbered from -2 to 9). Each group has six elements (numbered from 1 to 6). Each element is composed of three equal-spaced horizontal and vertical bars, respectively, and the length of each bar is equal to five times its width (Figure 1.5). The size of the bars decreases as the group and element number increase. Vertical bars are for horizontal resolution measurement, and horizontal bars are for vertical resolution measurement. One line pair (lp) is defined as the spacing between the center of two bars (shown as 'd' in Figure 1.5). The resolution can be defined either in frequency domain using maximally discernible lp per mm, or in spatial domain using minimally discernible spacing of two bars. It should be noted that it is the spacing (d) instead of the width (x) of the bars that defines the resolution.

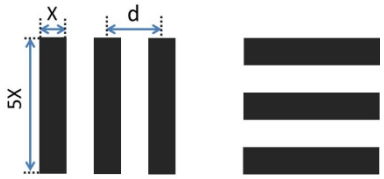

Figure 1.5. An element of the USAF 1951 target

Qualitatively, the resolution of an imaging system is calculated as the group and element combination of the smallest discernible pattern. The resolution (in terms of line pairs per millimeter, or lp/mm) can be calculated by:

$$Resolution = 2^{G+\frac{E-1}{6}} \tag{1—4}$$

where G is the group number and E is the element number. For instance, if the smallest discernible pattern is Group 3 element 4, then the resolution of the system can be calculated as $2^{3+\frac{4-1}{6}} = 11.3\,\mathrm{lp/mm}$. To convert this spatial resolution, we can simply take the reciprocal of this number, which is 1/11.3 mm=0.0885 mm=88.5 μm.

It is worth noting that the USAF 1951 target can only support resolution measurement down to 1.56 μm. If an imaging system has higher resolution beyond this target, then smaller bars can be custom fabricated using a similar style.

1.2.1.3 Resolution of the image sensor

As discussed in Section 1.2.1.1 and 1.2.1.2, the diffraction-limited optical resolution can be measured using either PSF/OTF measurement or test targets. However, this optical resolution may not necessarily be the overall resolution of the imaging system, since the pixel resolution of the image sensor also has to be taken into account.

It is worth noting that all the digital images are captured by the pixelated image sensor, so they are the discretely sampled version of the original image. In order to maintain the optical resolution as the image system's resolution, one has to make sure that the sensor pixel is able to sample the size of the optical resolution without aliasing**.** According to the Nyquist sampling theorem, this requires the pixel size to be no larger than half of the resolution.

This concept is illustrated in Figure 1.6. We can consider that two bars on the USAF 1951 target are imaged onto an image sensor. When the sensor pixel size is larger than half of the resolution (Figure 1.6a), even if the two bars can be optically resolved by the lens, they can still be projected onto adjacent pixels on the image sensor, and thus cannot be resolved by the imaging system. In this case, the images of the two bars need to have a separation of at least two pixels in order to be resolved by the image sensor (Figure 1.6b), so that the overall resolution of the image system is determined by the image sensor instead of the optics. By increasing the sensor's pixel density, the imaging system can now achieve its optical resolution (Figure 1.6c). Therefore, it is necessary to verify both the optical resolution and the sensor's pixel resolution when designing a microscope imaging system.

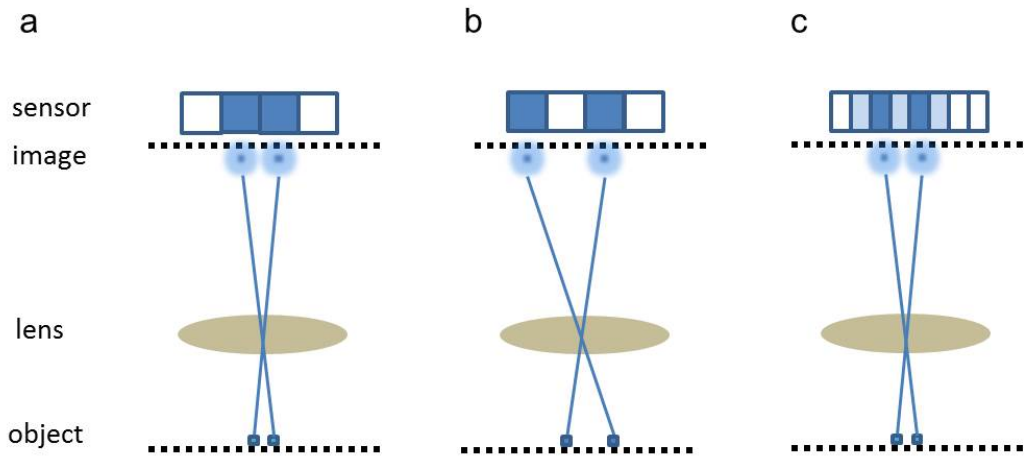

Figure 1.6. The image sensor's impact on resolution. (a) When the sensor pixel size is larger than half of the resolution, even if the two bars can be optically resolved by the lens, they may still not be resolved by the imaging system. (b) The images of the two bars need to have a separation of at least two pixels in order to be resolved by the image sensor. (c) The imaging system can achieve its optical resolution by using an image sensor with small enough pixels.

1.2.2 The relationship between field-of-view (FOV) and resolution

Field-of-view (FOV) can be defined as the lateral dimension of the sample that can be imaged by the microscope. For the conventional microscope system, the resolution and FOV are closely related with each other. The degree of freedom of a microscope system, or the number of independent pixels from a recorded image, is defined as the system's space-bandwidth product (SBP) [5,6]. Although there are many choices of commercial objective lenses, the SBP of the microscope has not experienced too much improvement. This implies an intrinsic tradeoff between resolution and FOV, which can also be better understood by considering the image sensor in the microscope: the number of pixels in the image sensor represents the degree of freedom of the system and it is a constant value. High resolution imaging has to use more pixels to sample small features, so there will not be enough pixels to sample the FOV. On the other hand, low magnification imaging uses the image sensor to collect a large FOV, so the pixels will not be dense enough to sample high resolution features.

1.3 Modern techniques for wide FOV microscopy

In order to break the limit of SBP, or to expand the FOV while maintaining the resolution, many new techniques have been developed in recent years. Some of them re-engineer the illumination method, so that extra information can be obtained using an image sensor with limited number of pixels. Representative examples are the Fourier ptychographic microscopy (FPM), the digital in-line holography, and scanning of focal spot array. There are also other techniques using a more straight-forward approach that scans the FOV on the sample by generating movement between the sample and the image sensor. We will discuss the principles of these new techniques in this section.

1.3.1 Fourier ptychographic microscopy (FPM)

The FPM works with a large FOV but low resolution objective and improves its resolution by implementing a novel illumination method [6–8]. It uses an LED array as the light source, and each LED provides an oblique illumination of the sample, inducing a frequency shift of the image in Fourier space. By a raster scan of the LEDs, a series of low-resolution raw images are obtained, each with a different amount of frequency shift. These raw images can then be stitched together using an iterative computation method to expand the cut-off frequency, and thus a high-resolution, wide-FOV image can be obtained. The FPM is a potentially cost-effective solution since it does not need expensive high-N.A. objective lenses. Although the current FPM system is modified from a standard microscope and it is still bulky, it has potential to be built into a more compact size by custom assembling its LED array, objective, tube lens, and image sensor.

1.3.2 Lensfree holographic on-chip microscopy

Dennis Gabor introduced holography as a lensless microscopic imaging method in 1948 [9]. In recent years, digital holographic microscopy has become an emerging field, where image sensors have been used for holographic measurement and computational methods have been applied for holographic reconstruction [10]. As a related technique, the lensfree holographic on-chip microscopy has been developed as a wide-FOV high-resolution imaging solution [11,12]. In its setup, the sample is placed directly on an image sensor with a small distance to the sensor's pixel surface. An LED with a pinhole is used to project the coherent reference light wave onto the sample, and the interference of the reference wave with the sample-scattered wave is recorded by the image sensor. By using an iterative computational method, the image of the sample can be reconstructed. The resolution is 1-2 μm, and can be further improved to sub-micron by using multiple LED illumination and a superresolution algorithm [13]. This method has a large FOV similar to the image sensor's surface, and is able to recover both the amplitude and the phase information of the sample. However, its reconstruction algorithm has an assumption of sample sparcity, so it is not suitable for imaging samples with high confluency, such as cultured cells. Recently, this method gained the ability of imaging dense samples by placing the sample at multiple distances to the image sensor surface to obtain more information for the reconstruction [14].

1.3.3 Scanning of focal spot array

Using scanning focal spots for illumination is another method to break the SBP limit. In this case, the resolution is not directly determined by the collection optics or the image sensor's pixel size, but by the size of the focal spots. Therefore, we are able to design the collection optics and image sensors to collect wide FOV and design the focal spots to provide high resolution at the same time. In order to improve the throughput and expand the FOV, it is preferable to use a large array of focal spots to scan the sample simultaneously. Researchers have been thinking of different methods for focal spot generation and scanning, and here we will introduce two approaches in this category.

Arpali *et al*. used a spatial light modulator (SLM) to generate an array of Gaussian-shaped spots on the sample surface [15]. The sample is loaded onto the CCD surface through a channel made of adhesive tapes, and the spot array laterally scans the sample by controlling the SLM to get a sequence of images. These images are then merged to generate the final image. Based on the PSF measurement, this demonstrated resolution was not high (~200 μm), due to the width of the Gaussian spots.

Orth and Crozier demonstrated high throughput fluorescence scanning microscopy with an SBP of gigapixel [16─18]. A microlens array (MLA) is illuminated by a green laser beam to generate a focal spot array, and the sample is mounted onto a piezoelectric stage and placed at this focal plane. By the mechanical movement of the stage, the focal spot array performs a raster scan on the sample. Raw images are captured at each scan step by an image sensor, and are then reconstructed into a high-resolution wide-FOV image. This method can achieve a resolution as high as 0.7 μm and an FOV over 5.5 mm × 5.5 mm [16], and multi-color fluorescence imaging can be realized by using a multi-wavelength excitation laser [18]. However, the need of the piezoelectric stage for the scanning increases the size and cost of the system.

1.3.4 Scanning of FOV

Scanning the FOV on the sample is a very straightforward idea for wide FOV imaging. This method can be easily seen in modern microscopes. Microscopes equipped with motorized stages are available in the market, and are capable of imaging multiple areas and stitching them together to create a larger FOV. However, these systems are bulky and high-cost.

Another idea about scanning the FOV comes from commercial flatbed document scanners. In recent years, contact image sensor (CIS) technology has been widely used within commercialized flatbed scanners, where a SELFOC® lens array (SLA) is implemented to create a 1:1 image of the document onto a linear image sensor. This CIS technology has been further explored as a low cost solution for wide FOV imaging [19,20]. Zheng, *et al*. built a wide FOV brightfield scanning microscopy system based on a closed-circuit television (CCTV) lens for image magnification and a flatbed scanner for image acquisition, achieving a sub-micron resolution with a 10 mm × 7.5 mm FOV [19]. In another work, Göröcs, *et al*. demonstrated wide FOV fluorescence imaging by adding an excitation light source and an emission filter to the flatbed scanner, and a >500 cm^2 FOV was obtained with a ~10 μm resolution [20]. Both of these two approaches achieved gigapixel-level SBP.

1.4 The structure of this thesis

This thesis is focused on the development of novel wide FOV microscopic imaging systems, and the demonstration of their capabilities in the longitudinal study of living organisms on different scales, including viral plaques, cultured cells, and live tissues.

In Chapter 2, we will report the application of a wide FOV bright-field on-chip microscope, the ePetri dish, in viral plaque analysis. In Chapter 3, we will introduce a wide FOV fluorescence on-chip microscope, named the Talbot microscope, and demonstrate its capability in high-throughput fluorescence imaging of living cells. Chapter 4 and Chapter 5 will focus on two new endoscopic technologies for the wide FOV imaging of the whole anal canal tissue. In Chapter 4, we will describe a scanning-based endoscope, named the AnCam. In Chapter 5, we will introduce an endoscope integrated with a panoramic lens and a smartphone, named the PanCam. Chapter 6 will give a summary of this thesis.

REFERENCES

1. S. R. Collins, J. S. Weissman, and N. J. Krogan, "From information to knowledge: new technologies for defining gene function," Nat Methods **6**, 721-723 (2009).
2. B. Neumann, M. Held, U. Liebel, H. Erfle, P. Rogers, R. Pepperkok, and J. Ellenberg, "High-throughput RNAi screening by time-lapse imaging of live human cells," Nat Methods **3**, 385-390 (2006).
3. R. Hooke, "Micrographia: or, Some physiological descriptions of minute bodies made by magnifying glasses". London: J. Martyn and J. Allestry, 1665. (first edition).
4. http://www.microscopyu.com/articles/superresolution/diffractionbarrier.html
5. A. W. Lohmann, D. Mendlovic, Z. Zalevsky, C. Ferreira, "space-bandwidth product of optical signals and systems," J. Opt. Soc. Am. A **13**, 470-473 (1996).
6. G. Zheng, R. Horstmeyer, and C. Yang, "Wide-field, high-resolution Fourier ptychographic microscopy," Nat Photonics **7**, 739-745 (2013).
7. X. Ou, R. Horstmeyer, C. Yang, and G. Zheng, "Quantitative phase imaging via Fourier ptychographic microscopy," Opt Letters **38**, 4845-4848 (2013).
8. X. Ou, G. Zheng, and C. Yang, "Embedded pupil function recovery for Fourier ptychographic microscopy," Opt Express **22**, 4960-4972 (2014).
9. D. Gabor, "A new microscopic principle," Nature **161**, 777-778 (1948).
10. P. Marquet, B. Rappaz, P. J. Magistretti, E. Cuche, Y. Emery, T. Colomb, and C. Depeursinge, "Digital holographic microscopy: a noninvasive contrast imaging technique allowing quantitative visualization of living cells with subwavelength axial accuracy," Opt Letters **30**, 468-470 (2005).
11. O. Mudanyali, D. Tseng, C. Oh, S. O. Isikman, I. Sencan, W. Bishara, C. Oztoprak, S. Seo, B. Khademhosseini, and A. Ozcan, "Compact, light-weight and cost-effective microscope based on lensless incoherent holography for telemedicine applications," Lab Chip **10**, 1417-1428 (2010).
12. A. Greenbaum, W. Luo, T. W. Su, Z. Gorocs, L. Xue, S. O. Isikman, A. F. Coskun, O. Mudanyali, and A. Ozcan, "Imaging without lenses: achievements and remaining challenges of wide-field on-chip microscopy," Nat Methods **9**, 889-895 (2012).
13. S. O. Isikman, W. Bishara, S. Mavandadi, F. W. Yu, S. Feng, R. Lau, and A. Ozcan, "Lens-free optical tomographic microscope with a large imaging volume on a chip," Proc Natl Acad Sci U S A **108**, 7296-7301 (2011).
14. A. Greenbaum, U. Sikora, and A. Ozcan, "Field-portable wide-field microscopy of dense samples using multi-height pixel super-resolution based lensfree imaging," Lab Chip **12**, 1242-1245 (2012).
15. S. A. Arpali, C. Arpali, A. F. Coskun, H. H. Chiang, and A. Ozcan, "High-throughput screening of large volumes of whole blood using structured illumination and fluorescent on-chip imaging," Lab Chip **12**, 4968-4971 (2012).
16. A. Orth and K. Crozier, "Microscopy with microlens arrays: high throughput, high resolution and light-field imaging," Opt Express **20**, 13522-13531 (2012).
17. A. Orth and K. Crozier, "Gigapixel fluorescence microscopy with a water immersion microlens array," Opt Express **21**, 2361-2368 (2013).
18. A. Orth and K. B. Crozier, "High throughput multichannel fluorescence microscopy with microlens arrays," Opt Express **22**, 18101-18112 (2014).

19. G. A. Zheng, X. Z. Ou, and C. H. Yang, "0.5 gigapixel microscopy using a flatbed scanner," Biomed Opt Express **5**, 1-8 (2014).
20. Z. Gorocs, Y. Y. Ling, M. D. Yu, D. Karahalios, K. Mogharabi, K. Lu, Q. S. Wei, and A. Ozcan, "Giga-pixel fluorescent imaging over an ultra-large field-of-view using a flatbed scanner," Lab Chip **13**, 4460-4466 (2013).

C h a p t e r 2

VIRAL PLAQUE ANALYSIS ON AN EPETRI PLATFORM

In this chapter, we will describe the application of a wide field-of-view (FOV), time-lapse, on-chip imaging platform, the ePetri, for plaque analysis of murine norovirus 1 (MNV-1). The observation of viral plaques is the standard method for determining viral titer and understanding the behaviors of viruses. The ePetri offers the ability to dynamically track plaques at the individual cell death event level over a wide FOV of 6 mm × 4 mm. As demonstrated, we captured high-resolution time-lapse images of MNV-1-infected cells at 30 min intervals. We implemented a customized image-processing program containing a density-based clustering algorithm to analyze the spatial-temporal distribution of cell death events to identify plaques at their earliest stages. By using the results in a viral titer count format, we showed that our approach gives results that are comparable to conventional plaque assays. We further showed that the extra information collected by the ePetri can be used to monitor the dynamics of plaque formation and growth. Finally, we performed a demonstration experiment to show the relevance of such an experimental format for antiviral drug study. We believe the ePetri is a simple and compact solution for the automation of viral plaque assays, plaque behavior analysis, and antiviral drug discovery and study. This chapter is adapted from C. Han and C. H. Yang, "Viral plaque analysis on a wide field-of-view, time-lapse, on-chip imaging platform," *Analyst* **139**, 3727-3734 (2014).

2.1 Background

The analysis of viral plaques is the standard method for determining virus concentration and understanding their proliferation and spread behaviors [1,2]. A plaque is a region of host cells undergoing cytopathic effects (CPEs). Plaque growth is initiated when a virus particle attaches to a host cell, penetrates the cell membrane, replicates, induces CPE, and releases a new generation of viruses, which then diffuse to neighboring host cells to repeat the process [3]. Because each plaque originates from a single virus particle, the number of plaques can be counted to determine the virus titer in a sample. This method is termed a plaque assay, and is widely used for viral quantification [1,4]. The area and shape of the plaques, together with the speed of plaque growth, can be used to study viral behavior [5]. Viral plaques can also be used for the screening of antiviral drugs [6].

Since the establishment of the first plaque assay [4], little has changed over the decades. Viral plaques are still grown in conventional Petri dishes or multi-well plates. Plaques are counted by the naked eye; therefore, several days are required for sufficient growth of the plaques [1]. This manual counting process is labor-intensive and time-consuming. The plates also have to be taken out of the incubator for observation, which is inconvenient and may disturb virus distribution. In addition, the cells need to be stained with dyes such as neutral red or crystal violet to enhance contrast for the plaque readout, preventing continuous monitoring of plaque growth dynamics.

In recent years, studies have used standard microscopes for time-lapse imaging of viral plaques in order to investigate the behaviors of different viruses. Wodarz *et al*. monitored the spatial dynamics of recombinant adenovirus type-5 proliferation using a fluorescence microscope [7]. However, they had a large imaging interval (24 h), and had to capture several images for each plaque and stitch them together due to the small FOV of the microscope. Doceul *et al*. studied the rapid plaque growth of the Vaccinia virus using a microscope integrated with a stage incubator that collected time-lapse images at much shorter intervals (1 h) [2]; however, they were also restricted by a 10× objective FOV, so a limited number of plaques were recorded for statistical build-up. In summary, standard microscopes are high-cost with limited FOVs; therefore, they are not ideal platforms for viral plaque analysis.

Commercialized systems such as the aCOLyte 3 and ProtoCOL 3 from Synbiosis were developed for wide FOV colony counting. They used light-emitting diodes (LEDs) for illumination, a charge-coupled device (CCD) camera with a lens for imaging, and integrated software capable of automated plaque counting from Petri dishes or multi-well plates. However, they have limited resolution (e.g., ProtoCOL 3 can accurately measure features down to 0.1 mm) and cannot support the observation of single cell death events. They do not provide a cell culture environment and are not designed for continuous plaque growth monitoring. Similar to the conventional manual plaque counting method, the sample usually has to be stained with dyes to provide better contrast for the automatic plaque counting software. A technology that combines the resolution of a microscope with the large FOV of a commercialized colony counting system, and supports time-lapse imaging, is strongly needed.

Our group recently developed a wide-FOV, on-chip imaging method termed ePetri and have demonstrated its compact, wide-FOV imaging capability in longitudinal monitoring of cell culture and stem cell differentiation [8]. This technique is based on the use of a super-resolution algorithm [9] in combination with proximal cell imaging by growing the cells directly on the sensor chip to perform high-resolution and wide-FOV imaging. If the resolution of the image is restricted by the detector pixel size, we can enhance it by capturing a sequence of sub-pixel-shifted, low-resolution (LR) images and combining them to reconstruct a high-resolution (HR) image. The ePetri device has demonstrated the ability to image at 700-nm resolution with a FOV of 6 mm × 4 mm without using any optical lenses.

The ePetri device has several intrinsic advantages for plaque analysis. First, its wide FOV supports the observation of multiple plaques at the same time. Second, its sub-micron resolution enables much earlier identification of a plaque site than conventional means, as well as observation of individual cell death events within each plaque. Third, the imaging process can be operated automatically and continuously inside the incubator. This not only saves labor and avoids disturbing the sample, but also allows the monitoring of the plaque growth process. Fourth, the ePetri device is engineered using mass-producible electronic components without optical lenses, making it a low-cost imaging solution. Finally, the ePetri device is compact in size ($10 \times 10 \times 10$ cm^3 for our current prototype) and allows multiple devices to be run in parallel inside the same incubator, increasing imaging throughput.

In this chapter, we developed the ePetri device for use with viral plaque assays, as well as for monitoring the dynamics of viral plaque formation and development. We chose murine norovirus 1 (MNV-1) as our model virus and RAW 264.7 as the host cell line. During the on-chip plaque growth we obtained a 24-mm^2 FOV and time-lapse HR images at 30 min intervals. We then built an image-processing program for plaque recognition and tracking. We observed that cells undergoing CPE would detach from the substrate, becoming spherical, which focuses more light onto the sensor surface, causing them to appear much brighter than healthy cells. Taking advantage of this effect, we were able to segment dying cells from healthy cells using a simple thresholding method. We also noticed that a plaque is a cluster of high-density cell death events, so we incorporated a well-established, density-

based clustering algorithm [10] to detect the plaques. To our knowledge, this is the first time a clustering algorithm has been used for viral plaque detection. The last step of the program distinguishes between connected plaques by tracking their growth history. Using this program we conducted a plaque assay, tracked plaque growth, and studied antiviral drugs.

In this chapter, we will first describe the ePetri device setup in detail and explain the imaging approach. Next we will explain our customized plaque recognition program. We will then demonstrate the plaque counting performance of our system in comparison with conventional plaque assays. Then we will show the dynamic monitoring of plaque formation and growth. Finally, we will describe the demonstration use of our system to investigate the responses of viral plaque growth to two different antiviral drugs: 2'-C-methylcytidine (2CMC) and neuraminidase.

2.2 Imaging principles and system setup

When the sample is on the surface of a complementary metal-oxide semiconductor (CMOS) image sensor, it can directly record a shadow image of the sample. However, due to the pixel size of the image sensor (2.2 μm in our experiment), the resolution is limited to approximately twice the pixel size (according to the Nyquist criterion). To improve the pixel-limited resolution, we applied a super-resolution algorithm described in our previous work [8,9]. Briefly, we placed the sample 1 μm above the image sensor surface (determined by the sensor's passivation layer), then tilted the illumination angle to induce a sub-pixel shift of the sample shadow on the image sensor, and captured a series of LR images at each angle. Next, we calculated the amount of the shift by estimating the height of the sample above the pixels. Finally, we interpolated the LR images into a larger matrix according to their corresponding shift amounts, to reconstruct a HR image.

The ePetri device is depicted in Figure 2.1a. It consists of (1) an illuminator, (2) a CMOS sensor chip with a reservoir (also shown in Figure 2.2b), (3) a camera board, and (4) a thermoelectric cooler (TEC) with a fan. RAW 264.7 cells were cultured on the sensor (Figure 2.2a), and infected with MNV-1 (Figure 2.2b); subsequently, the sensor chip was mounted onto the camera board. As viral plaques appeared and expanded (Figure 2.2c), time-lapse LR images were recorded: at each frame, the 8×8 LED array illuminated the

sample from different angles by switching on one LED at a time and performing a raster scan (Figure 2.3), creating a sequence of LR images. The TEC and fan were used to protect the cells and viruses from the heat generated by the sensor circuit. During the imaging process, the system was placed inside a standard 37°C CO_2 incubator. A laptop running a customized MATLAB program was used to control the LED array, the TEC, and the fan, as well as to collect the LR images at 30-min intervals. After imaging, another customized MATLAB super-resolution program processed the LR images and produced a HR image for each imaging interval.

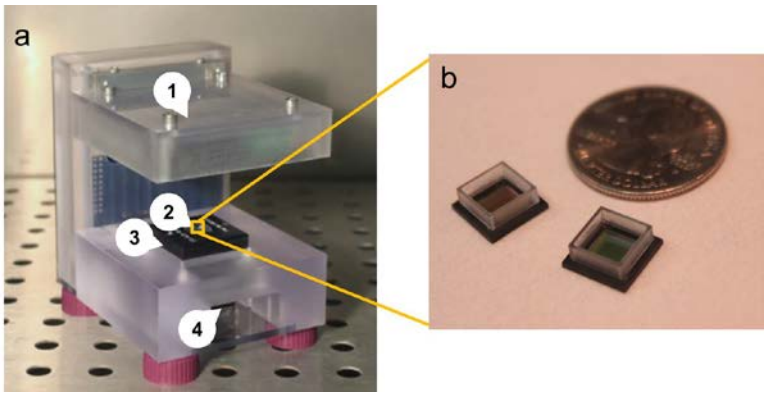

Figure 2.1. The ePetri device setup. (a) The ePetri device prototype. (b) Image sensor with reservoir.

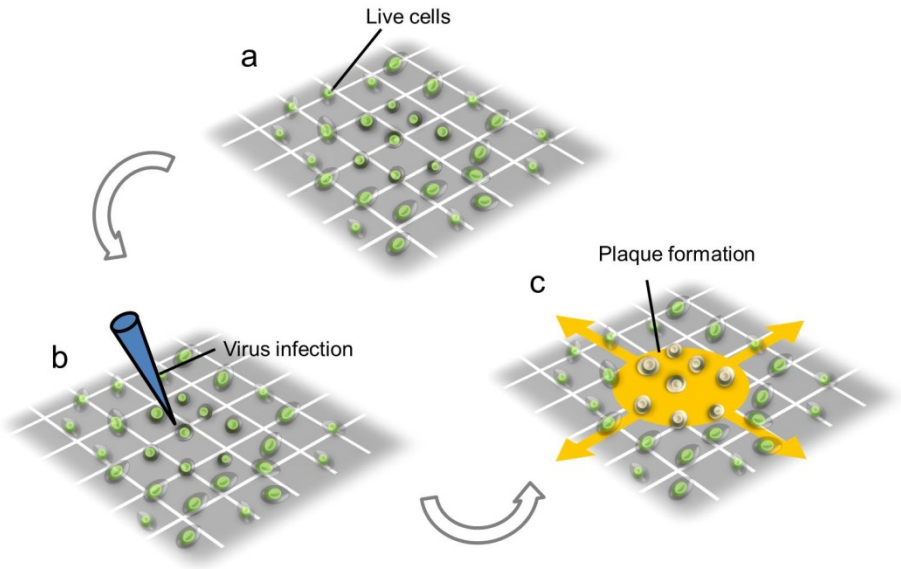

Figure 2.2. Viral infection and plaque growth on the image sensor. (a) Cells are cultured on the sensor. (b) Cells are infected by the virus. (c) A viral plaque appears and starts to expand.

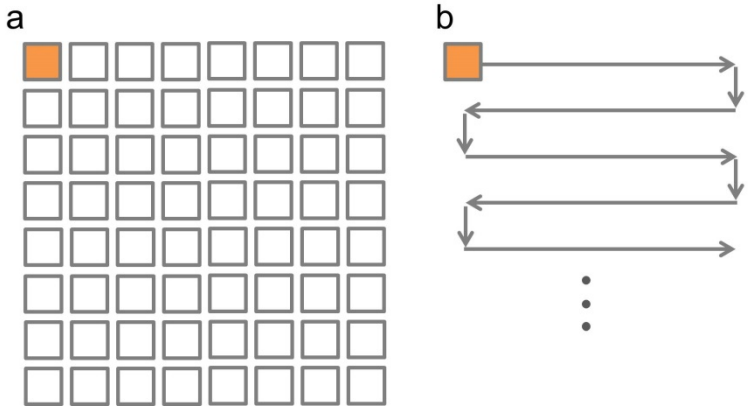

Figure 2.3. The scanning mechanism of the 8×8 LED array. (a) One LED is switched on at a time. (b) The LED array performs a raster scan with its LEDs.

As demonstrated, Figure 2.4 shows a representative image of a HR image compared with a LR image at the same region during the viral plaque development at 22.5 h after infection. Cells under CPEs are clearly discernible from the HR image (inside the white circle), while they are hard to distinguish in the LR image. We can also notice that the dead cells are brighter than the background, so they can be directly recognized by simple thresholding.

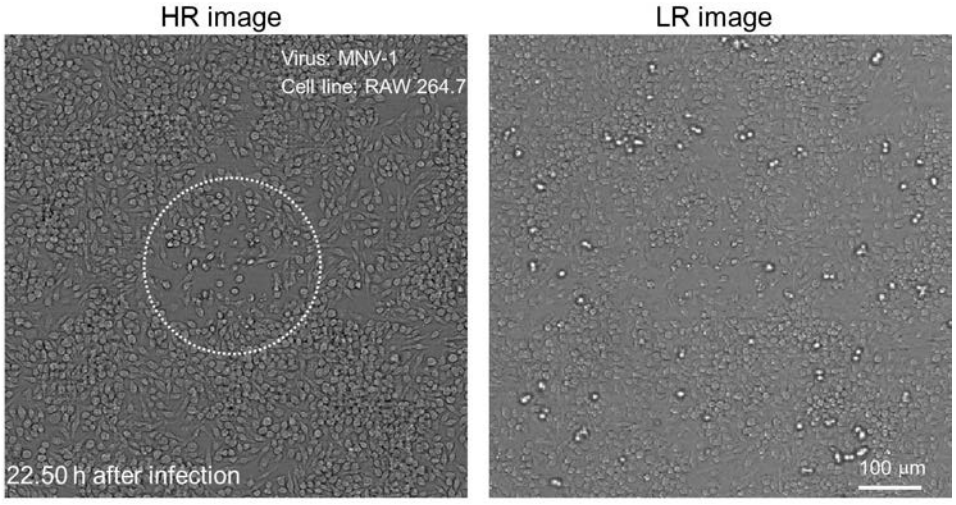

Figure 2.4. Comparison of a HR image with a LR image during the viral plaque growth process. Left: HR image. Right: LR image.

To show the big picture, a full-FOV HR image is presented in Figure 2.5a with a typical growing plaque (zoomed inset shown in Figure 2.5b). The dynamic growing process of a viral plaque is also shown in Figure 2.5c, with their boundaries labeled in white circles.

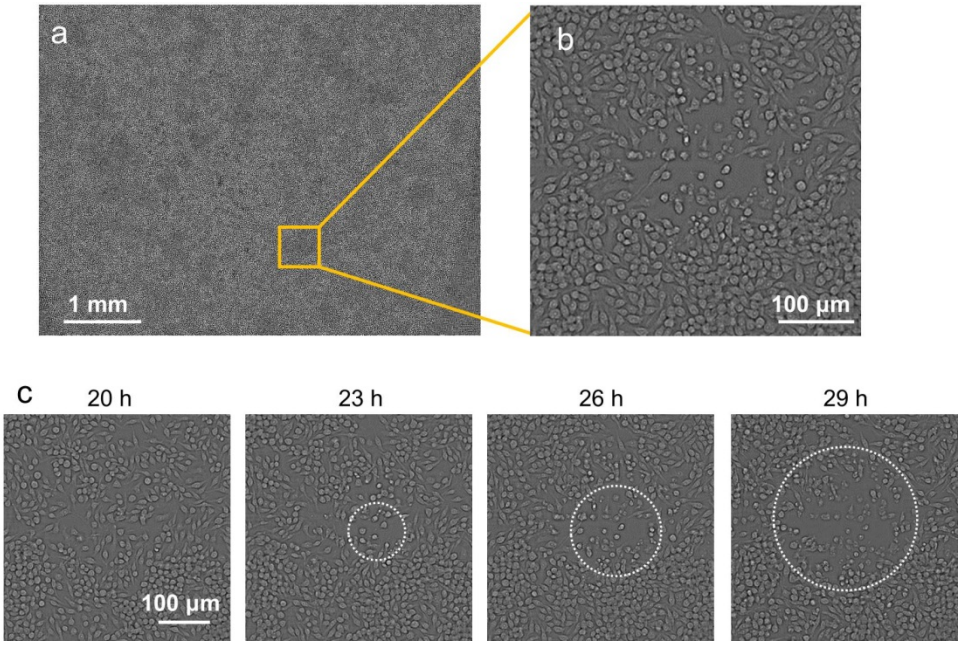

Figure 2.5. The wide FOV imaging of viral plaques and the time-lapse imaging of plaque growth. (a) A representative, full field-of-view, high-resolution image with (b) a typical growing plaque zoomed in. (c) The dynamic process of a growing plaque.

2.3 Plaque recognition by image processing

We designed an image-processing program to automatically detect plaques from time-lapse HR image sequences. This algorithm is able to detect newly generated plaques, track the growth of each individual plaque, and distinguish different plaques after they contact each other. Each frame was processed based on the time-lapse HR image sequence using the results of the previous frames. The program consists of six major steps, as illustrated by the flowchart in Figure 2.6. The representative dynamic results for each step are also shown in Figure 2.7.

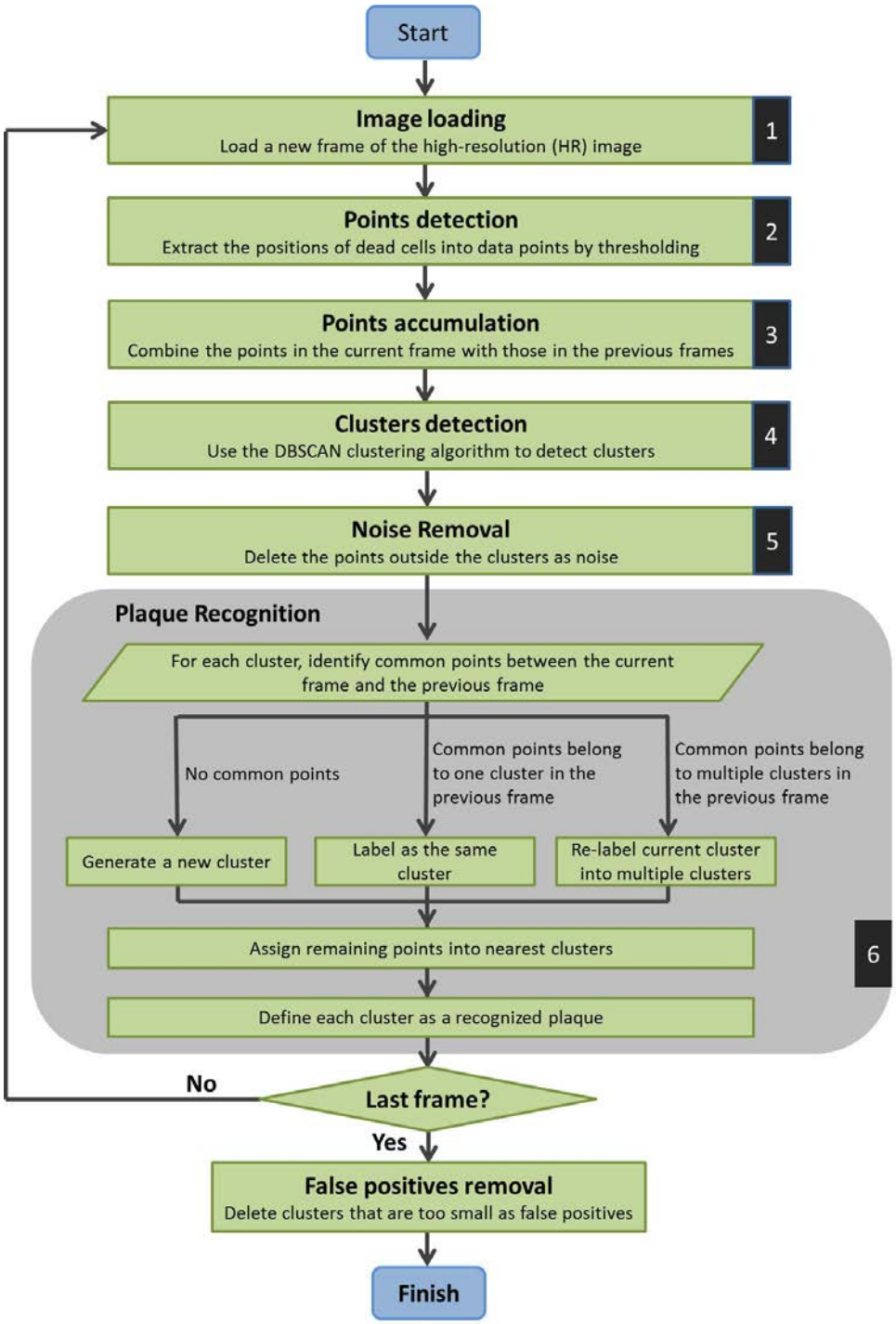

Figure 2.6. The plaque recognition algorithm structure.

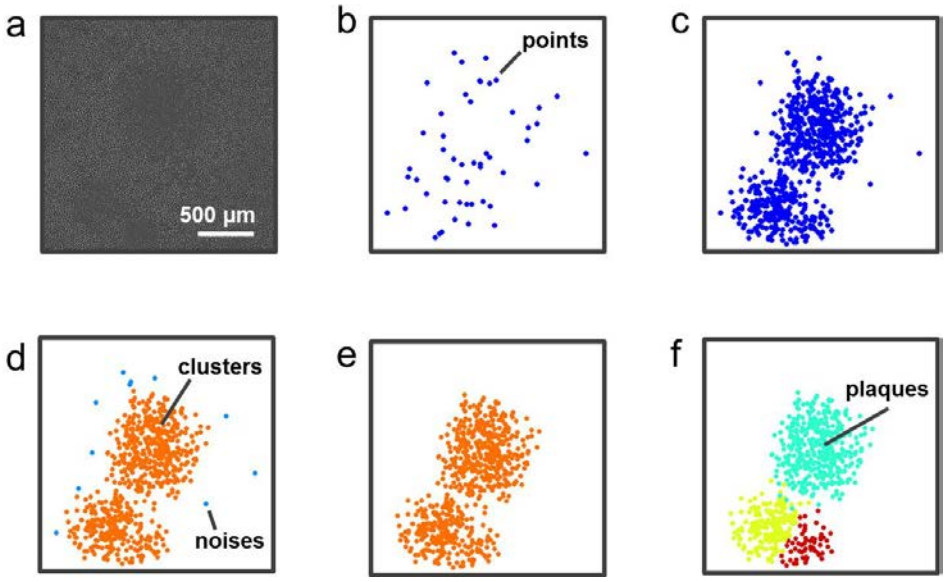

Figure 2.7. Representative results for each step in the plaque recognition algorithm. (a) Image loading. (b) Points detection. (c) Points accumulation. (d) Clusters detection. (e) Noise removal. (f) Plaque recognition.

The six steps are described in detail as follows:

1. Image loading

A new frame from the HR image sequence is loaded into the program.

2. Points detection

A brightness threshold is set for the image (typically 2.2 times the mean value of the whole image), converting the HR image into a binary (0-1) image with only the profiles of the dying cells. The center-of-mass is extracted from each profile to generate the dying cell positions into our data points.

3. Points accumulation

The detected points in Step 2 are combined with the plaque detection results from the previous frame.

4. Clusters detection

Considering that a plaque is a cluster of dead cells with high density, we apply a density-based clustering algorithm to the data points generated in Step 3. The density-based spatial clustering of applications with noise (DBSCAN) algorithm is used [10]. This detects clusters by gauging the spatial density of the points, with its basic principle illustrated in Figure 2.8. Briefly, each point is evaluated by two thresholds. The first threshold is Eps, which is the required neighborhood distance between this point and its surrounding points. The second threshold is MinPnts, which represents the required number of other points within the Eps neighborhood. For a given point, if there are > MinPnts points within the Eps neighborhood, then this point is labeled as the core point. If there are <MinPnts points within the Eps neighborhood but there is at least one core point in the Eps neighborhood, then this point is labeled as a border point. All the density-connected core points and border points are considered elements of the same cluster. In this way, the algorithm evaluates all the points and labels them according to the clusters they belong to. The points that do not belong to any clusters are considered noise points. The typical values used in our experiments were Eps=150 μm and MinPnts=5.

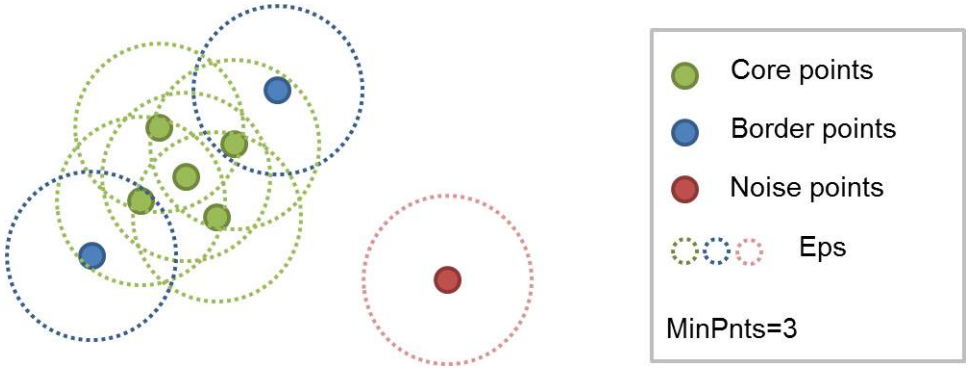

Figure 2.8. The principle of DBSCAN algorithm. For the eight points in this figure, five of them are labeled as core points (green) and two are labeled as border points (blue), which together form a cluster of seven points. The remaining one point is labeled as a noise point (red). The dashed circles show the Eps, and the MinPnts is set at 3 for illustration.

5. Noise removal

After Step 4, the points that do not belong to any clusters are considered noise and are removed from the current frame.

6. Plaque Recognition

The plaque recognition step consists of several sub-steps. First, each current cluster is compared with the previously recognized plaques. If it does not have any common points with previous plaques, it is considered a new cluster (this means a new plaque has been generated). If it has common points with only one previous plaque, it is labeled the same cluster as the previous one (this means a single plaque is growing). If it has common points with multiple previous plaques, these corresponding common points are labeled separately according to each previous plaque (this means multiple plaques are starting to contact each other). Second, each un-labeled point in the current cluster is assigned to its nearest labeled cluster. After labeling all the points in the current clusters, each cluster is defined as a recognized plaque.

After the last frame is finished, the recognized plaques with insufficient points (typically <20 points) are considered false positives and are removed.

We built a customized MATLAB program for this algorithm. For verification, we manually examined 72 plaques in five ePetri plaque assay experiments and compared them with the results of our program. The plaque recognition accuracy of our program was 93±7% (there were 3±5% plaques unrecognized, and 2±3% falsely unseparated).

2.4 ePetri plaque assay

To compare the performance of our ePetri plaque assay method and the conventional multi-well plate plaque assay, we grew plaques on both six-well plates and CMOS image sensors (relative scale shown in Figure 2.9a). The RAW 264.7 cells were cultured to ~70% confluence for both groups. The same MNV-1 sample was used with different dilutions for each method ($1{:}10^7$ dilution for the conventional plaque assay, and $1{:}10^5$ dilution for the ePetri plaque assay). For the conventional plaque assay, cells were stained with neutral red 48 h after infection and the plaques were counted by the naked eye (Figure 2.9b). For the ePetri group, the HR images were taken at 30 min intervals until 32 h after infection (Figure 2.9c), and our plaque recognition program was used to automatically count the number of plaques in the last frame (Figure 2.9d). The plaque titer given by the conventional plaque assay and ePetri plaque assay were $2.1\pm0.6 \times 10^8$ PFU/ml (SEM, N=4) and $1.9\pm0.3 \times 10^8$ PFU/ml (SEM, N=4), respectively, without significant differences,

according to the Student's *t-test* (P=0.13). It is worth noting that we demonstrated a shorter readout time (32 h) compared with the conventional plaque assay (48 h as established in the standard protocol [1]), due to the ability of the ePetri plaque assay to recognize plaques from their early stages. We will show this in the next section.

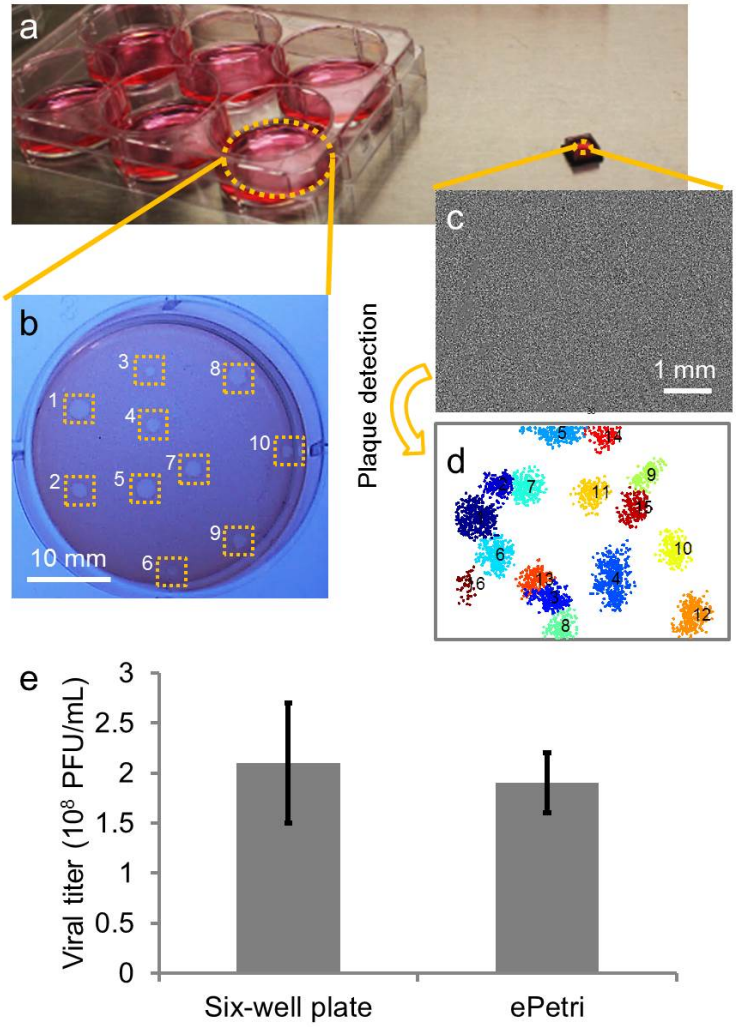

Figure 2.9. Plaque assay experiment. (a) A six-well plate for the conventional plaque assay, compared with a CMOS image sensor for the ePetri plaque assay. (b) A representative image of the conventional plaque assay. Manually counted plaques were labeled with white squares. (c) A representative image of the ePetri plaque assay (d) with the plaques automatically detected. (e) The calculated viral titer of the conventional plaque assay compared with that of the ePetri plaque assay.

2.5 Longitudinal observation of plaque growth

In addition to plaque recognition, the ePetri plaque assay method automatically captures a longitudinal sequence of cell death events on the entire sensor chip. This means that we can also use the data to investigate plaque growth dynamics from their earliest stages. As a demonstration example, we tracked the growth pattern of a single plaque (Figure 2.10). Figure 2.10a shows the time-lapse images of a growing plaque with individual cell death events labeled. Figure 2.10b shows the same plaque with each cell death event colored according to its occurrence. Based on this data, we also generated statistics of cell death numbers over time (Figure 2.10c).

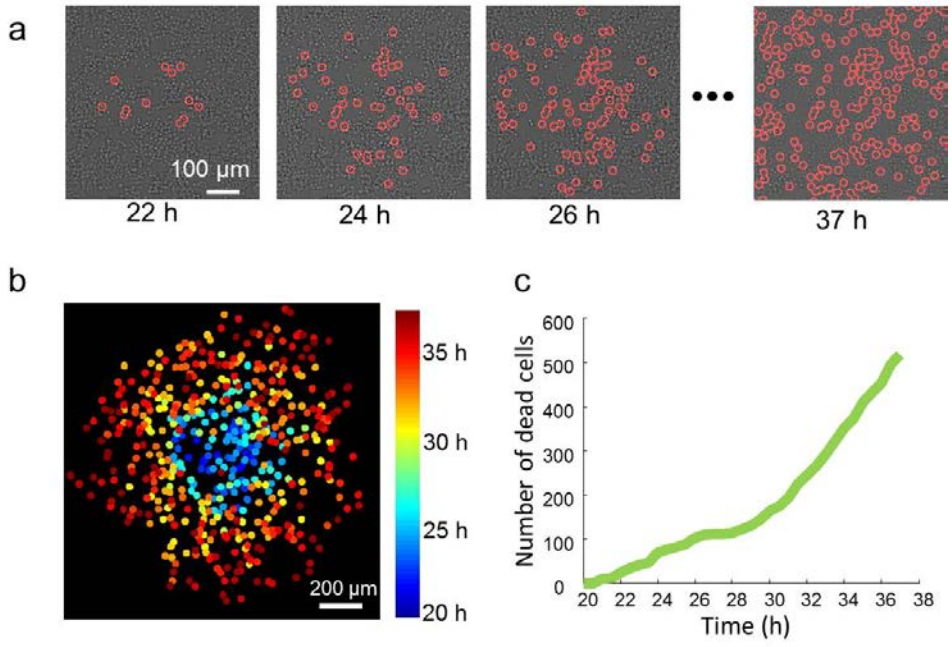

Figure 2.10. Longitudinal observation of the plaque growth. (a) Time-lapse HR images of a growing plaque with individual cell death events labeled. (b) The same plaque with each cell death event colored according to its occurrence. (c) Number of cell deaths over time in the plaque.

Our plaque detection algorithm also gives us the time at which a new plaque appears. As a demonstration example, we defined the time of generation of a new plaque as the time at which it was picked up by our clustering algorithm, and conducted two experiments to monitor plaque formation events over time (Figure 2.11a). From the histogram of the two

experiments (Figure 2.11b-c), we observed that the peak of plaque formation happened 24–26 h after MNV-1 infection, and the time between the formation of early plaques and late plaques was approximately 6 h.

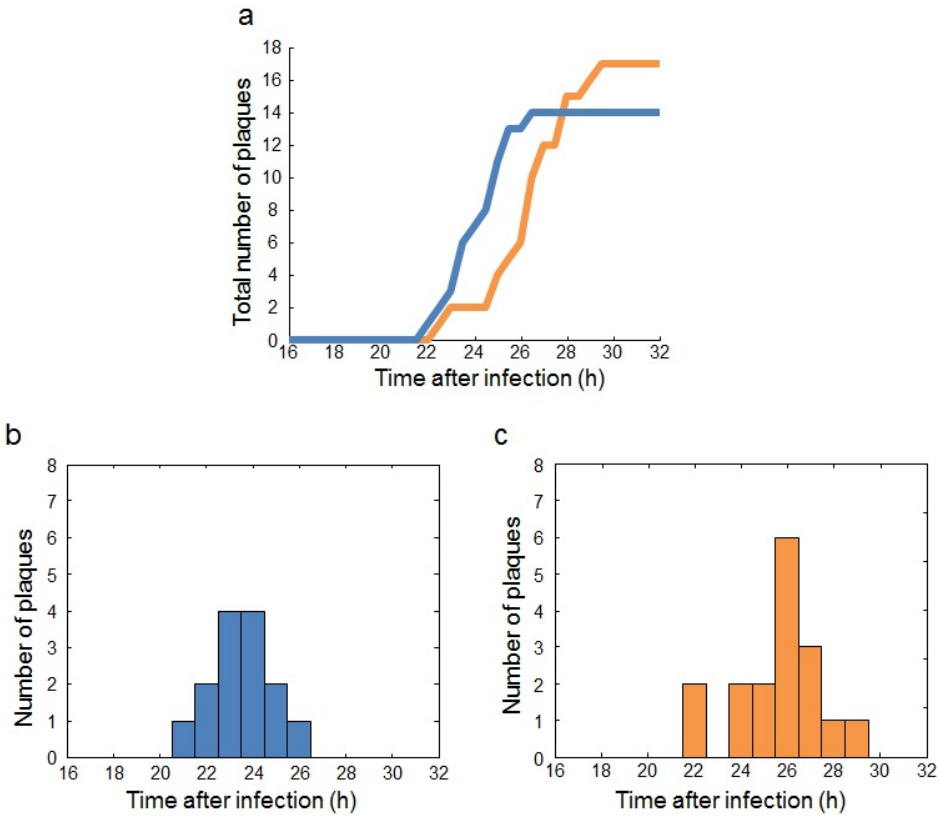

Figure 2.11. Dynamics of plaque formation. (a) Plaque formation events over time for two independent experiments. (b-c) The histograms showing plaque formation distribution in (b) the first experiment (blue curve in a) and (c) the second experiment (orange curve in a).

2.6 Demonstration study of viral inhibitor treatment

We demonstrated the ePetri device in a viral inhibitor study. We selected two previously discovered MNV-1 inhibitors. The first inhibitor is 2'-C-methylcytidine (2CMC), which blocks the RNA replication pathway [11]. The second one is neuraminidase, which cleaves terminal sialic acids on the surface of host cells, preventing viral attachment to cells [12,13]. We included one control group without inhibitors (Figure 2.12a). We used two

different concentrations for the 2CMC treatment group (4 μM and 10 μM) and the neuraminidase treatment group (1 mU/ml and 2.5 mU/ml). Each treatment was repeated once, and a 1:(2×10^4) dilution of a MNV-1 sample was used for all the groups. We monitored each group for 32 h after virus infection. To increase the throughput, we ran 2–3 ePetri devices in parallel each time. Representative final plaque recognition results for each group are shown in Figure 2.12a─12e. We then investigated the effects of the two inhibitors on the total number of plaques (Figure 2.12f). In the case of 2CMC, the plaque number decreased by 40% at a concentration of 4 μM, and no plaques appeared when the concentration increased to 10 μM. In the case of neuraminidase, the plaque number decreased by 60% at a concentration of 1 mU/ml, but no further decrease was observed at 2.5 mU/ml. Further increase in neuraminidase concentration had negative effects on cell growth. Finally, we also examined plaque size by defining the radius of a circle with the same area as the plaque, calculated the mean and standard deviation of the radius data for each group, and statistically analyzed the data between the groups using one-way ANOVA followed by Tukey's HSD test (Figure 2.12g). For the 2CMC group, the plaque radius at 4 μM (106±14 μm, N=19) was significantly smaller than that of the control group (130±15 μm, N=31) with $P<0.001$, and reduced to 0 μm (no plaques) at 10 μM. For the neuraminidase group, the plaque radius was also significantly smaller than the control group at 1 mU/ml (102±15 μm, N=9) with $P<0.001$, but did not significantly drop when the dose was increased to 2.5 mU/ml (95±12 μm, N=12), with $P=0.677$. The results suggest that 2CMC is capable of completely inhibiting viral proliferation, whereas neuraminidase is not. In this study, we added neuraminidase after viral infection as a proof of concept. However, as previously studied [12], the treatment of neuraminidase before viral infection can have a better inhibitory effect. We will use our ePetri device to investigate this timing of neuraminidase treatment in our future work.

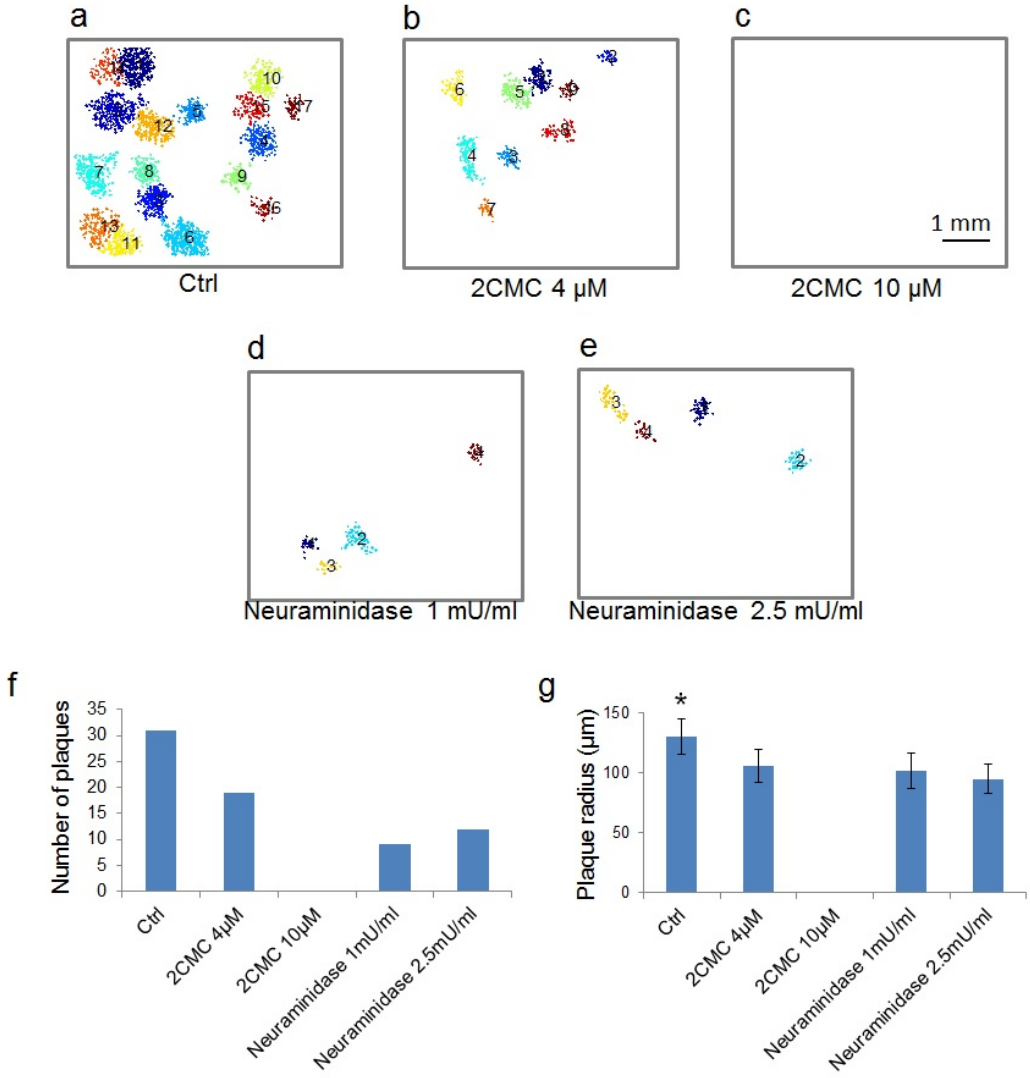

Figure 2.12. Study of viral inhibitor treatments. (a─e) Representative images showing the plaque recognition results of (a) the control group, the 2CMC group at concentrations of (b) 4 μM, and (c) 10 μM, and the neuraminidase group at concentrations of (d) 1 mU/ml and (e) 2.5 mU/ml, 32 h after MNV-1 infection. (f) Number of plaques for all the five groups. (g) Means and standard deviations of the plaque radiuses for all the five groups (* $P<0.05$).

2.7 Discussion

The ePetri device has several intrinsic advantages for plaque analysis. First, its wide FOV supports the observation of multiple plaques at the same time. Second, its sub-micron resolution enables much earlier identification of a plaque site than conventional means, as well as observation of individual cell death events within each plaque. Third, the imaging process can be operated automatically and continuously inside the incubator. This not only saves labor and avoids disturbing the sample, but also allows the monitoring of the plaque growth process. Fourth, the ePetri device is engineered using mass-producible electronic components without optical lenses, making it a low-cost imaging solution. Finally, the ePetri device is compact in size ($10 \times 10 \times 10$ cm^3 for our current prototype) and allows multiple devices to be run in parallel inside the same incubator, increasing imaging throughput.

In this study, we selected MNV-1 as our virus model due to its high significance. Norovirus (NoV) is the top pathogen causing foodborne illness in the United States and is responsible for more than 23 million infections per year [14]. So far, little is known about the infection mechanisms of human NoVs, and there is no specific treatment for human NoV infection because it cannot grow in tissue culture systems. Discovered in 2003, MNV-1 is the only member of NoVs that can successfully grow in tissue culture [15]. We believe that the ePetri approach can provide more insight into the mechanisms of NoV infection, as well as those of other viruses that are conventionally studied by plaque assays.

We used thresholding to detect virus-induced cell death events in our algorithm. Occasionally, some random cell deaths or temporary cell detachment events (such as cell division) were also picked up by the thresholding. These data points are considered noise for plaque detection. These noise points are randomly generated and sparsely distributed around the whole imaging area. Conversely, the cell deaths inside virus plaques have much higher density; therefore, we were able to extract them from the noise by applying the density-based clustering algorithm.

We measured the virus concentration of the same sample using both the ePetri plaque assay and the conventional plaque assay in a 6-well plate. We were able to read out the results using the ePetri plaque assay at 32 h after infection, whereas we read out the conventional plaque assay by the naked eye 48 h after infection, following standard protocols [1]. The

ePetri plaque assay provides high resolution in detecting single cell death events; therefore, we were able to recognize plaques when they were still small in size, reducing the wait time for the plaque assay.

We determined the formation time of a plaque by looking at when a cluster was recognized by our algorithm. The experiment shows that the peak of plaque formation occurred at 24–26 h after infection, and the time between the formation of early plaques and late plaques was ~6 h. This verifies that the 32-h monitoring time was enough to cover the formation events of all the plaques. The ~6 h difference between the early and late plaques may suggest the heterogeneous nature of our virus sample. This contains rich information on viral behavior and is worth further investigation. One future experiment might involve retrieving the virus from a single plaque and testing whether plaque formation time can be synchronized. Another would be to work on different virus strains and study the variation in their plaque formation time.

Generally, there are five steps in a virus life cycle: attachment to the host cell membrane, entry into the cell, genome replication, protein synthesis, and virus release [16]. This process is illustrated in Figure 2.13. In this study, we demonstrated the application of our system on the evaluation of antiviral drugs by choosing two already established virus inhibitors: neuraminidase and 2CMC, which inhibit the membrane attachment and RNA replication, respectively, of MNV-1. In recent years, many other antiviral drugs targeting different steps of the virus life cycle have also been studied. Here we summarize some typical drugs in Figure 2.14. Among these drugs, dynasore and nocodazole were reported to inhibit virus entry [17]. WP1130, ribavirin, and simvastatin were reported to suppress virus replication [18-20]. Cycloheximide and type I/II interferons inhibit virus protein synthesis [21,22]. Oseltamivir and zanamivir inhibit virus release from host cells [16]. The ePetri can potentially be a potential powerful tool for studying all these drugs and their effects on plaque formation and plaque growth dynamics.

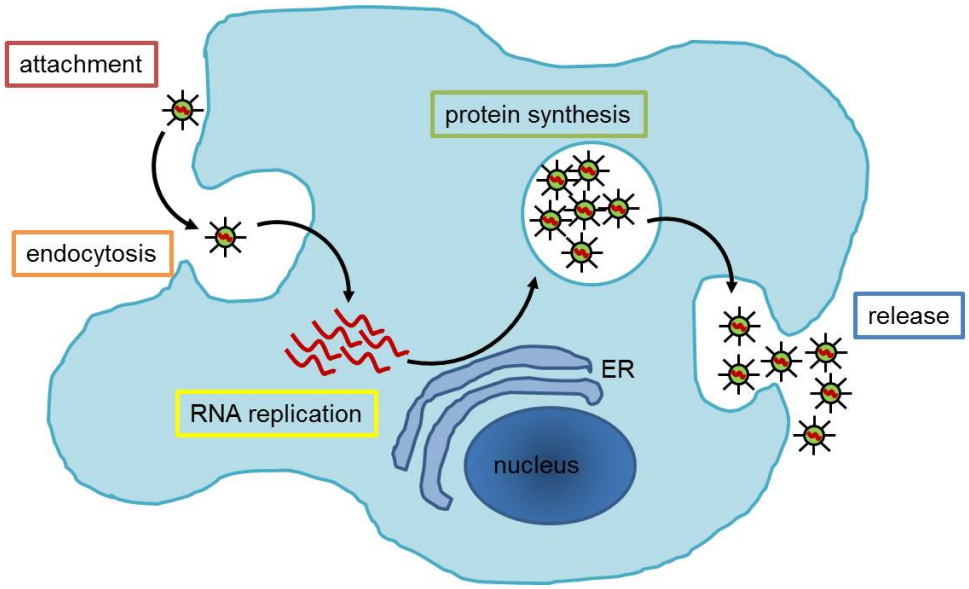

Figure 2.13. The life cycle of MNV-1 virus. It includes attachment, endocytosis, RNA replication, protein synthesis, and release.

Attachment	Endocytosis	RNA replication	Protein synthesis	Release
Neuraminidase	Dynasore Nocodazole	2CMC Ribavirin WP1130 Simvastatin	Type I/II interferon Cycloheximide	Oseltamivir Zanamivir

Figure 2.14. Typical antiviral drugs targeting different steps of the MNV-1 virus life cycle. They have inhibitive effect on virus attachment [12,13], endocytosis [17], RNA replication [18-20], protein synthesis [21,22], and release [16], respectively.

The conventional plaque assay has several inherent limitations. First, it is time-consuming because plaque growth is a slow process and can take several days. Second, many viruses do not kill host cells and consequently do not form plaques; therefore, it is not possible to study them using the plaque assay. To overcome these limitations, a variation of the plaque assay called the fluorescent focus assay (FFA) was developed [23]. A FFA is similar to a plaque assay except that it uses fluorescently-labeled antibodies targeting viral antigens to measure host cell infection; therefore, it can give information on viral spread even before a plaque is formed. In addition, such an assay can directly visualize viruses, so that plaque

observation is not needed. We have recently developed a wide FOV on-chip fluorescence microscope that supports high-resolution fluorescence imaging, and have already demonstrated its use in time-lapse imaging of GFP-labeled HeLa cells as well as in the study of anti-cancer drugs [24,25]. We believe this fluorescence ePetri device will be well-suited for the study of FFA in our future work.

2.8 Conclusion

To conclude, in this chapter we applied the ePetri device to viral plaque analysis. Time-lapse, high-resolution images were obtained by the ePetri device at 30-min intervals. A density-based clustering algorithm, DBSCAN, was introduced into a customized program for plaque recognition. This plaque recognition program was then used for the plaque assay and longitudinal monitoring of plaque formation and growth. We further explored potential applications of our device by studying the two viral inhibitors, 2CMC and neuraminidase, and observed a difference in their inhibition on plaque growth. We expect that the ePetri device can be used for many applications, such as the study of virus behavior and the discovery of new antiviral drugs.

2.9 Experimental section

2.9.1 Conventional plaque assay

Conventional plaque assays were conducted by the following standard protocols [1]. Briefly, RAW 264.7 cells (~70% confluency) cultured in DMEM were inoculated with various dilutions of the MNV-1 sample in six-well plates with each dilution added in two wells (0.5 ml per well). After 1.5 h incubation for MNV-1 attachment, the media was removed and a 37°C low melting point (LMP) agarose solution (1.5% in DMEM, 3 ml per well) was added. The plates were placed into a 37°C CO_2 incubator for 48 h, then stained with 0.02% neutral red solution for 1 h. A stained six-well plate was mounted on top of a light box for illumination, and a digital single-lens reflex (DSLR) camera was used to capture the image. Visible plaques were counted by the naked eye, as demonstrated in Figure 2.15. The number of plaques in both wells at each dilution was added and multiplied by the dilution factor. This gives the number of plaque forming units (PFUs) in a 1-ml volume. For example, consider two wells at $1:10^7$ dilution: if one well has 10 plaques and the other well has 5 plaques, the viral titer is $10\times10^7+5\times10^7=15\times10^7$ PFU/ml.

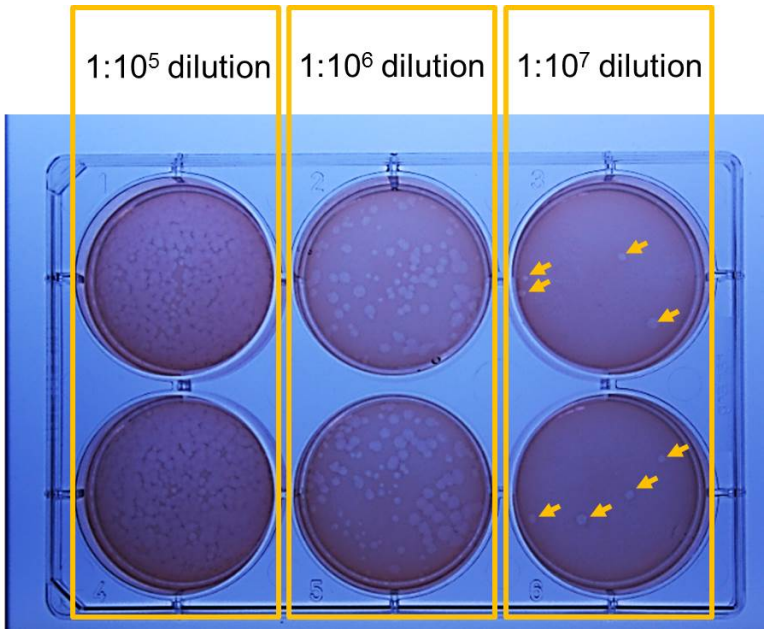

Figure 2.15. A stained six-well plate for conventional plaque assay. The yellow arrows show the viral plaques counted by visual inspection at $1:10^7$ dilution of the original viral solution.

2.9.2 The ePetri device for plaque analysis

The ePetri device was designed based on our previous work8 and provided by ePetri Inc. We used MT9P031 (2.2 μm pixel, Aptina) for the image sensors and removed their microlens layers by treating them in oxygen plasma for 10 min at 80 W. The homemade square plastic reservoir was glued to the image sensor using polydimethylsiloxane (PDMS).

The protocol for viral plaque growth on the image sensor is similar to that used in the conventional plaque assay. Briefly, image sensors were pre-treated with trypsin for surface cleaning and better cell adhesion. The DMEM solution containing ~10^5 RAW 264.7 cells was filled into each sensor's reservoir. After cells grew to ~70% confluence, the media was changed to the diluted MNV-1 solution (typically 20 μl) and a coverslip was placed on top of the medium. After 1.5 h incubation for MNV-1 attachment, the coverslip and virus solution were removed, and the 37°C low-melting point agarose solution (1.5% in DMEM, 150 μl) was added. A thin layer of DMEM was overlaid on top of the agarose to prevent evaporation. Sensor chips were mounted onto the ePetri devices with a customized PDMS

cap placed above the image sensor to prevent further evaporation. The systems were placed into the 37 °C CO_2 incubator for continuous imaging at 30 min intervals.

The viral titer for the ePetri plaque assay was calculated in a similar manner to the conventional plaque assay. However, because the reservoir's area (7.25×7.25 mm^2) was 2.15 times the sensor's imaging area (5.70×4.28 mm^2), the measured virus concentration was multiplied by this factor during calculations. For example, consider that we used 20 μl MNV-1 solution at $1:10^5$ dilution: if we count 15 plaques, then the viral titer is $15\div0.02\times10^5\times2.15=16\times10^7$ PFU/ml.

For the experiments in the viral inhibitor study, the protocol remained the same, except that the drug (2CMC/neuraminidase) was added to the low-melting point agarose solution before it was overlaid onto the cells.

REFERENCES

1. M. B. Gonzalez-Hernandez, J. Bragazzi Cunha, and C. E. Wobus, "Plaque assay for murine norovirus," J Vis Exp, e4297 (2012).
2. V. Doceul, M. Hollinshead, L. van der Linden, and G. L. Smith, "Repulsion of superinfecting virions: a mechanism for rapid virus spread," Science **327**, 873-876 (2010).
3. J. Yin and J. S. McCaskill, "Replication of viruses in a growing plaque: a reaction-diffusion model," Biophys J **61**, 1540-1549 (1992).
4. R. Dulbecco, "Production of Plaques in Monolayer Tissue Cultures by Single Particles of an Animal Virus," Proc Natl Acad Sci U S A **38**, 747-752 (1952).
5. Y. Lee and J. Yin, "Detection of evolving viruses," Nat Biotechnol **14**, 491-493 (1996).
6. M. Matrosovich, T. Matrosovich, W. Garten, and H. D. Klenk, "New low-viscosity overlay medium for viral plaque assays," Virol J **3**, 63 (2006).
7. D. Wodarz, A. Hofacre, J. W. Lau, Z. Sun, H. Fan, and N. L. Komarova, "Complex spatial dynamics of oncolytic viruses in vitro: mathematical and experimental approaches," PLoS Comput Biol **8**, e1002547 (2012).
8. G. Zheng, S. A. Lee, Y. Antebi, M. B. Elowitz, and C. Yang, "The ePetri dish, an on-chip cell imaging platform based on subpixel perspective sweeping microscopy (SPSM)," Proc Natl Acad Sci U S A **108**, 16889-16894 (2011).
9. S. C. Park, M. K. Park, and M. G. Kang, "Super-resolution image reconstruction: A technical overview," IEEE Signal Processing Magazine **20**, 21-36 (2003).
10. M. Ester, H. Kriegel, J. Sander, and X. Xu, "A Density-Based Algorithm for Discovering Clusters in Large Spatial Databases with Noise," Proceedings of 2nd International Conference on Knowledge Discovery and Data Mining *(KDD-96)*, (AAAI Press, 1996), 226-231.
11. J. Rocha-Pereira, D. Jochmans, K. Dallmeier, P. Leyssen, R. Cunha, I. Costa, M. S. Nascimento, and J. Neyts, "Inhibition of norovirus replication by the nucleoside analogue 2'-C-methylcytidine," Biochem Biophys Res Commun **427**, 796-800 (2012).
12. J. W. Perry and C. E. Wobus, "Endocytosis of murine norovirus 1 into murine macrophages is dependent on dynamin II and cholesterol," J Virol **84**, 6163-6176 (2010).
13. S. Taube, J. W. Perry, K. Yetming, S. P. Patel, H. Auble, L. Shu, H. F. Nawar, C. H. Lee, T. D. Connell, J. A. Shayman, and C. E. Wobus, "Ganglioside-linked terminal sialic acid moieties on murine macrophages function as attachment receptors for murine noroviruses," J Virol **83**, 4092-4101 (2009).
14. J. L. Hyde, S. V. Sosnovtsev, K. Y. Green, C. Wobus, H. W. Virgin, and J. M. Mackenzie, "Mouse norovirus replication is associated with virus-induced vesicle clusters originating from membranes derived from the secretory pathway," J Virol **83**, 9709-9719 (2009).
15. S. M. Karst, C. E. Wobus, M. Lay, J. Davidson, and H. W. t. Virgin, "STAT1-dependent innate immunity to a Norwalk-like virus," Science **299**, 1575-1578 (2003).
16. J. Magden, L. Kaariainen, and T. Ahola, "Inhibitors of virus replication: recent developments and prospects," Appl Microbiol Biotechnol **66**, 612-621 (2005).

17. A. Gerondopoulos, T. Jackson, P. Monaghan, N. Doyle, and L. O. Roberts, "Murine norovirus-1 cell entry is mediated through a non-clathrin-, non-caveolae-, dynamin- and cholesterol-dependent pathway," J Gen Virol **91**, 1428-1438 (2010).
18. J. W. Perry, M. Ahmed, K. O. Chang, N. J. Donato, H. D. Showalter, and C. E. Wobus, "Antiviral activity of a small molecule deubiquitinase inhibitor occurs via induction of the unfolded protein response," PLoS Pathog **8**, e1002783 (2012).
19. K. O. Chang and D. W. George, "Interferons and ribavirin effectively inhibit Norwalk virus replication in replicon-bearing cells," J Virol **81**, 12111-12118 (2007).
20. K. O. Chang, "Role of cholesterol pathways in norovirus replication," J Virol **83**, 8587-8595 (2009).
21. K. Bok, V. G. Prikhodko, K. Y. Green, and S. V. Sosnovtsev, "Apoptosis in murine norovirus-infected RAW264.7 cells is associated with downregulation of survivin," J Virol **83**, 3647-3656 (2009).
22. H. Changotra, Y. Jia, T. N. Moore, G. Liu, S. M. Kahan, S. V. Sosnovtsev, and S. M. Karst, "Type I and type II interferons inhibit the translation of murine norovirus proteins," J Virol **83**, 5683-5692 (2009).
23. A. F. Payne, I. Binduga-Gajewska, E. B. Kauffman, and L. D. Kramer, "Quantitation of flaviviruses by fluorescent focus assay," J Virol Methods **134**, 183-189 (2006).
24. S. Pang, C. Han, M. Kato, P. W. Sternberg, and C. Yang, "Wide and scalable field-of-view Talbot-grid-based fluorescence microscopy," Opt Lett **37**, 5018-5020 (2012).
25. C. Han, S. Pang, D. V. Bower, P. Yiu, and C. Yang, "Wide field-of-view on-chip Talbot fluorescence microscopy for longitudinal cell culture monitoring from within the incubator," Anal Chem **85**, 2356-2360 (2013).

C h a p t e r 3

THE TALBOT MICROSCOPE AND TALBOT FLUORESCENCE EPETRI SYSTEM

In the previous chapter, we applied the ePetri dish to the analysis of viral colony growth. In this chapter we develop another wide field-of-view (FOV) imaging technique, named the Talbot microscope, for the fluorescence imaging of live cells. The Talbot microscope takes advantage of the Talbot effect and can generate a focal spot array to scan the fluorescence samples directly on-chip. We demonstrate its capability by imaging various fluorescence-stained and live green fluorescent protein (GFP)-coded cell samples. We further upgraded the Talbot microscope for the long-term time-lapse fluorescence imaging of cell cultures, and named it the Talbot Fluorescence ePetri. As a demonstration, we obtained time-lapse images of HeLa cells expressing H2B-eGFP, and we also employed the system to analyze the cells' dynamic response to anticancer drug camptothecin (CPT). The Talbot microscope has a resolution limit of 1.2 μm and an FOV of ~13 mm^2. The method described in this chapter can provide a compact and simple solution for automated high-throughput fluorescence imaging of cell cultures in incubators.

This chapter is adapted from two publications. The first publication is *S. Pang, *C. Han, M. Kato, P. W. Sternberg, and C. H. Yang, "Wide and scalable field-of-view Talbot-grid-based fluorescence microscopy," *Opt Lett* **37**, 5018-5020 (2012). The second publication is *C. Han, *S. Pang, D. V. Bower, P. Yiu, and C. H. Yang, "Wide field-of-view on-chip Talbot fluorescence microscopy for longitudinal cell culture monitoring from within the incubator," *Anal Chem* **85**, 2356-2360 (2013). * denotes equal contribution.

3.1 Background

Time-lapse or longitudinal fluorescence microscopy can reveal the dynamics of biological processes, and is of crucial importance to many studies in cell biology, such as clarifying gene function by RNA interference [1], visualizing cell apoptosis [2], and aiding drug discovery [3]. Time-lapse imaging generally requires a wide field-of-view (FOV) in order to view and track a large number of migrating and dividing cells over extended periods of time. However, traditional fluorescence microscopes use an objective lens and have a limited FOV. Microscopes equipped with motorized stages are available in the market that

are capable of imaging multiple areas and stitching them together to create a larger FOV [2,4]. Unfortunately, these systems are bulky and costly.

Over the past few years, significant efforts have been made to build a wide FOV on-chip fluorescence imaging system with reduced size and cost. Most of these efforts [5,6] concentrate on using an image sensor chip (either CCD or CMOS-based) to directly collect fluorescence signals from the samples that are placed in proximity to the chip (the descriptor of 'on-chip' for characterizing this line of work refers to the proximity of sample to the sensor chip). This design choice eliminates the microscopy objective and achieves an effective FOV that is approximately equal to the sensor chip's active sensor area. These methods span a range of resolutions. The simplest method [5] inserts an absorption fluorescence filter between the sample and a CCD sensor chip. In the demonstration experiment, the distance between sample and sensor was ~100 μm. The sample was excited by uniform illumination and the emitted fluorescence spread on the CCD. Based on point-spread function (PSF), such a system has an image resolution of ~100 μm. (The authors claimed a compressive sensing resolution of ~10 μm. However, this parameter is only applicable to sparsely distributed sample and the same method can be applied to conventional microscopy to claim improved resolution for sparse samples.) In another approach, Arpali *et al*. used a spatial light modulator (SLM) to generate an array of Gaussian-shaped spots on the sample surface [6]. The sample was loaded onto the CCD surface through a channel made of adhesive tapes, and the spot array laterally scanned the sample to get a sequence of images. These images were then merged to generate the final image. Based on PSF, this demonstrated resolution should be ~200 μm – the width of the Gaussian spots. Neither of these approaches can provide enough resolution for sub-cellular features (typically on a scale of several microns), and thus are not adequate for longitudinal cell fluorescence imaging.

In this chapter, we develop a new on-chip fluorescence imaging technique, the Talbot Microscope. This method uses a uniformly laser-illuminated lenslet array to generate an array of tightly focused laser spots. By the Talbot self-imaging effect [7], this light grid propagates forward and regenerates itself into focused light spots at certain distances. This focal spot array can then be used to perform high-resolution scanning of the sample (see system setup for detailed description). This approach has several advantages for wide FOV

time-lapse fluorescence imaging. First, its ~1 μm resolution is sufficient for imaging sub-cellular features such as cell membranes and nuclei. Second, the use of the Talbot effect affords a large working distance (~3.7 mm in our case) between the optical illumination elements and the sample; this spacing is vital for allowing the incorporation of microfluidic components for perfusion culture purposes. This advantage also distinguishes the Talbot microscope from a related non-Talbot approach that has a much shorter demonstrated working distance (~40 μm) [8]. Third, the FOV is directly scalable by using a larger lenslet array to create more focal spots and by employing a larger sensor chip for signal collection. This advantage stands in contrast with conventional microscopy, where scaling up the FOV requires broader mechanical scanning range and therefore longer image acquisition time. Fourth, our key components are a MEMS mirror, a lenslet array, and a webcam CMOS sensor for detection. All of them are low cost, mass-producible, and compact. In this study, we further demonstrate that a Talbot microscope system in combination with microfluidic cell culture and temperature control components can be applied to perform wide FOV time-lapse fluorescence imaging of cell cultures from within an incubator. To our knowledge, this is the first demonstration of automated wide FOV and high-resolution fluorescence imaging for longitudinal cell culture studies that does not rely on conventional microscopy methods.

The new imaging modalities that can simply and effectively monitor cell cultures from within an incubator are a recent scientific development. To date, our group has developed a brightfield wide FOV on-chip imaging method that provides a compact wide FOV imaging capability for cell culture applications (termed ePetri) [9]. This current work extends this line of development by introducing fluorescence imaging capability. We believe that this approach can significantly streamline the work flow of Petri dish based assays by reducing labor. With its wide FOV and ~1 μm resolution, our demonstrated method can potentially offer a labor-saving, low-cost, and mass-producible solution for drug screening, dynamic cell imaging, and medical diagnostics.

In the next section, we will introduce the imaging principle of the Talbot microscope. We will then describe the system setup in detail and explain the imaging approach. Next we will demonstrate the wide FOV imaging capability by imaging quantum dots-stained or GFP-labeled biological samples, and an application for high throughput phenotyping of *C.*

elegans. Finally, we will introduce the upgraded Talbot microscope (hereby termed Talbot Fluorescence ePetri), and demonstrate the time-lapse fluorescence imaging of HeLa cells expressing histone 2B-tagged eGFP (H2B-eGFP), where cells in the sequence of images are automatically counted and tracked. In this application, we will also apply our system to investigate the response of cells to anti-cancer drug camptothecin.

3.2 The imaging principle of the Talbot microscope

3.2.1 The Talbot effect

The Talbot effect is named after Henry Fox Talbot, who first observed this diffraction effect [10]. The Talbot effect is a self-imaging effect of a periodic pattern due to Fresnel diffraction: when a coherent plane wave illuminates a periodic structure, a repeated image of the structure will appear at certain distances as the wave propagates. The distances where we can observe the Talbot self-images are $z = n \cdot z_T$, where n is an integer, and z_T is named the Talbot distance, which can be further defined as:

$$z_T = \frac{2d^2}{\lambda} \tag{3–1}$$

where d is the structure's period and λ is the wavelength of the coherent plane wave. Figure 3.1 shows a simulation of the Talbot effect generated by a microlens array (MLA) using the angular spectrum method [11]. When a coherent plane wave is incident on the MLA, an array of focal spots is generated (at distance 0). As the wave propagates down, we can observe that this focal spot array repeats itself at the Talbot distance (at distance z_T). It is noticeable that at distance $z_T/2$ there also appears a focal spot array but with a shift of d/2. Also, the spot arrays with decrease pitch can be seen at the fractions of the Talbot distance.

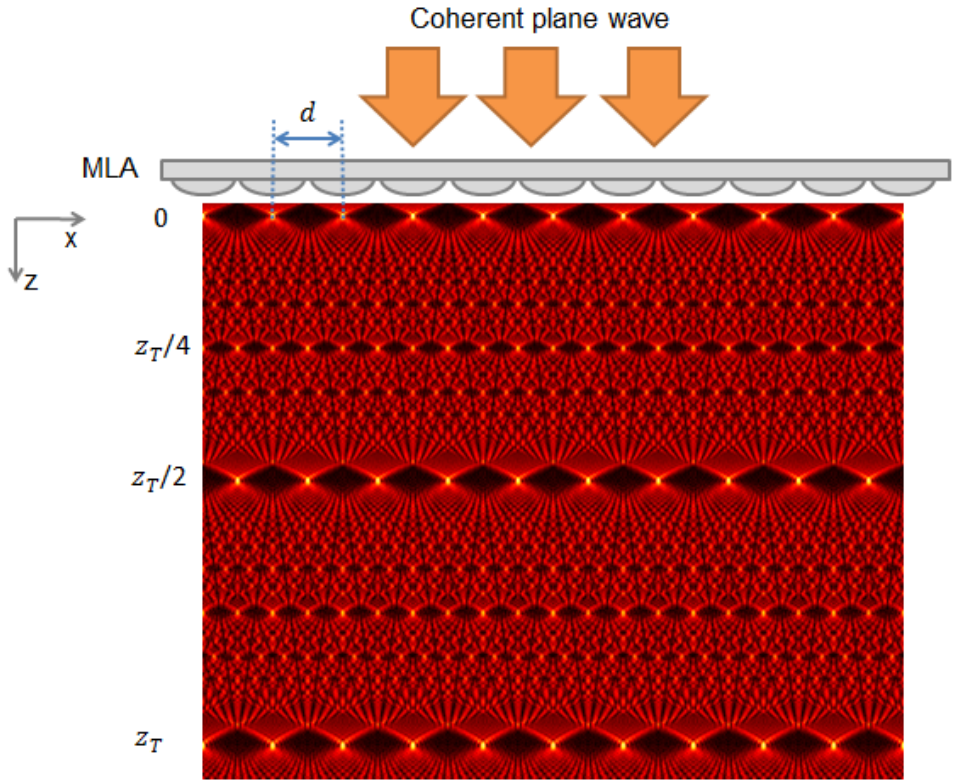

Figure 3.1. The simulation of the Talbot effect of a focal spot array by using angular spectrum. It is noticeable that the focal spot array repeats itself at the Talbot distance z_T.

It has also been studied that we can shift the focal spots at the Talbot distance laterally by tilting the illumination angle of the incident plane wave [12,13]. The relationship between the amount of lateral shift and the tilting angle can be expressed as:

$$\Delta x = z_T \cdot tan\theta \qquad (3\text{—}2)$$

where Δx is the lateral shift amount of the focal spots at the Talbot distance and θ is the tilt angle of the incident wave. Based on this effect, we will be able to control the focal spots at the Talbot distance to perform a raster scan by tuning the illumination angle of the light source, which is the basic principle of the Talbot microscope.

It is worth noting that the tilt angle will also induce a shift in z direction. At the Talbot distance, this relationship can be expressed as [13]:

$$\Delta z = z_T \cdot cos^3\theta \qquad (3\text{–}3)$$

where Δz is the shift amount of the focal spots in z direction. The shift in this direction is undesirable for our imaging purpose, since we would like to make the focal spot scan on the same plane. Fortunately, the tilt angle in our experimental condition is very small, so that the amount of Δz can be safely negligible (Δz =0.18 μm for θ ranging from -4 mrad to 4 mrad, and z_T=3.7 mm).

3.2.2 The Talbot microscope

Based on the properties of the Talbot effect, we can build a scanning microscope as illustrated in Figure 3.2. We can coat a filter material on an image sensor chip to block the excitation light, then directly deposit the sample on the top surface of the sensor. A Talbot focal spot array can be aligned at the same plane as the sensor's surface, then perform a raster scan of the sample, with the raw images directly collected by the sensor at each scan step. The fluorescence signal excited by each focal spot can be extracted from the raw images and combined together to reconstruct into a high resolution image. In this way, the resolution of the image depends only on the size of the focal spots.

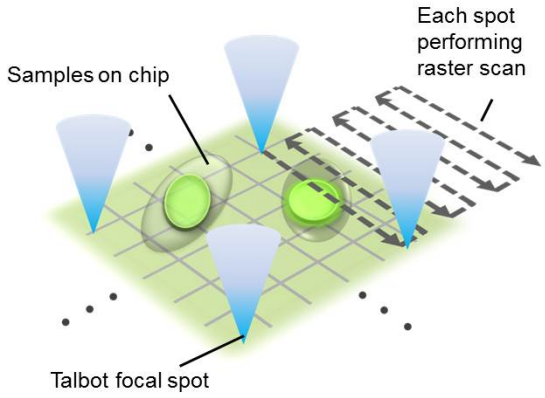

Figure 3.2. The imaging principle of the Talbot microscope. The sample is deposited on the surface of a filter-coated image sensor chip, and the Talbot focal spot array performs a raster scan of the sample, with the image directly collected by the sensor.

3.3 System Setup

Our Talbot Fluorescence ePetri system is depicted in Figure 3.3a. The illuminator is described in detail in Figure 3.3b and 3.3c. Briefly, the illuminator uses a 488 nm 30 mW fiber coupled laser (FiberTec II, Blue Sky Research) as its light input. The input light is collimated by a fiber collimator (CL) and guided to a polarizing beam splitter (PB) and reflected towards the MEMS mirror (M2, Mirrocle). A quarter wave plate (WP) was placed between the polarizing beam splitter and the MEMS mirror to allow the beam reflected by the MEMS mirror to pass through the beam splitter. The reflected beam is then expanded by two convex lenses (L1 and L2) and hits a microlens array (MLA, 18-00407, SUSS). It is worth noting that the MEMS mirror is at the back focal plane of L1, while the microlens array is placed at the front focal plane of L2, so that they together form a 4F system. This ensures that the angular tilt of the beam will not move the beam position on the microlens array.

The reflected light transmitted through the MLA with pitch d = 30 μm, area = 225 mm^2, and focal distance z_f = 90 μm, to create an array of focused laser spots at a distance z_f after the lenslet array. Due to the Talbot effect [7], this array repeated itself at distance z_f+nz_T. For our experiments, we chose to use the n = 1 refocused Talbot spot array for our scanning purpose (samples will be placed in that plane for imaging). This afforded us with a large working distance of ~3.7 mm between the illuminator and the sample. By angularly tilting the input light field using the MEMS mirror over an angular range of 8 mrad (the tilt angle ranges from -4 mrad to 4 mrad), we could laterally shift the scanning array by 30 μm. By this approach, we could raster scan each Talbot focal spot over an area of 30 μm × 30 μm. Since the laser spot pitch was equal to the lenslet array pitch (30 μm), this scanning approach allowed us to fully cover the whole area of interest.

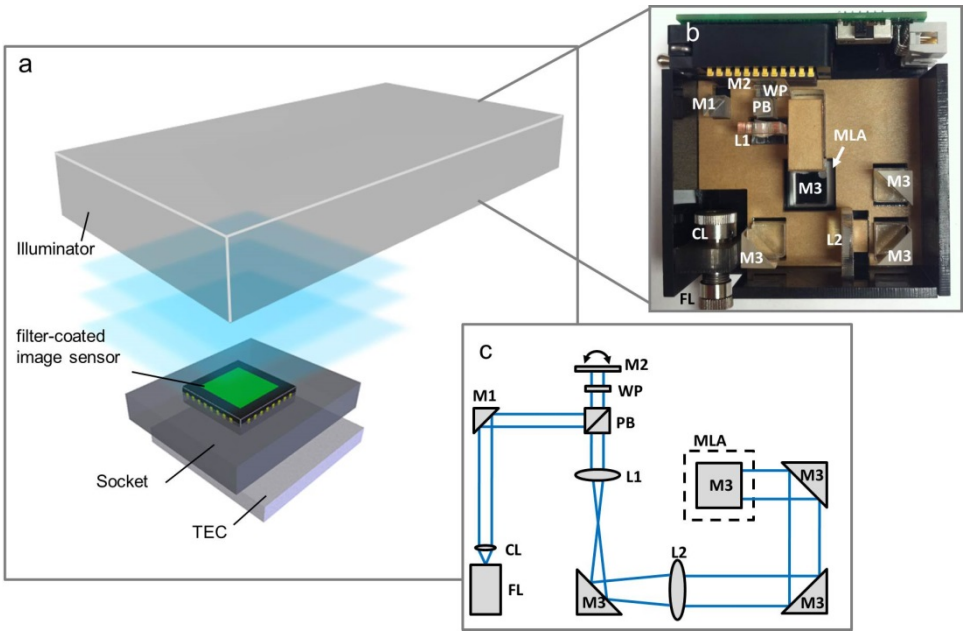

Figure 3.3. The system setup of the Talbot microscope. (a) An illustration of the Talbot microscope system consisting of an illuminator, a filter-coated CMOS sensor, a socket, and a thermoelectric cooler (TEC). (b) A photo of the illuminator showing its inside structure. (c) A schematic of the illuminator. FL: fiber laser; CL: fiber collimator; L1: Plano-convex lens (f=10 mm); L2: plano-convex lens (f=50 mm); M1: right angle prism mirror (5 mm); M2: MEMS mirror; M3: right angle prism mirror (10 mm); MLA: microlens array; PB: polarizing beamsplitter; WP: achromatic 1/4 wave plate.

The heart of the sensing platform consists of a 2.2-μm pixel-size (MT9P031I12STM, Aptina Imaging) or a 5.2-μm pixel-size (MT9M001C12STM, Aptina Imaging) CMOS sensor chip. The glass cover was removed from each sensor to provide access to the sensor surface. Fluorescence emission filter materials (Aptina Green1 or Aptina Red 1, Aptina) were coated onto the sensors following the same methods in our previous work [14]. An additional PDMS layer was spin-coated on top of the filter layer for protection. The 2.2-μm pixel-size image sensors were used in Section 3.6, while the 5.2-μm pixel-size image sensors were used in Section 3.5 and 3.7. The sensor chip is mounted onto a camera board (EPIX) via a customized sensor socket for signal readout. A thermoelectric cooler is attached to the socket to protect the live cells from the heat generated by the sensor circuit. The other side of the TEC is cooled by a CPU fan. This prototype is able to acquire a full

image at a maximum rate of one frame per 115 second with an FOV of 13 mm^2 using the 5.2-μm pixel-size image sensor, while it takes a maximum rate of one frame per ~5 min for the 2.2 -μm pixel-size image sensor.

We have established that the filter-coated sensor chip's sensitivity is ~10^5 fluorophores/μm^2 for Alexa Fluor 488 under 488 nm laser illumination with 10 mW/cm^2 intensity and 15 ms integration time. During imaging, the power delivered by each Talbot focal spot was ~10^{-4} mW.

3.4 Resolution

We further investigated the optical resolution of our system by measuring the point spread function (PSF). A droplet of quantum dots (A10198, Life Technologies) was placed and dried on a red filter-coated image sensor. A small cluster was imaged at a scanning step size of 0.4 μm (Figure 3.4a). The Gaussian fit of the spot has a full width at half maximum (FWHM) of 1.25 μm in the x direction and 1.21 μm in the y direction (Figure 3.4b,c). This experiment was carried out using the 5.2-μm pixel-size sensor, however it should be noted that the resolution depends on the size of the focal spots instead of the pixels, as discussed in Section 3.2.2.

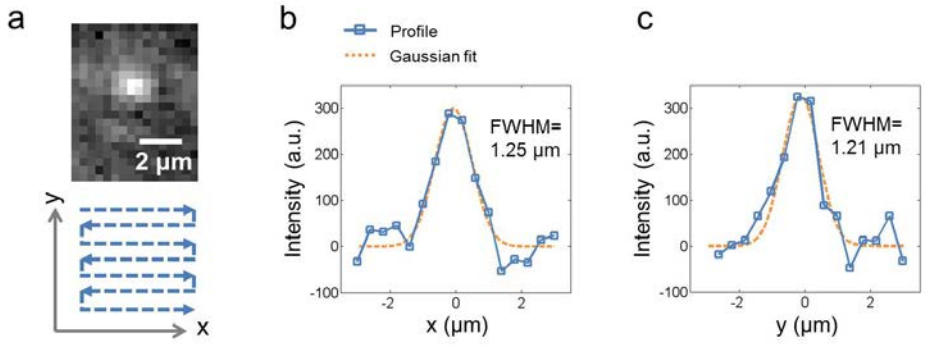

Figure 3.4. The resolution measurement. (a) A reconstructed image of the quantum dots defines the experimental point spread function (PSF). x is the direction of the scan lines. (b) The profile of the PSF and its Gaussian fit in x direction. (c) The profile of the PSF and its Gaussian fit in y direction.

3.5 Application of the Talbot microscope for the fluorescence imaging of cells and *C. elegans*

3.5.1 Wide FOV imaging of quantum dots labeled cells, GFP cells, and *C. elegans*

To demonstrate the wide FOV imaging capability of the Talbot microscope, we performed the fluorescence imaging of fixed human breast cancer cells (SK-BR-3), which have a cancer marker (Her2) in their membranes labeled by quantum dots (Qdot® 625, Life Technologies) (Figure. 3.5a─c). We also demonstrate the capability of the Talbot microscope to image HeLa cells expressing GFP in the nucleus (Figure 3.5d─f) and live *C. elegans* expressing GFP in the pharynx (Figure 3.5g─i). We chose 488 nm laser excitation for all these fluorophores, and the image sensor coated with red emission filter was used for Qdot® 625, while the ones coated with green emission filter were used for GFP. The FOV was set at 3.9×3.5 mm^2. Since the measured resolution was 1.2 μm, we chose the scan step size to be 0.60 μm in both x and y direction in accordance to the Nyquist sampling theorem. The exposure time for each step depended on the brightness of the sample. With approximately 1 μW on each focal spot, the exposure time for the SK-BR-3 cells, the HeLa cells, and the *C. elegans* was set at 12 ms, 16 ms, and 10 ms, respectively, in order to collect sufficient fluorescence signals. This results in a total scan time of less than 1 min. The data acquisition and storage time for the scanned images was ~ 4 -5 min, which was mainly limited by the sensor readout speed. We can notice that the subcellular structures are clearly discernible, such as cell membranes (Figure 3.5c), cell nuclei (Figure 3.5f), and fine features inside the pharynx of *C. elegans*. The body profile of the *C. elegans* in Figure 3.5h was plotted by directly capturing a brightfield image using white light illumination on the sensor, and overlaying this image with the high resolution fluorescence image.

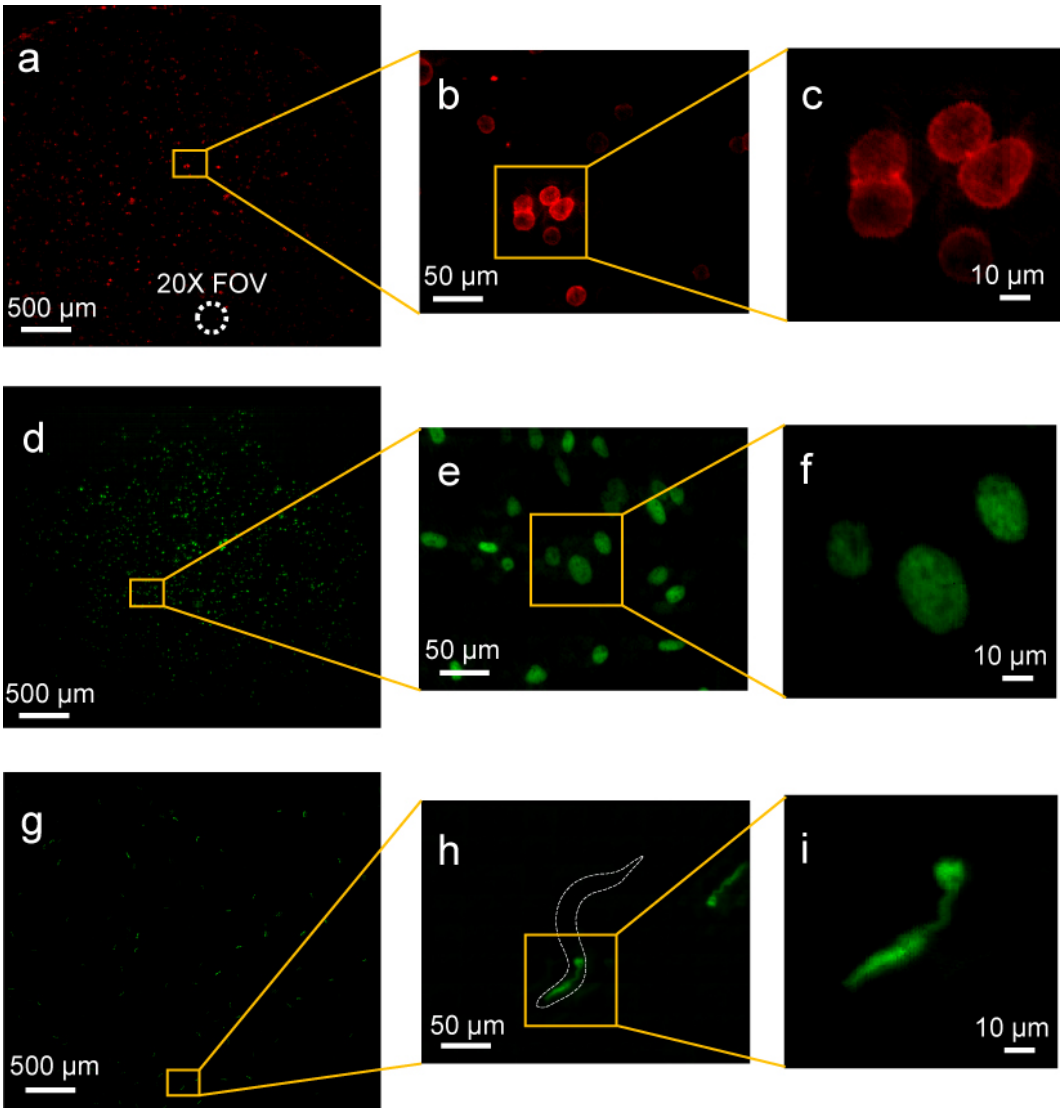

Figure 3.5. Wide field-of-view (FOV) fluorescence images by the Talbot microscope. (a─c) Fluorescence images of human breast cancer cells (SK-BR-3) with membranes stained by Qdot® 625. The full FOV image (a) is zoomed in to show details (b) and subcellular structures (c). (d─f) Fluorescence image of HeLa cells with GFP expression in the nuclei with the same arrangements as in (a─c). (g─i) Fluorescence image of *C. elegans* with GFP expression in the pharynx with the same arrangements as in (a─c).

3.5.2 Longitudinal imaging of *C. elegans* for distal tip cell (DTC) development

In the previous section we showed the wide FOV capability provided by our Talbot microscope. This can be very useful in high-throughput screening. To demonstrate this, we

simultaneously imaged a large number (~50) of adult *C. elegans* with GFP expression in their DTCs for the purpose of phenotyping their distal tip cell (DTC) migration. For creating different phenotypes, the RNA interference (RNAi) technology was used to induce deficiency in certain genes controlling DTC development. In order to image live *C. elegans* , we developed a method to immobilize them with hydrogel (see Section 3.9 for the protocol).

In the hermaphrodite *C. elegans*, the gonad achieves its final shape through the migration of two DTCs located at opposite ends of the developing gonad. Beginning at approximately 12 hours post-hatching, the DTCs migrate away from each other until ~29 hours post-hatching, then turn back, and migrate towards one another until they meet [15] (Figure 3.6a). Two genes are playing important roles in the DTC migration: *daf-12* encodes a transcription factor affecting developmental timing [16], while *gon-1* encodes a metalloprotease required for remodeling the basement membrane around the DTCs [17]. For *daf-12* mutant *C. elegans*, the DTCs appear normal in the beginning; however, after 28 h post-hatching, they keep migrating away from each other instead of turning back (Figure 3.6b). For *gon-1* mutant *C. elegans*, the DTCs do not migrate away from each other during development (Figure 3.6c).

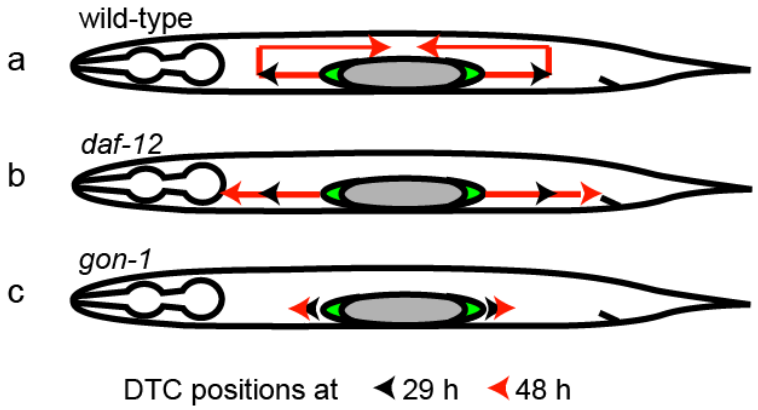

Figure 3.6. The distal tip cell (DTC) migration in *C. elegans*. (a) In wild-type hermaphrodite *C. elegans*, the DTCs migrate away from each other until ~29 hours post-hatching, then turn back and migrate towards one another until they meet. (b) In *daf-12* mutant *C. elegans*, the DTCs appear normal in the beginning, but they keep migrating away

from each other after 29 h post-hatching instead of turning back. (c) In *gon-1* mutant *C. elegans*, the DTCs do not migrate away from each other during development.

We applied our Talbot microscope to image the synchronized population of worms with GFP-labeled DTCs at two typical time points of the migration: 29 h and 48 h. The representative images are shown in Figure 3.7. The body profiles of the *C. elegans* in all the images were plotted by directly capturing brightfield images using white light illumination on the sensor, and overlaying the images with the high resolution fluorescence images. We observed that the migration behaviors of DTCs were consistent with the previous studies [15─17].

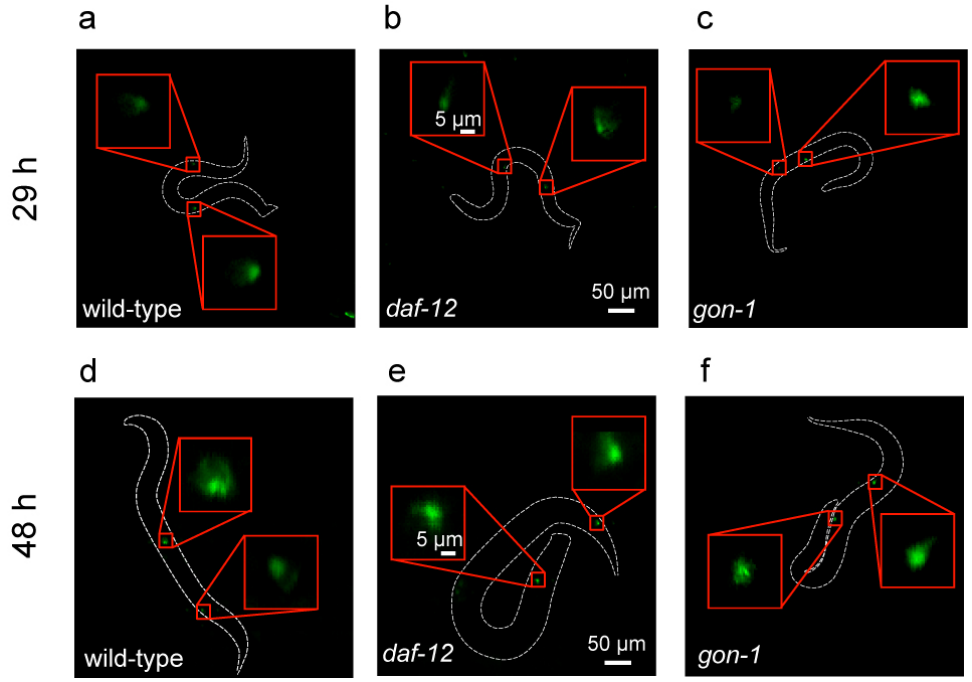

Figure 3.7. The Talbot microscope imaging of DTCs in *C. elegans*. Worm body profiles are shown in white dashed lines, and DTC regions are zoomed in. (a─c) The DTCs in wild-type, *daf-12* mutant, and *gon-1* mutant *C. elegans* at 29 h post-hatching. (d─f) The DTCs in wild-type, *daf-12* mutant, and *gon-1* mutant *C. elegans* at 48 h post-hatching.

In order to get quantitative data, we used the distance between the two DTCs as the readout of the progress in migration. From the statistics of the body length of the *C. elegans* and the distance between the two DTCs, we found that the mean distance between the DTCs is 147

± 40 μm at 29 h and 124 ± 65 μm at 48 h in wild-type animals (Figure 3.8). We also examined worms having two different types of migration defects. In the *daf-12* mutants, the DTCs migrated only slightly slower than wild-type at 29 h (116 ± 36 μm, P<0.001, Student's *t-test*), but at 48 h, the mean distance of 415 ± 124 μm (P<0.0001) indicated that the DTCs continued to migrate away from each other instead of turning back (Figure 3.7e). On the other hand, the *gon-1* mutants showed little migration after both 29 h (55±19 μm, P<0.0001) and 48 h (109±58 μm, P=0.29) (Figure 3.7c,f). The body lengths of wild-type and migration-defective animals were not significantly different (Figure 3.8).

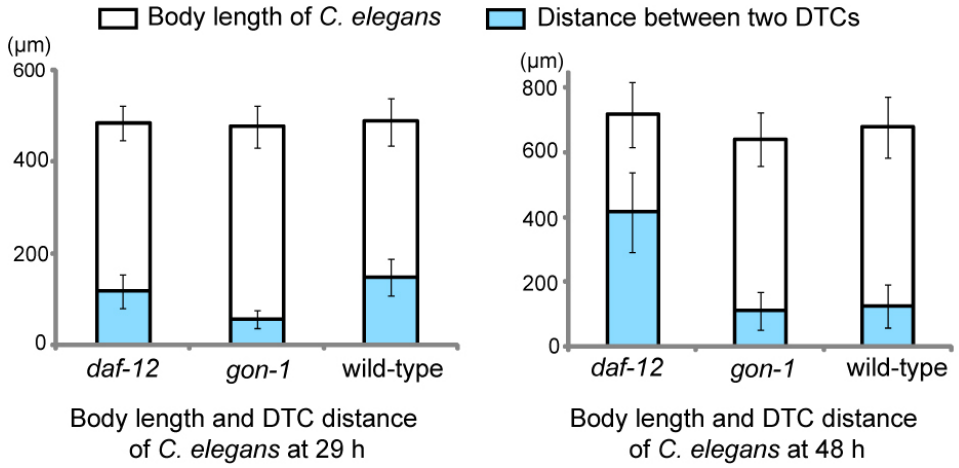

Figure 3.8. Statistics for the Talbot microscope imaging of *C. elegans* DTC migration. At 29 h, the body lengths of wild-type worms (N=35) are not significantly different from *daf-12* (N=40, P=0.75) and *gon-1* (N=42, P=0.31) mutants, while the DTC distances of the wild-types are slightly larger than the *daf-12* mutants (P<0.001), and much larger than the *gon-1* mutants (P<0.0001). At 48 h, the body lengths of the wild-types (N=38) do not have significant difference from the *daf-12* (N=30, P=0.09) and *gon-1* (N=38, P=0.08) mutants. The DTC distances of the wild-types are similar to the *gon-1* mutants (P=0.29), but significantly different from the *daf-12* mutants (P<0.0001).

3.6 Time-lapse imaging of GFP cells using the Talbot fluorescence ePetri system

In this section, we will introduce an updated version of the Talbot microscope, termed the Talbot fluorescence ePetri, for the purpose of long-term cell culture and time-lapse fluorescence imaging. The Talbot fluorescence ePetri is capable of performing wide FOV fluorescence imaging inside a standard humidified CO_2 incubator. By integrating an extra

microfluidic chamber on the filter-coated CMOS sensor chip, the perfusion cell culture is enabled during the imaging process.

3.6.1 System setup

Fabrication of the microfluidic-integrated image sensor

The microfluidic-integrated image sensor consists of a CMOS sensor and a microfluidic component, and was fabricated separately and assembled together. The 5.2 μm pixel-size CMOS image sensors (MT9M001C12STM, Aptina Imaging) were used. This sensor has 5.2 μm pixel size, and has a larger imaging area than the previously used 2.2 μm pixel sensor, which can provide more space to integrate with a microfluidic component. The cell culture chamber in the microfluidic component has a diameter of 5 mm and a height of 400 μm, with two channels as the inlet and outlet. The ceiling of the chamber is a glass coverslip. The microfluidic component was fabricated onto the filter-coated CMOS sensor in seven steps (Figure 3.9). Finally, the completed microfluidic component was attached to a coated CMOS sensor with the edges sealed by PDMS (Figure 3.9h), and two Tygon tubings are connected to the inlet and outlet for cell and medium loading (Figure 3.10a). Figure 3.10b shows the design of the microfluidic chamber.

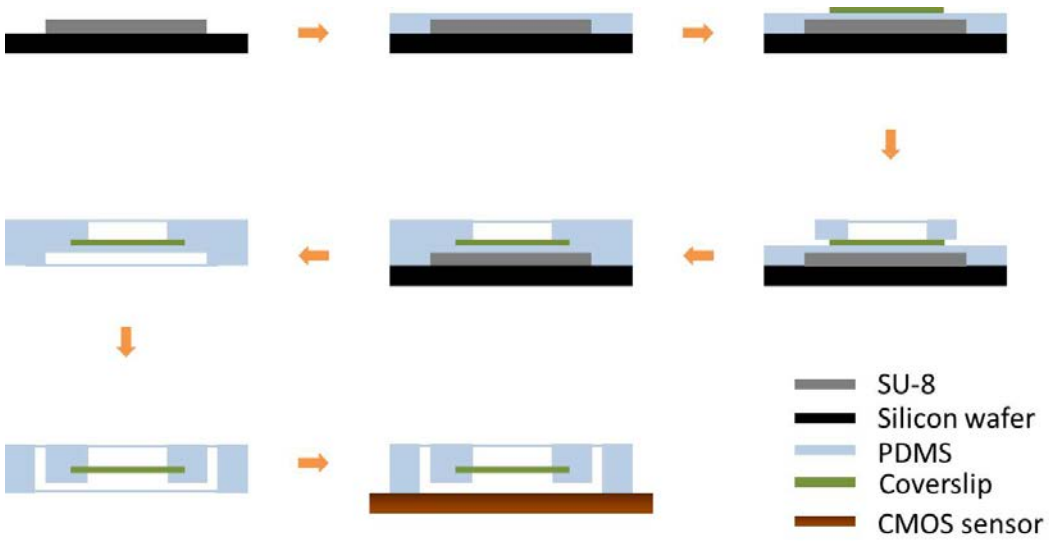

Figure 3.9. The fabrication process of the microfluidic component and its packaging with the image sensor. (a) SU-8 photoresist with a thickness of 200 μm was patterned onto a 3-inch silicon wafer to form a master. (b) Liquid PDMS prepolymer solution was poured

onto the master and cured at 80 °C for 1 h. (c) A 5 mm diameter coverslip was aligned and attached above the SU-8 culture chamber pattern. (d) Another PDMS block with a 4 mm diameter hole was aligned and attached to the coverslip. (e) The PDMS prepolymer was again poured onto the first PDMS layer, and cured at 80 °C for 1 h to fill the gap around the coverslip. (f) The whole PDMS structure was peeled off from the master. (g) The PDMS layer beneath the coverslip was removed and the 4 mm diameter hole above the coverslip was enlarged to 5 mm. A 1 mm hole was punched at the end of each channel to form the inlet and outlet. (h) The structure was attached to a filter-coated CMOS sensor with the edges sealed by PDMS.

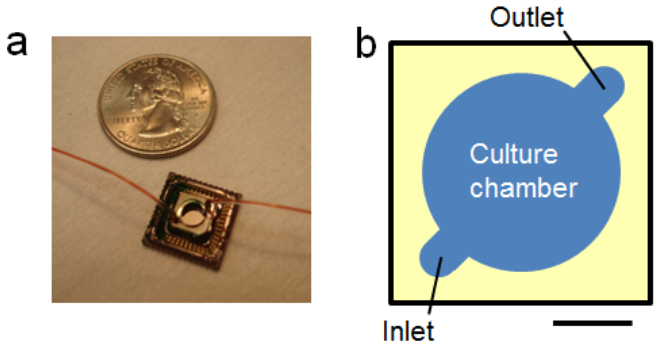

Figure 3.10. The microfluidic-integrated image sensor. (a) A photo of the packaged sensor chip. (b) The design of the microfluidic cell culture chamber with an inlet and an outlet

Assembling the Talbot fluorescence ePetri system

The microfluidic-integrated image sensor was connected with a self-priming micro-pump (EW-73120-64, Cole-Parmer), and fresh medium was loaded into the microfluidic culture chamber every 10 min. The maximum flow speed was set below 50 μm/s, which is within the suggested range for perfusion culture [18]. The illumination, image data acquisition, and micro-pump were all automatically controlled by a customized LabVIEW program. The Talbot fluorescence ePetri system was rebuilt using standard optical mounts and stages (Thorlabs) to improve the stability during long-term imaging in humid environment. The assembled system is shown in Figure 11. The full dimensions of the system are ~20 × 20 × 20 cm^3 – we note that the size can be significantly reduced for future versions. All the

following experiments were conducted within a humidified 5% CO2 incubator at 37 ^{0}C. The data was streamed from the incubator via a CAT-6 Ethernet cable.

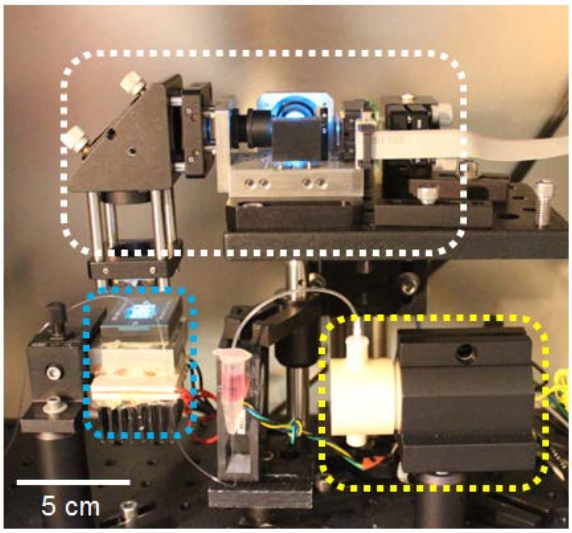

Figure 3.11. The assembled Talbot fluorescence ePetri system. White rectangle: the illuminator; blue rectangle: the microfluidic-integrated image sensor, socket, and TEC; yellow rectangle: the micro-pump.

3.6.2 Temperature control

As previously mentioned, to provide an adequate cell culture environment, the imaging platform was placed inside a humidified 5% CO_2 incubator at 37 ^{0}C. We turned on the TEC during imaging to prevent the sensor surface temperature from exceeding 37 ^{0}C. We measured the temperature on the CMOS sensor surface using a thermal couple 76 μm-diameter T-type thermocouple (Omega) inserted into the cell culture chamber from the inlet, and read the temperature data automatically into the computer using a universal connector (UTC-USB, Omega), with the data shown in Figure 3.12. Without the TEC cooling, there was an overshoot of temperature up to 40^{0}C during the imaging process. With the TEC cooling at 7W, the overshoot decreased to 38.5 ^{0}C. With the TEC cooling at 13 W, the temperature was controlled below 37 ^{0}C. Therefore, we set our TEC power at 13 W for our live cell time-lapse imaging experiments.

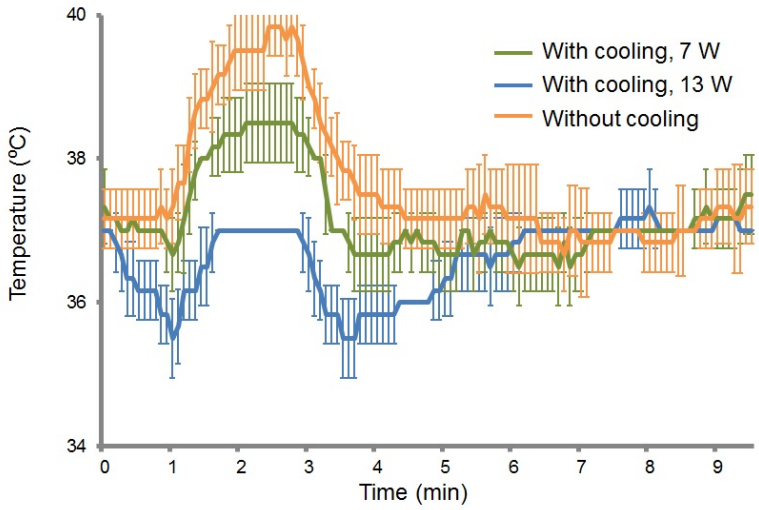

Figure 3.12. The measurement of sensor surface temperature during the imaging process. Six measurements were repeated in total. The 0-1.0 min is for pre-cooling, 1.0-2.4 min for imaging, and 2.4-2.9 min for data storage.

3.6.3 Imaging of cell cycles

As an initial demonstration, we chose HeLa cells expressing H2B-eGFP in their nuclei as our imaging targets. The cells were cultured on the image sensor surface, and a 3.7 mm x 3.5 mm FOV was imaged (Figure 3.13a). The scan step size was set at 0.6 μm. It took 85 s to scan the entire FOV, and 30 s to perform data readout and storage. Typical cells in G1, G2, metaphase, and anaphase stages could be recognized in this image (Figure 3.13b1,c1,d1,e1). The nucleoli were also recognizable as the dark regions inside the nuclei, where the H2B proteins were absent (Figure 3.13b1,c1). For comparison, the same cells were imaged under a standard microscope with a 20x/0.4 NA objective (Figure 3.13b2,c2,d2,e2). The resolution of the FTM system was adequate for us to distinguish the four different stages (G1, G2, metaphase, and anaphase) in the cell cycle.

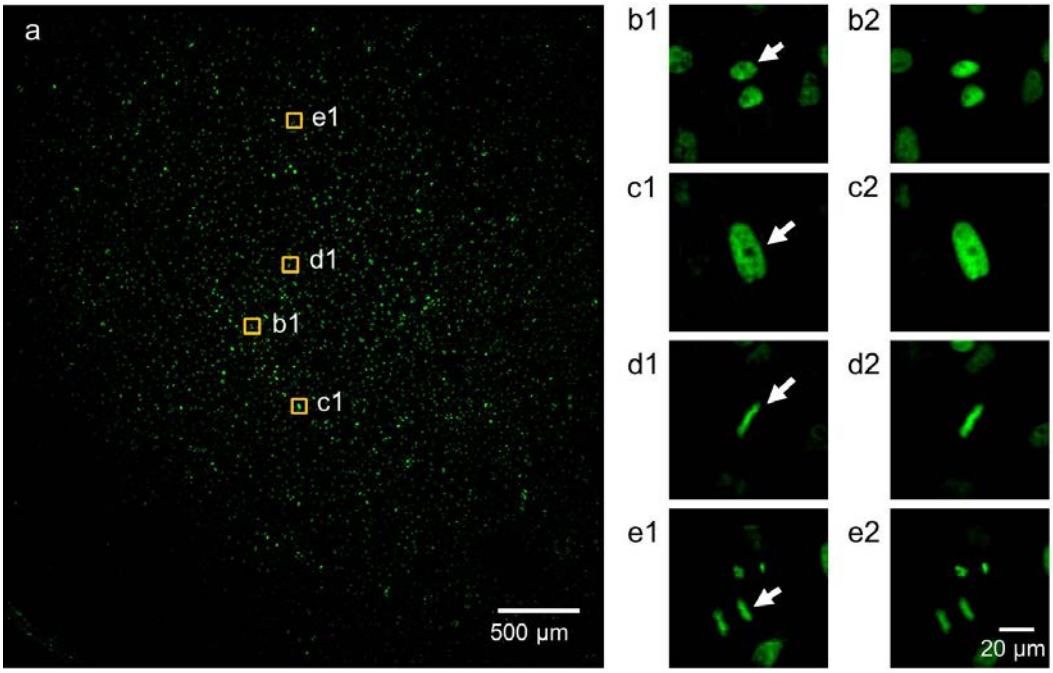

Figure 3.13. Wide FOV fluorescence imaging of the GFP cells. (a) The 3.7 mm x 3.5 mm image. (b1, c1, d1, e1) Cropped images of typical cells in (a), including G1 (b1), G2 (c1), metaphase (d1), and anaphase (e1) (arrows). (b2, c2, d2, e2) The same cells as imaged by a conventional microscope with a 20x/0.4 NA objective.

3.6.4 Automatic cell recognition and tracking

To demonstrate the system's longitudinal study capability, we employed it to acquire a sequence of images at 33 min intervals over a total duration of 24.8 hours. After reconstructing the image sequence, we extracted the outline of each nucleus from the background by thresholding and the application of watershed segmentation algorithm [19] (Figure 3.14). We first evaluated the segmentation accuracy by processing six 1 mm x 1 mm reconstructed sample images, and compared the results with manual segmentation. Among the segmented objects, the algorithm had an accuracy of 96.1±2.2% (1304 objects; 3.3±1.7% oversegmented (falsely cut) and 0.7±0.5% undersegmented (falsely merged)). There were 5.8±2.3% cells that were not bright enough to be recognized by the algorithm. We then used the nearest-neighbor tracking method on the segmented images [20], which finds the next position of each cell by searching its neighborhood in the next frame. A threshold for the neighbor range was defined according to the image sequence to optimize the tracking results. Newly divided cells were given a new tag.

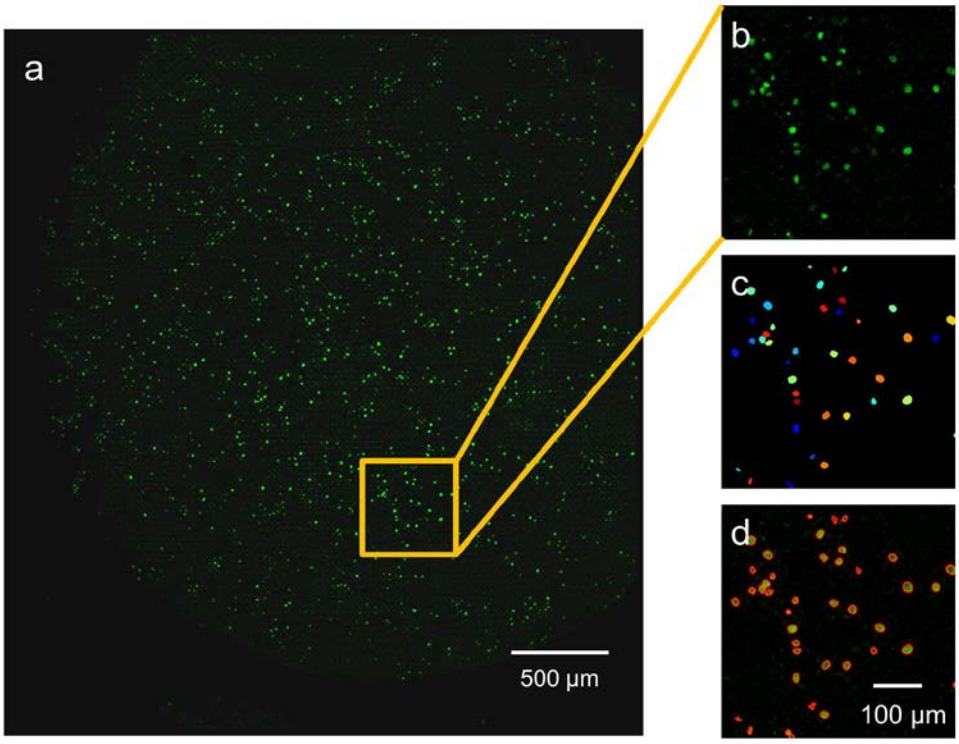

Figure 3.14. Cell segmentation and counting using the watershed algorithm. (a) The reconstructed high resolution image. (b) A typical region from (a). (c) The result of the segmentation by the watershed algorithm. (d) The segmentation result overlaid with the original image.

The trajectories for each tracked cell over 24.8 h were then plotted (Figure 3.15a). Figure 3.15b shows a zoomed-in vignette illustrating our capacity to perform single cell tracking. This cell migrated in the bottom-right direction, divided at 5.5 h (marked by *), and the two daughter cells started to migrate in opposite directions. At 24.8 h, the daughter cell that was moving upwards divided again (marked by **). By using the trajectory information, we can also automatically crop each cell out of the original wide FOV image sequence (Figure 3.15c).

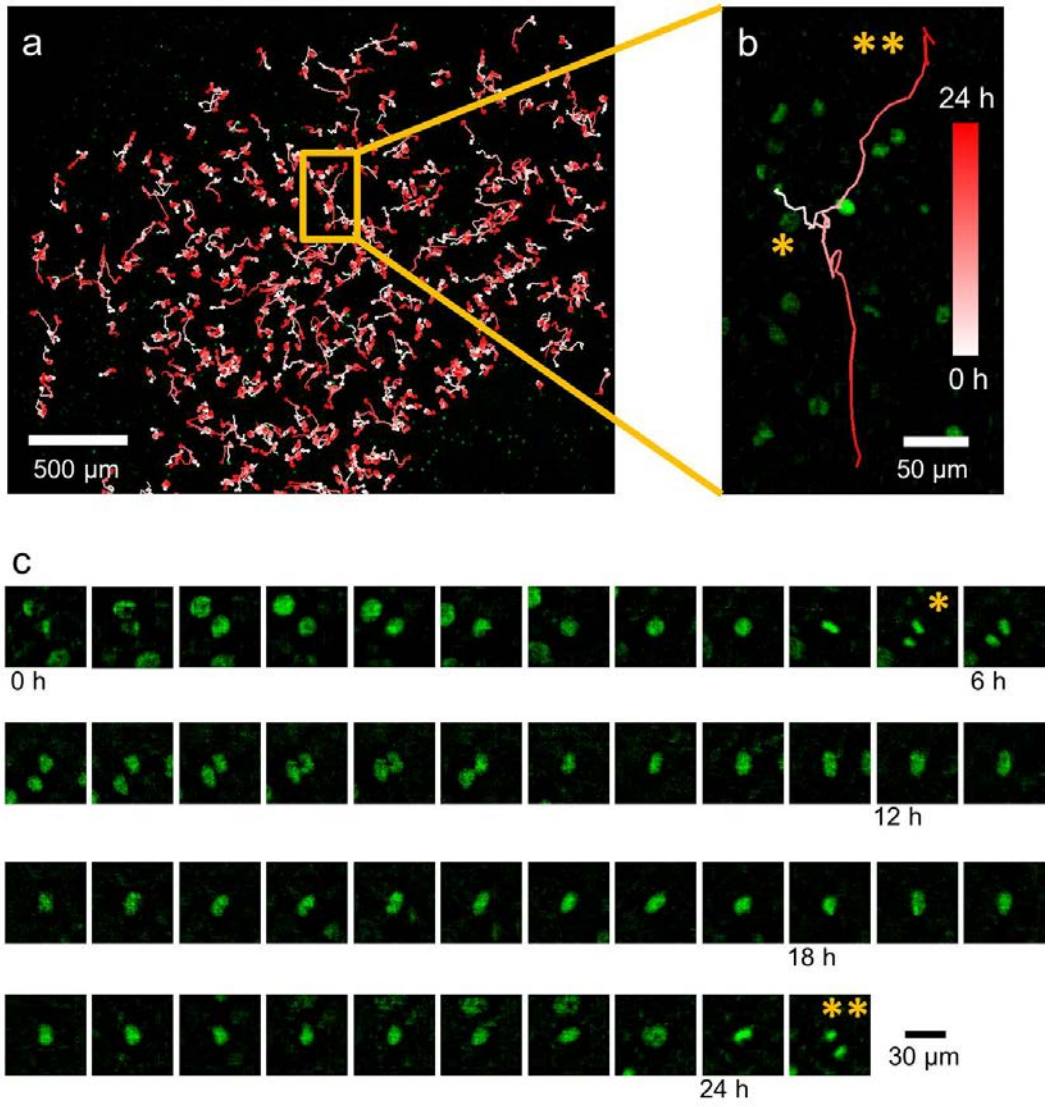

Figure 3.15. Longitudinal imaging of the GFP cells. (a) Trajectories of cells over 24.8 hours. The position of a cell at each time point is illustrated by its color. (b) The trajectory showing a single cell which divided at 5.5 h (*), with one of the daughter cells that moved upwards dividing again at 24.8 h (**). (c) Longitudinal images of the cell in (b) as it migrated and divided. The asterisks indicate the cells in anaphase at 5.5 h (*) and 24.8 h (**) during the division events.

3.6.5 Quantitative study of camptothecin treatment

Drug study is an excellent longitudinal study format for which an inexpensive, high-resolution and wide FOV fluorescence imaging system can significantly improve the efficiency. As a demonstration of such an application, we performed the following

experiment with camptothecin (CPT), a well-characterized anti-cancer drug. CPT inhibits DNA and RNA replication and synthesis by targeting the nuclear enzyme topoisomerase I [21]. Analogues of CPT have been successfully used in cancer chemotherapy [22].

Here we used our system to investigate HeLa cell division and migration behaviors in response to CPT. In this longitudinal study, we prepared two cell culture groups: the CPT treatment group and the control group. For the CPT group, cell culture medium with 1 μM CPT was loaded into the microfluidic culture chamber at 0 h. The control group was loaded with the medium without CPT. Wide FOV images were taken at 33 min intervals over a total duration of 21.5 hours. We performed watershed segmentation to count the number of cells in each image. At 0 h, the control and CPT group were counted to have 1158 and 1297 cells, respectively. At 21.5 h, the cell count for control group increased 52.4% while the cell count for CPT group increased 10.5% (Figure 3.16a). We then tracked 373 and 422 cells in the control and CPT groups, respectively, and calculated the migration distance of each cell over the 21.5 hours. The cells in the control and CPT groups had average migration distances of 246.0±59.2 μm and 210.3±68.5 μm, respectively, showing a significant difference from the Student's t-test ($P<0.001$) (Figure 3.16b). Representative time-lapse images are shown in Figure 3.16c. From these data, we can conclude that CPT inhibits cell proliferation and migration, and the Talbot Fluorescence ePetri system can be used for automate drug testing and cell behavior analysis.

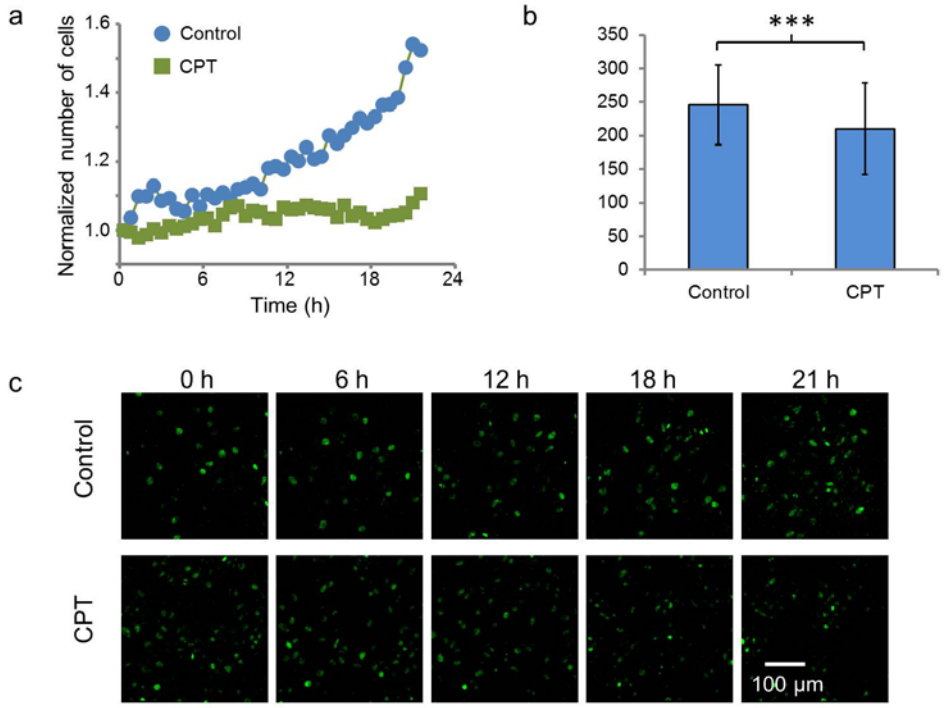

Figure 3.16. Effect of camptothecin (CPT) treatment. (a) Cell count over time for the control group and the CPT group. (b) Average cell migration distances for the control group and the CPT group over 21.5 hours (***P<0.001). (c) Representative images for the two groups at 0, 6, 12, 18, and 21 h.

3.7 Discussion

In the context of wide FOV imaging, the currently Talbot microscope prototype is slower than state-of-the art commercial large-area fluorescence scanning systems, such as Olympus VS120-SL. This is due to the fact that the low-cost sensor chip has limited frame rate and is less sensitive than the high-performance camera used in commercial scanning systems. In addition, our current sensor chip and board do not support pixel binning functions, which can significantly enhance the frame rate and readout speed. By switching to a sensor chip with higher frame rate and binning function, we can expect a significant imaging speed improvement.

We would like to further emphasize the scalability of the FOV for this imaging design. The FOV of the Talbot microscope only depends on the area of the lenslet array and the area of the image sensor, therefore it can be enlarged by simply employing a larger lenslet array and a larger sensor chip. Furthermore, unlike with conventional scanning microscopes, the

total scanning time would remain the same rather than scaling linearly with the area covered.

The Talbot Fluorescence ePetri approach requires an undistorted projection of the Talbot generated light spots on the sample. As PDMS is porous and vulnerable to deformation, a microfluidic reservoir comprised entirely of PDMS could significantly degrade the achieved resolution. To mitigate this, we developed a fabrication method for implementing a glass/PDMS hybrid microfluidic component, as described in the Experimental section. Here we incorporated a glass cover as the top of the reservoir to preserve the quality of the Talbot light spots. For our demonstration experiment, the current reservoir design consisted only of a center culture chamber and two ports. It is possible to integrate more sophisticated microfluidic functions into the system. For example, it would be possible to implement multiple branch channels to generate a stable chemical gradient [23] to study the response of cells to different concentrations of chemical signals. We can also include microvalves [24] to modulate the amount of drug delivery over time and investigate the resulting cell dynamics.

In our Talbot Fluorescence ePetri system, we observed that the fluorescence intensity of the H2B-eGFP varied as a cell went through different stages in the cell cycle: it was very bright during mitosis when the chromosomes were highly condensed, but became very dim in early interphase (such as G1 phase) when H2B was diffuse in the nuclei. This may explain the fact that 5.8±2.3% of the cells cannot be recognized by our segmentation algorithm. We tracked ~30% of the brightest cells of the whole population throughout the time-lapse imaging process in our CPT treatment experiment to avoid errors in our statistics for the migration speed. In this study, the main focus was on the demonstration of the Talbot Fluorescence ePetri platform, and we expect that more advanced algorithms can be used to track a larger percentage of cells. For example, we can implement trajectory repair processes in our tracking algorithm, which connects the broken trajectories if the positions where a cell disappears and reappears are within a certain neighborhood. Furthermore, the typical cell cycle stages (such as metaphase, anaphase, G1, and G2) can be automatically recognized by introducing machine vision techniques such as the support vector machine (SVM) [19]. The cell annotation over a wide FOV is likely useful for a host of bioscience studies.

3.8 Conclusion

As a conclusion, in this chapter we demonstrated the utility of the Talbot microscope and an upgraded Talbot Fluorescence ePetri for high throughput live cell imaging, phenotyping, and drug study applications. The Talbot microscope has a FOV of 13 mm^2 and a resolution limit of 1.2 μm. Our on-chip system is simple in implementation, low cost, integratable with microfluidic devices, and compact enough to be placed inside a standard incubator. We believe our system can also find significant applications in many emerging fields such as tissue engineering and stem cell differentiation where the longitudinal study of a large number of living samples is needed.

3.9 Experimental section

3.9.1 Preparation of Qdot ®-stained SK-BR-3 cells

The human breast cancer cell line SK-BR-3 was purchased from American Type Culture Collection (ATCC). Cells were cultured at 37 °C, 5% CO2 in McCoy's 5A medium (ATCC) with 10% fetal bovine serum (FBS, Invitrogen). Before experiment, cells were fixed with 4% formaldehyde for 5 min, and incubated sequentially with mouse anti-HER2 (c-erbB-2) antibody (Invitrogen) for 1 h and 5 nM Qdot® 625 goat F(ab')2 anti-mouse IgG conjugate (Invitrogen) for 1 h, then washed with Dulbecco's phosphate-buffered saline (DPBS, Invitrogen). Before experiment, cells were mounted on a red filter-coated sensor with a 5 mm-diameter coverslip on top. Mineral oil was then filled at the edge of the coverslip to avoid evaporation.

3.9.2 Preparation of HeLa cells expressing GFP

HeLa cells (ATCC) were infected at approximately 35% confluence with VSVG-pseudotyped lentivirus to obtain cells ubiquitously expressing GFP fused to histone-2B (H2B), driven by the chicken beta-actin-CMV (CAG) promoter. Stably infected cells were propagated in DMEM (Cellgro) supplemented with 10% FBS (Cellgro).

3.9.3 Preparation of live *C. elegans*

For the imaging of pharynx, the C. elegans strain PS5643 syIs231 [hs:LIN-3C , myo-2::GFP]; him-5 was cultured at 22°C using standard protocols [25]. The eggs were harvested from PS5643 gravid adults by bleaching and placed on plates, and the worms were allowed to develop at 22°C to L1 stage.

For the phenotyping of DTC development, the C. elegans strain JK2868 qIs56 [lag-2::GFP; unc-119(+)] was cultured at 22°C. The eggs were harvested from JK2868 gravid adults by bleaching and placed on plates containing either *daf-12* RNAi bacteria, *gon-1* RNAi bacteria, or bacteria without an RNAi construct, and the worms were allowed to develop at 22°C.

The RNAi bacteria were obtained from the Ahringer Library (Geneservice), and their RNAi feeding protocol was used with modifications [26]. RNAi feeding plates were made by spreading carbenicillin at 25 μg/mL and IPTG at 1 mM final concentration on agar plates, and adding RNAi liquid bacterial culture. The plates were either used the following day or stored at 4°C.

The C. elegans worms were immobilized on the CMOS sensor using hydrogel by modifying established protocols [27]. Briefly, hydrogel prepolymer solution was prepared by adding 20% (wt/wt) poly(ethylene glycol) 1000 dimethacrylate (PEG-DMA, Polysciences) in DPBS, then 1% (wt/wt) Irgacure 2959 (2-hydroxy-1-(4-(hydroxyl-ethoxy) phenyl)-2-methyl-1-propanone, BASF) as the photoinitiator. The worms were washed into the hydrogel prepolymer solution, and a 2 μL worm suspension was mounted onto the green filter-coated sensor with a 5 mm-diameter coverslip on top. A UV exposure of ~10 mW cm^{-2} at 365 nm for 1 min was applied to induce gelation.

3.9.4 Microfluidic cell culture and time-lapse imaging

The microfluidic-integrated image sensor was treated with Poly-L-lysine solution (Sigma-Aldrich) overnight for better cell attachment. Upon experiment, the cell solution was adjusted to a concentration of 1×10^6 cells/ml, and loaded into the microfluidic device. After 4 h of incubation to permit the cells to attach to the image sensor surface, the image sensor was mounted onto the socket for imaging.

REFERENCES

1. Q. Zhong, A. G. Busetto, J. P. Fededa, J. M. Buhmann, and D. W. Gerlich, "Unsupervised modeling of cell morphology dynamics for time-lapse microscopy," Nat Methods **9**, 711-713 (2012).
2. Y. E. Kim, J. Chen, J. R. Chan, and R. Langen, "Engineering a polarity-sensitive biosensor for time-lapse imaging of apoptotic processes and degeneration," Nat Methods **7**, 67-73 (2010).
3. A. A. Cohen, N. Geva-Zatorsky, E. Eden, M. Frenkel-Morgenstern, I. Issaeva, A. Sigal, R. Milo, C. Cohen-Saidon, Y. Liron, Z. Kam, L. Cohen, T. Danon, N. Perzov, and U. Alon, "Dynamic Proteomics of Individual Cancer Cells in Response to a Drug," Science **322**, 1511-1516 (2008).
4. T. Schroeder, "Long-term single-cell imaging of mammalian stem cells," Nat Methods **8**, S30-35 (2011).
5. A. F. Coskun, I. Sencan, T. W. Su, and A. Ozcan, "Lensfree fluorescent on-chip imaging of transgenic Caenorhabditis elegans over an ultra-wide field-of-view," PLoS One **6**, e15955 (2011).
6. S. A. Arpali, C. Arpali, A. F. Coskun, H. H. Chiang, and A. Ozcan, "High-throughput screening of large volumes of whole blood using structured illumination and fluorescent on-chip imaging," Lab Chip **12**, 4968-4971 (2012).
7. K. Patorski, "The Self-Imaging Phenomenon and Its Applications," Progress in Optics **27**, 3-108 (1989).
8. A. Orth and K. Crozier, "Microscopy with microlens arrays: high throughput, high resolution and light-field imaging," Opt Express **20**, 13522-13531 (2012).
9. G. A. Zheng, S. A. Lee, Y. Antebi, M. B. Elowitz, and C. H. Yang, "The ePetri dish, an on-chip cell imaging platform based on subpixel perspective sweeping microscopy (SPSM)," Proc Natl Acad Sci U S A **108**, 16889-16894 (2011).
10. H. F. Talbot, "Facts relating to optical science" No. IV, Philos. Mag. 9 (1836).
11. J. W. Goodman, "Introduction to Fourier optics," Roberts & Company Publishers (2005).
12. F. Pfeiffer, T. Weitkamp, O. Bunk, and C. David, "Phase retrieval and differential phase-contrast imaging with low-brilliance X-ray sources," Nat Phys **2**, 258-261 (2006).
13. M. Testorf, J. Jahns, N. A. Khilo, and A. M. Goncharenko, "Talbot effect for oblique angle of light propagation," Opt Commun **129**, 167-172 (1996).
14. S. Pang, C. Han, L. M. Lee, and C. H. Yang, "Fluorescence microscopy imaging with a Fresnel zone plate array based optofluidic microscope," Lab Chip **11**, 3698-3702 (2011).
15. J. Kimble and D. Hirsh, "The postembryonic cell lineages of the hermaphrodite and male gonads in Caenorhabditis elegans," Developmental biology **70**, 396-417 (1979).
16. A. Antebi, J. G. Culotti, and E. M. Hedgecock, "daf-12 regulates developmental age and the dauer alternative in Caenorhabditis elegans," Development **125**, 1191-1205 (1998).
17. R. Blelloch and J. Kimble, "Control of organ shape by a secreted metalloprotease in the nematode Caenorhabditis elegans," Nature **399**, 586-590 (1999).
18. L. Kim, Y. C. Toh, J. Voldman, and H. Yu, "A practical guide to microfluidic perfusion culture of adherent mammalian cells," Lab Chip **7**, 681-694 (2007).

19. M. Held, M. H. Schmitz, B. Fischer, T. Walter, B. Neumann, M. H. Olma, M. Peter, J. Ellenberg, and D. W. Gerlich, "CellCognition: time-resolved phenotype annotation in high-throughput live cell imaging," Nat Methods **7**, 747-754 (2010).
20. A. J. Hand, T. Sun, D. C. Barber, D. R. Hose, and S. MacNeil, "Automated tracking of migrating cells in phase-contrast video microscopy sequences using image registration," J Microsc **234**, 62-79 (2009).
21. Y. H. Hsiang, R. Hertzberg, S. Hecht, and L. F. Liu, "Camptothecin induces protein-linked DNA breaks via mammalian DNA topoisomerase I," J Biol Chem **260**, 14873-14878 (1985).
22. R. Garcia-Carbonero and J. G. Supko, "Current perspectives on the clinical experience, pharmacology, and continued development of the camptothecins," Clin Cancer Res **8**, 641-661 (2002).
23. X. A. Figueroa, G. A. Cooksey, S. V. Votaw, L. F. Horowitz, and A. Folch, "Large-scale investigation of the olfactory receptor space using a microfluidic microwell array," Lab Chip **10**, 1120-1127 (2010).
24. B. G. Chung, F. Lin, and N. L. Jeon, "A microfluidic multi-injector for gradient generation," Lab Chip **6**, 764-768 (2006).
25. S. Brenner, "The genetics of Caenorhabditis elegans," Genetics **77**, 71-94 (1974).
26. R. S. Kamath, M. Martinez-Campos, P. Zipperlen, A. G. Fraser, and J. Ahringer, "Effectiveness of specific RNA-mediated interference through ingested double-stranded RNA in Caenorhabditis elegans," Genome Biol **2**, research0002 (2001).
27. F. Yanagawa, H. Kaji, Y. H. Jang, H. Bae, D. Yanan, J. Fukuda, H. Qi, and A. Khademhosseini, "Directed assembly of cell-laden microgels for building porous three-dimensional tissue constructs," J Biomed Mater Res A **97**, 93-102 (2011).

Chapter 4

A WIDE FIELD-OF-VIEW SCANNING ENDOSCOPE FOR ANAL CANAL SCREENING

In Chapter 2 and Chapter 3, we introduced two wide field-of-view (FOV) on-chip microscopes for the time-lapse imaging of dynamic processes in biological samples, including viral plaque development and cell growth and migration. In this chapter, we aim to explore the wide FOV technologies on a larger scale: the imaging of live tissues. We will report a novel wide FOV scanning endoscope, named the AnCam, which is based on the contact image sensor (CIS) technology used in commercial business card scanners. The AnCam can capture the whole image of the anal canal within 10 seconds with a resolution of 89 μm, a maximum FOV of 100 mm × 120 mm, and a depth-of-field (DOF) of 0.65 mm at 5.9 line pairs per mm (lp/mm). We will demonstrate the performance of the AnCam by imaging the entire anal canal of pigs and time-lapse tracking the dynamics of acetowhite testing. We believe the AnCam can potentially be a simple and convenient solution for screening of the anal canal for dysplasia and for surveillance in patients following treatment for anal cancer. This chapter is adapted from C. Han, J. Huangfu, L. Lai, and C. H. Yang, "A Wide Field-of-view Scanning Endoscope for Whole Anal Canal Imaging", *Biomed. Opt. Express* **6**, 607-614 (2015).

4.1 Background

Anal cancer is a malignancy of the epithelium of the anal canal [1]. As a malignancy that is associated with human papilloma virus (HPV) infection, the incidence of anal canal cancer has increased markedly over the last two decades [2,3]. Although screening for anal cancer results in early detection, screening of at-risk populations has not been widely adopted. The current gold standard for anal cancer screening is high resolution anoscopy (HRA), a technique adapted from standard cervical examination protocols [4–7]. In brief, the procedure is conducted as follows: 3–5% acetic acid is applied, using a soaked gauze, into the anal canal for at least one minute. The gauze is removed and a clear plastic anoscope is passed into the anal canal to retract soft tissues away and to allow the anal mucosa to be evaluated. The colposcope is positioned and used to identify abnormal areas delineated by acetic acid and labeled as "acetowhite" areas. These areas are biopsied to obtain a

histological confirmation of the abnormality. A handwritten map and photographs of abnormal areas document the location, appearance, and clinical impression of the biopsied areas.

Although HRA is the current standard examination used to screen for anal cancer, the technique has significant limitations. A typical colposcope has an adjustable magnification of 3×–17× with a 13–84-mm diameter FOV (Olympus OCS-3). However, the geometry of the anal canal allows the colposcope to only view small areas of the anal canal at any given time. To complete the entire examination, the colposcope would have to be moved and refocused multiple times. In addition, the ability to identify abnormal from normal tissues is dependent on the skill level of the practitioner and the number of biopsies taken during the examination. Lastly, the exam is charted manually. Digital photographs of areas of concern are highly desirable for serial follow-up but are logistically difficult to implement well. Taken together, the entire procedure is time consuming, with an average of more than 30 minutes per exam, requires multiple steps in its set up and execution, depends on the skill set of the provider to identify abnormal areas requiring biopsies, and demands high levels of histopathologic resources for support. A simpler, cheaper, and better alternative for imaging the anal canal for screening purposes is needed.

In recent years, contact image sensor (CIS) technology has been widely used within commercialized flatbed scanners and business card scanners, where a SELFOC lens array (SLA) is used to create a 1:1 image of the document onto a linear image sensor. Recently, CIS has been explored as a low cost solution for wide FOV biomedical imaging [8,9]. Zheng, *et al*. built a wide FOV brightfield scanning microscopy system based on a closed-circuit television (CCTV) lens for image magnification and a flatbed scanner for image acquisition [8]. Göröcs, *et al*. achieved wide FOV fluorescence imaging by adding an excitation light source and an emission filter to the flatbed scanner [9].

In this chapter, we will describe a novel anal imaging device developed by adapting a CIS that is disassembled from a low-cost business card scanner for imaging of cylindrical inner surfaces such as the anal canal. We have named this device the AnCam, and will describe its setup in detail and establish its resolution and DOF performance. Next, we will report a series of animal model experiments comparing the images of the AnCam with the

conventional colposcope in the evaluation of the anal canal. We will demonstrate the use of the AnCam in time-lapse imaging of acetic acid-induced changes of the anal canal to show the dynamic changes resulting from the use of acetic acid on the epithelium as well as the reproducibility of the serial images. Finally, we will present an upgraded AnCam with disposable tube design prepared for anal canal screening in patients. To our knowledge, this is the first report of an imaging device for capturing the circumferential inner cylindrical surface of the anal canal.

4.2 System setup

System setup for the AnCam is shown in Figure 4.1, and its basic imaging principle is illustrated in Figure 4.1a. The imaging module consists of a light source, an SLA, and a linear image sensor. The light source contains red, green, and blue (RGB) light-emitting diodes (LEDs) coupled to a light guide, which provides uniform illumination along its entire length. The SLA is a linear collection of cylindrical lenses (GRIN lenses) (Figure 4.1b). The light source illuminates the sample of interest, and the SLA is capable of performing good 1:1 imaging (without magnification) and of projecting a strip segment of the sample onto the linear image sensor. In order to obtain an image of the anal canal, which has a cylindrical surface, we incorporated the imaging module into a transparent tube, and carefully realigned the SLA and linear image sensor to fit the geometry of the tube and to ensure the sample on the outer surface of the tube is imaged correctly onto the image sensor. At each step, the imaging module collects one line of image information under three color channel illumination. Via the rotational scan of the imaging module at a constant speed for 360° inside the polycarbonate tube, we obtain a 2D RGB image of the sample throughout the tube surface.

Our AnCam system design and prototype are shown in Figure 4.1c and 4.1d, respectively. The imaging module was directly modified from a CIS that was disassembled from a palm-sized business card scanner (Opticard 821, Plustek). All of the components of the imaging module were then realigned and mounted onto an axis, and fixed inside a polycarbonate tube with a 38.1-mm outer diameter. The holders for the imaging module and the tip of the tube were all made of polylactide (PLA) and fabricated by a 3D printer (MakerBot Replicator 2). The axis was connected to a geared stepper motor (28BYJ-48, Kootek), which was controlled by a microcontroller (Arduino UNO) with a motor shield. The

imaging module was driven by the card scanner's own software for LED illumination and image capture, and the rotational speed of the motor was set at 0.68 rad/sec to be synchronized with image acquisition. The noise from the linear image sensor was removed by taking the fast Fourier transform (FFT) of the scanned image and then suppressing its abnormal frequency components (in MATLAB).

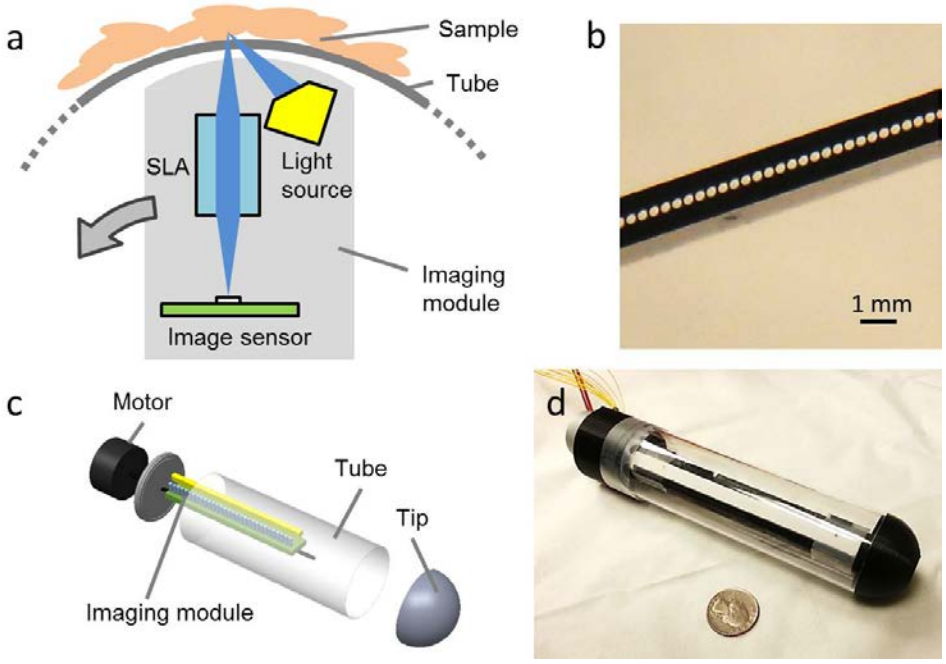

Figure 4.1. The AnCam system setup. (a) The imaging principle of the AnCam. (b) The SELFOC® lens array (SLA) inside the imaging module of the AnCam. (c) The design of the AnCam. (d) A prototype of the AnCam.

4.3 Resolution

To verify the resolution of our AnCam, we printed Groups 0–3 of the 1951 USAF resolution target on a transparency film (CAS/Art Services, Inc.) and attached it onto the tube surface for scanning (Figure 4.2). The scan was performed along the y direction. As shown in Figure 4.2b–d, the element with 11.3 line pairs per mm (lp/mm, corresponding to 88.5-µm line spacing) is the smallest discernible element; therefore, we can establish a resolution of 89 µm. This resolution is consistent with the image sensor's Nyquist sampling limit of 85 µm, considering that the pixel pitch for the sensor is 42.3 µm (600 dpi). The line visibility in the collected images and the close fit of the observed AnCam resolution to the

Nyquist resolution limit suggest that the sensor pixel pitch, rather than the optical imaging scheme, was the resolution-limiting factor in our sample. In other words, the AnCam would likely be able to achieve a finer resolution if the sensor were to be replaced with one of a denser pixel pitch.

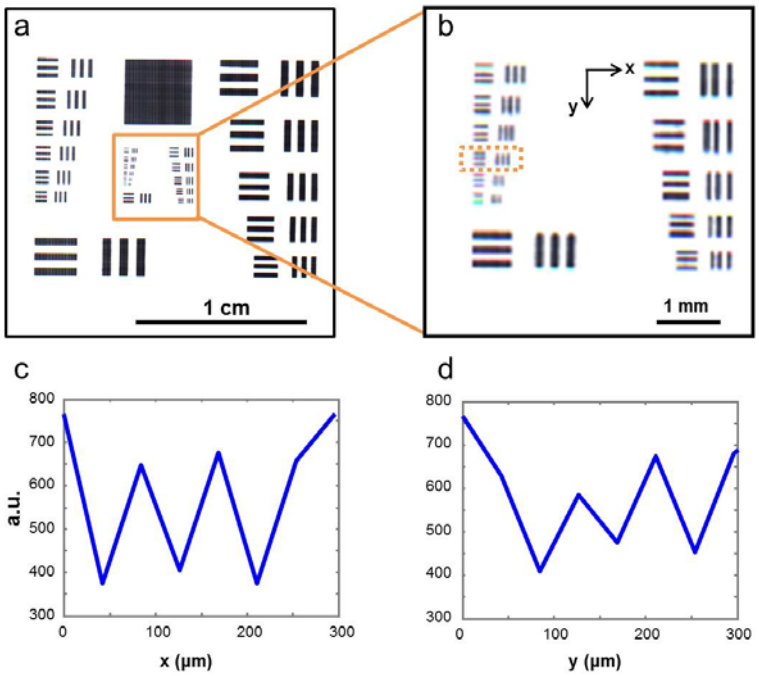

Figure 4.2. Resolution test. (a) The image of a resolution target obtained by the AnCam. (b) A zoomed-in region of (a), showing that the 11.3 lp/mm (88.5-μm line spacing) element is discernible (labeled in the orange rectangle). (c-d) The intensity profile of the 11.3-lp/mm element in the x (c) and y (d) directions after summing the red, green, and blue (RGB) channels.

In order to further verify that the optical resolution of the SLA is much higher than the pixel-limited resolution of the system, we used a 1951 USAF target as the sample, and aligned it to the front focal plane of the SLA. The image generated by the SLA was collected by a standard microscope with a 10× 0.3 NA objective and captured by a 4.65 μm pixel-size CCD camera (DMK 31BU03, The Imaging Source). The microscope provides a sub-micron resolution, which ensures that we are observing the resolution of the SLA. The

imaging setup is illustrated in Figure 4.3a, and the image is shown in Figure 4.3b. The image Group 7, Element 1 (128 lp/mm, or 7.8 μm line spacing) is discernible, suggesting a resolution of 8 μm.

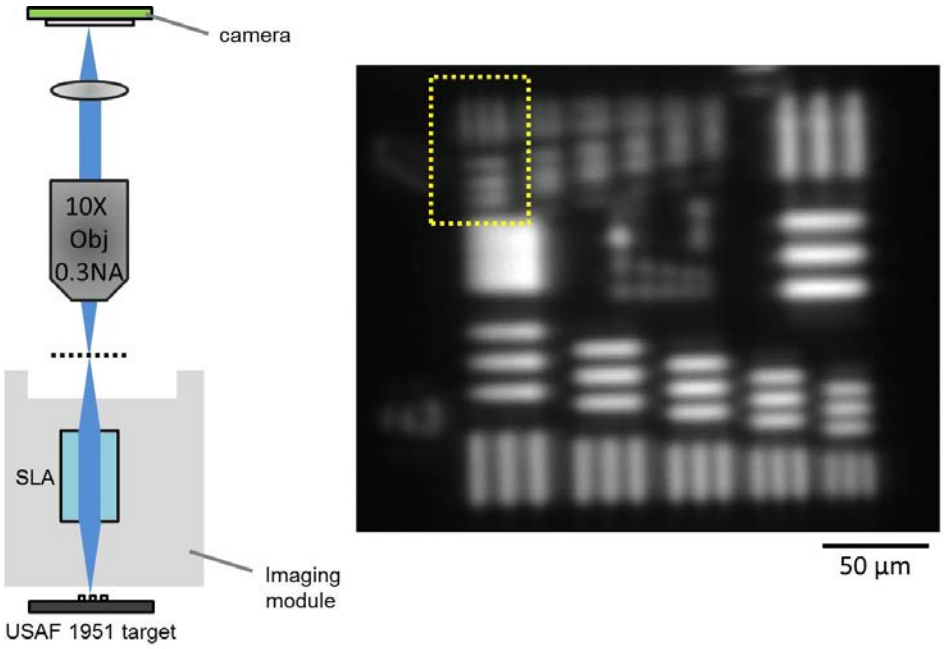

Figure 4.3. Optical resolution measurement of SELFOC lens array. Left: measurement system setup. Right: measurement result. Group 7, Element 1 (128 lp/mm, or 7.8 μm line spacing) is discernible (yellow rectangle).

4.4 Depth of field

We characterized the DOF of the AnCam to demonstrate its tolerance of tissue unevenness. The DOF measurement is illustrated in Figure 4.4, which is adapted from the standard DOF measurement method for optical imaging systems. The imaging module was raised by 0.7 mm to make sure that the focal plane of the SLA is above the tube surface. Then a resolution target with a 5.9-lp/mm (170-μm line spacing) line pattern was attached to the tube surface with a tilting angle of $\theta=1/15$ rad (Figure 4.4a). The light source of the imaging module was disabled and an external light source was used to provide a uniform illumination onto the target. After obtaining the scanned image (Figure 4.4c), the modulation transfer function (MTF) at different separation distances was defined as the normalized contrast of the line pattern, and the result was plotted (Figure 4.4b). The DOF

was then defined as the depth range where the MTF was above 50%, which was calculated to be 0.65 mm at 5.9 lp/mm. Figure 4.4d–h shows representative images of the line pattern at different distances below (Figure 4.4d,e), at (Figure 4.4f), and above (Figure 4.4g,h) the focal plane. Their positions are also marked in Figure 4.4b.

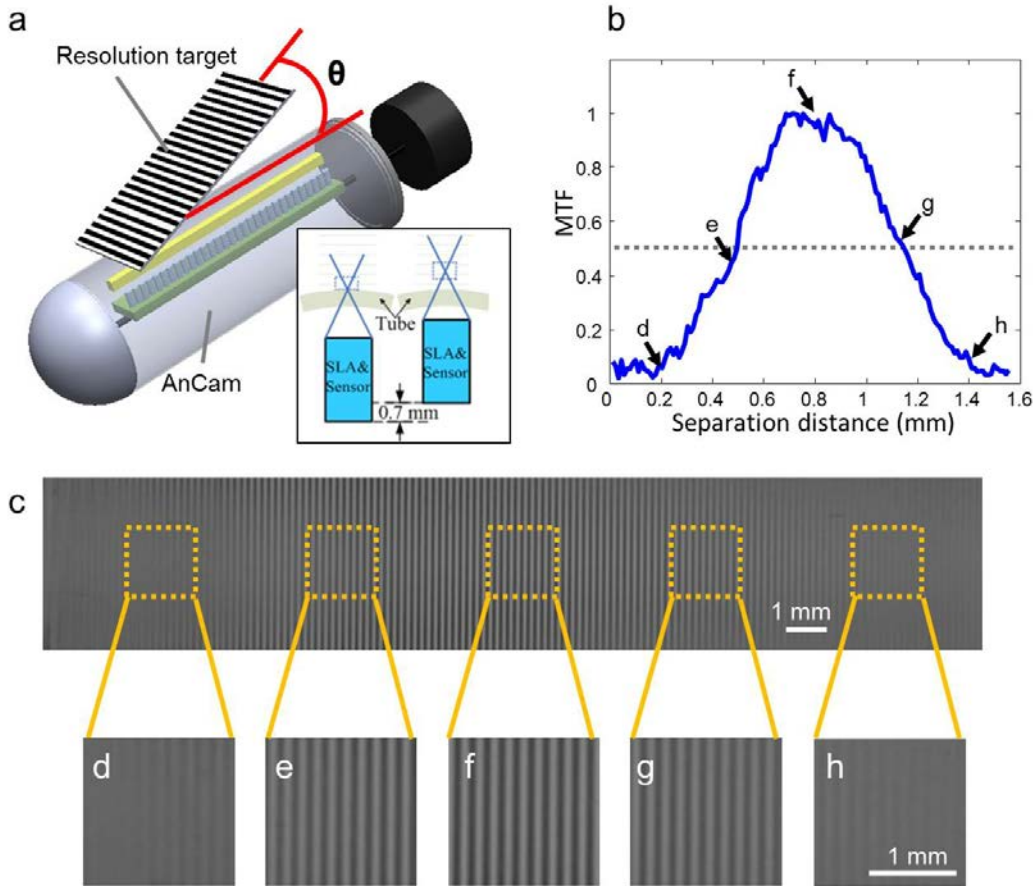

Figure. 4.4. The depth-of-field (DOF) measurement. (a) The setup for the DOF measurement. A resolution target with a 5.9-lp/mm line pattern was attached on the tube surface of the AnCam at an angle of θ=1/15 rad. The imaging module was raised by 0.7 mm to make sure the focal plane of the SLA is above the tube surface (bottom-right image). (b) The measured modulation transfer function (MTF) corresponding to the separation distance of the line pattern. (c-h) The scanned image of the target and the zoom-in images of the line pattern with a distance of 0.2 mm (d), 0.5 mm (e), 0.8 mm (f), 1.1 mm (g), and 1.4 mm (d) to the tube surface.

4.5 Entire anal canal imaging using the AnCam in comparison to a colposcope

Next, we compared the performance of the AnCam with that of a conventional colposcope in the imaging of the anal canal. These studies were completed in an *in vivo* pig model. After the pig was anesthetized as per approved institutional protocols, a small region of the anal canal was stained using a marker pen. The AnCam was gently inserted into the anal canal after applying a small amount of water-based lubrication to the top of the device (Figure 4.5a). The entire cylindrical surface of the anal canal was imaged with a single scan (Figure 4.5b). Results of the comparison are shown in Figure 4.5c–e. The image has a FOV of 55 mm × 120 mm (Figure 4.5c). The stained patterns made from the marker pen are discernible (Figure 4.5d,e). As a comparison, the same area of the anal canal was examined using a plastic anoscope and a standard colposcope (Olympus OCS-3) with 12× magnification (Figure 4.5f,g), and the image was captured using an iPhone 4S camera connected to the eyepiece via a customized adaptor. The yellow and blue arrows in Figure 4.5e and 4.5g are pointing at the same stained spots viewed under the two systems, as marked by the pen. Both the AnCam and the colposcope can resolve these stained spots. It is also worth noting that the colposcope images (Figure 4.5f,g) have unavoidable reflections on the tissue surface due to the illumination of the light source affecting visualization of the anal mucosa.

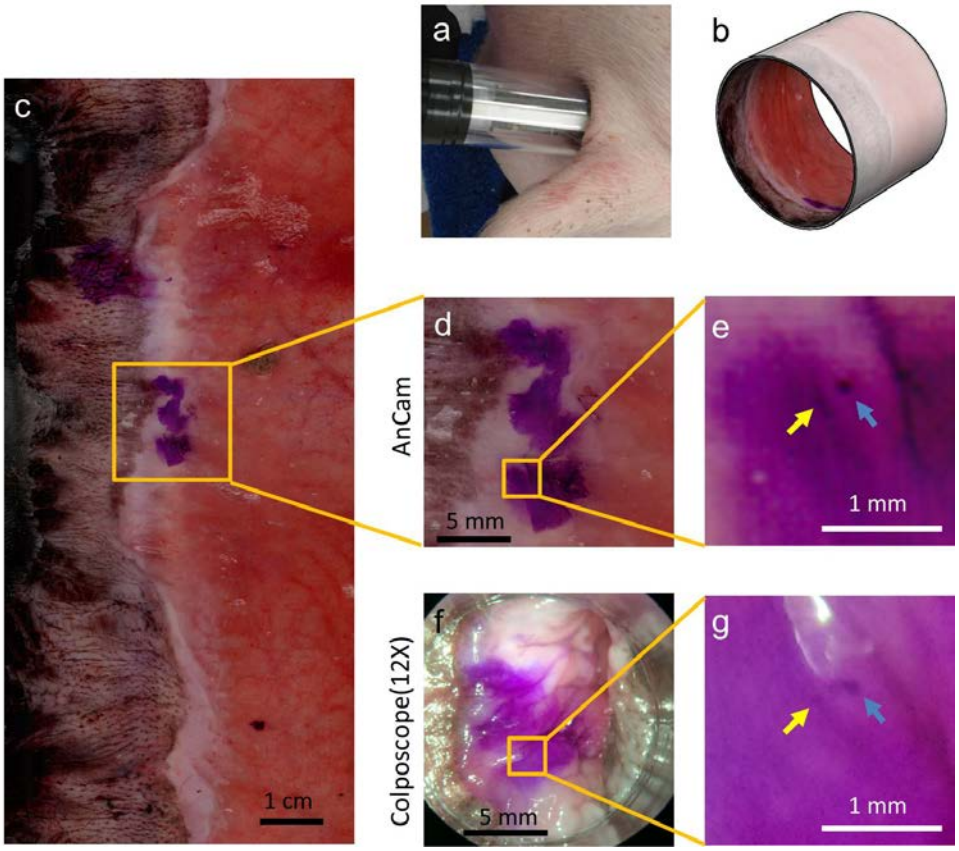

Figure 4.5. Whole anal canal imaging of an animal model. (a) The AnCam was inserted into the anus of a live pig for imaging. (b) The cylindrical surface containing the whole anal canal was imaged with a single scan. (c–e) The wide field-of-view (FOV) image captured by the AnCam (c) with the stained region zoomed in (d,e). (f–g) The same stained region captured by a standard colposcope with 12× magnification (f) with a zoomed-in and 90°-rotated image (g). The yellow and blue arrows in (e) and (g) are pointing at the same stained spots.

4.6 Time-lapse imaging of acetowhite test

Delineation of acetowhite tissues is a critical step in standard HRA and requires application of acetic acid to dehydrate anal mucosa cells. Acetic acid-induced changes of the epithelial surface localize abnormal areas that require biopsy [6,10]. To demonstrate that the AnCam is capable of depicting the dynamic changes in the anal mucosa with serial acetic acid application and of localizing acetowhite areas, we performed acetic acid testing in a live, anesthetized pig. First, we documented the appearance of the anal canal before acetic acid

staining (Figure 4.6a,b). Then, a 5% acetic acid-soaked gauze was inserted into the anal canal for 5 min. The gauze was removed, and an AnCam image was obtained (Figure 4.6c). We repeated the application of acetic acid three times, removed the gauze, reinserted the AnCam, and obtained serial time-lapse images of the anal canal (Figure 4.6c–e). We compared the entire anal canal before application of acetic acid with the post-acetic acid images, and an area of interest before and after the three rounds of acetic acid staining is shown in Figure 4.6b–e. There was a significant whitening of the anal canal epithelium (yellow arrows) and rectal epithelium (white arrow) after each of the first two stainings (Figure 4.6b–d). However, there was no further change after the third staining (Figure 4.6e), arguing that there is no further improvement in acetowhite effect after 10 min of acetic acid application. In each of the images (Figure 4.6b–e), the anatomic structure of interest was reproduced and comparable. The consistency of the images argues for the potential use of this device in longitudinal follow-up of patients with anal canal pathology.

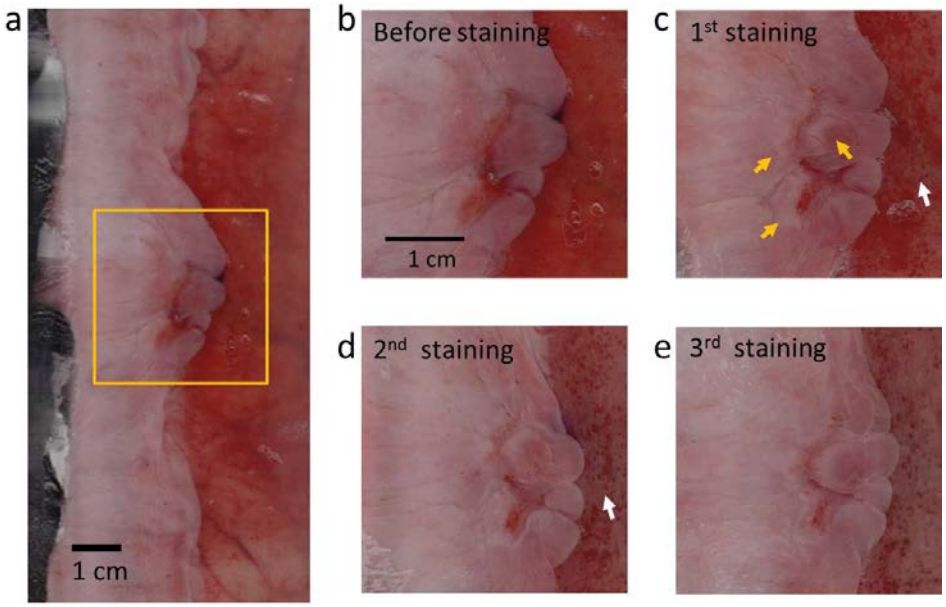

Figure 4.6. The time-lapse images of three rounds of acetic acid staining. (a–b) The wide field-of-view (FOV) AnCam image of the anal canal (a) and a zoomed-in region (b) before staining. (c) After the first round of staining, there was a significant whitening of the anal canal epithelium (yellow arrows) and rectum epithelium (white arrow). (d) After the

second round of staining, more regions of the anal canal and rectum became whitened. (e) After the third round of staining, the tissue did not become further whitened.

The acetic acid induced changes gradually fade out with return of the epithelium to normal. We monitored this washout process by evaluating serial AnCam images. The scans were repeated at 6-min intervals for 60 min. The results are shown in Figure 4.7. The selected whitened areas (arrow) gradually faded out over time and disappeared at 36 min. By 66 min, all the stained regions had returned to normal. To our knowledge, this is the first time the acetic acid staining and washout process has been dynamically monitored and reported. This may provide guidance to physicians for optimizing and standardizing the dose and duration of acetic acid application in HRA.

.

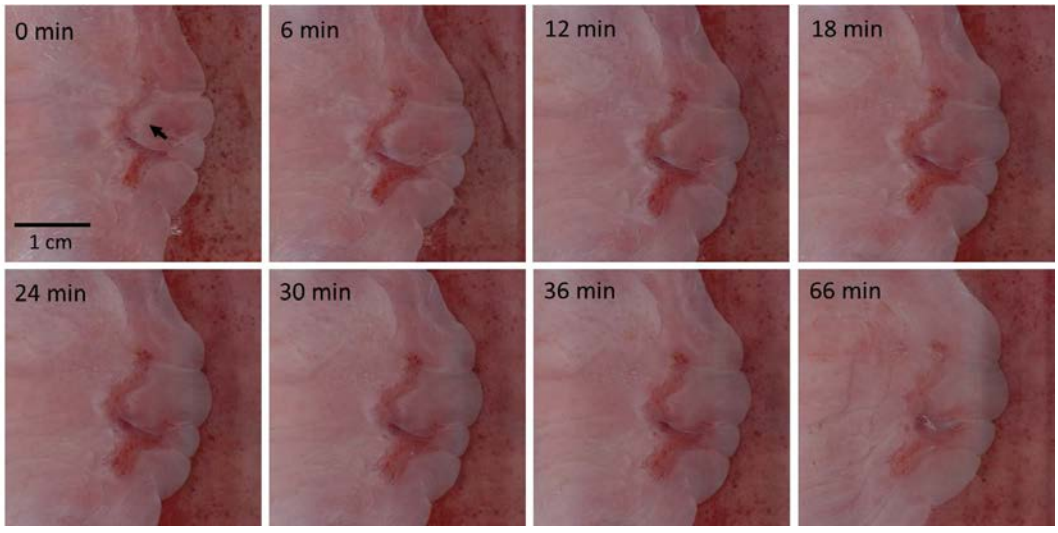

Figure 4.7. The time-lapse images showing the wash-out process of the acetowhite areas. It can be observed that the selected whitened areas (arrow) gradually faded out over time and disappeared at 36 min, and all the stained regions returned to normal at 66 min.

4.7 AnCam built for clinical examination of patients

In previous sections, we have already demonstrated the performance of the AnCam in terms of resolution, DOF, and time-lapse imaging capability. However, all the parts of the AnCam are fixed and the tube has to be cleaned using 70% ethanol after each use. For experiment on patients, further modification needs to be made. First, materials need to be

biocompatible, thus the 3D printed PLA tube tip is no longer suitable. Second, the whole tube has to be made disposable to avoid cross-contamination among different patients. Towards this direction, we developed our new AnCam, hereby termed the medical AnCam.

4.7.1 Design

The design of the medical AnCam is shown in Figure 4.8. Compared with the old version AnCam, it has two easily separable components: the main body and the disposable tube. The main body has a motor compartment to prevent the motor and the cables from being exposing to the patient. The motor compartment also has a cable outlet connected with medical tubing, which packages all the cables inside for the patient's safety. The quick connection between the main body and the tube are facilitated by designing two connectors (Connector A and B). They have fitting surfaces to ensure the positioning (green arrows in Figure 4.8). Besides, they also have male (Connector A) and female (Connector B) locking structures (red arrows) so that they can lock into each other by a simple rotation.

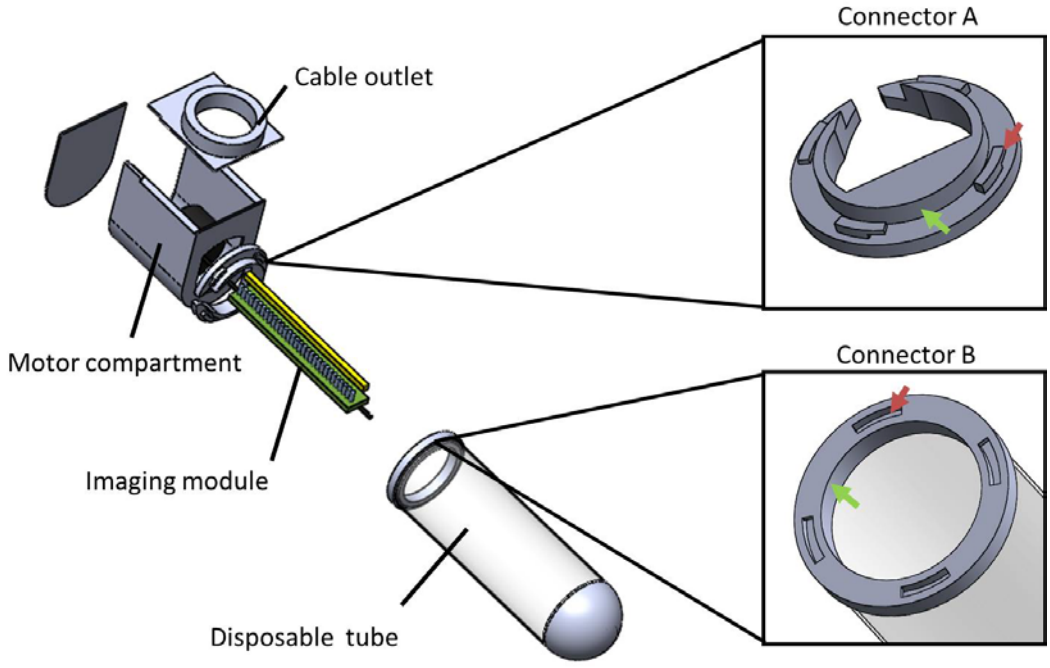

Figure 4.8. The design of the medical AnCam. The main body consists of the motor compartment and the imaging module. The disposable tube can be easily mounted onto the

main body by designing two connectors (connector A and B) on the main body and the tube, respectively.

Before the experiment, the disposable tube can be mounted to the main body by first aligning the two fitting surfaces on Connector A and B, then rotating the tube clockwise to make Connector A and B lock to each other, as shown in Figure 4.9. After each experiment, the tube can be removed from the main body by simply rotating it counterclockwise and pulling it out, which is just a reverse process. In this way, the disposable tubes can be easily changed for examining different patients.

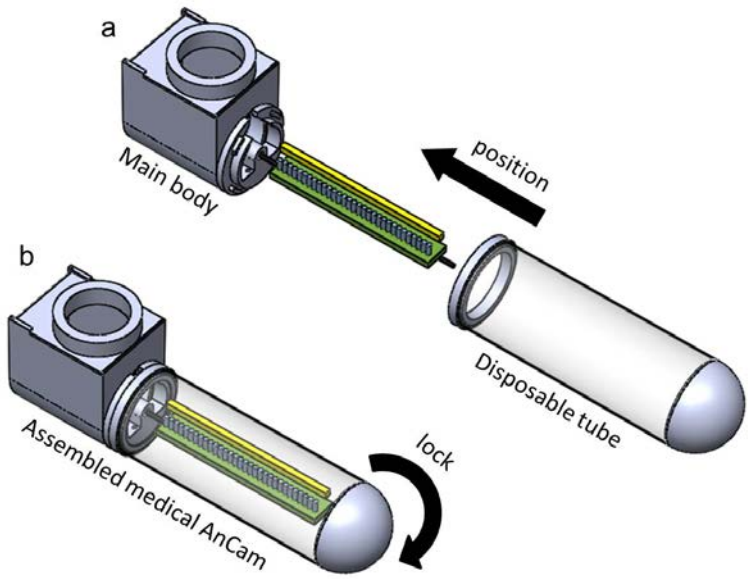

Figure 4.9. The tube mounting process for the medical AnCam. (a) The disposable tube is positioned to the main body by aligning two fitting surfaces (connector A and connector B, as shown in Figure 4.8). (b) The disposable tube is locked to the main body by simply rotating the tube clockwise. Reversing this process will unmount the tube.

4.7.2 Fabrication of the disposable tube

The disposable tube consists of a medical-grade silicone tip, a polycarbonate tube, and Connector B. The fabrication process includes several steps. First, the medical-grade silicone tip is fabricated by a molding process. Second, the disposable tube is packaged by attaching the tip and Connector B to the PC tube and coating an extra layer of silicone at

the junctions between the tip and the polycarbonate tube to ensure that the material in contact with the patients is biocompatible. The plastic materials are glued together by chloroform. The whole process will be described in detail as follows.

The silicone tip is fabricated with the following procedures as shown in Figure 4.10. First, a Poly(methyl methacrylate) (PMMA) core is assembled by gluing five pieces of PMMA disks (Diameter=14 mm, 20 mm, 26 mm, 20 mm, and 30 mm) (Figure 4.10a). This design forms a groove at the core's surface to keep the silicone from falling off. Then a hemisphere mold is prepared by cutting the tip out of a polypropylene (PP) centrifuge tube (Z640948, Sigma-Aldrich) (Figure 4.10b). Next, the PMMA core and the hemisphere mold are assembled together for the molding process (Figure 4.10c). The medical-grade silicone pre-polymer (Silastic 7-4870, Dow Corning) is prepared by mixing its two components, and filled between the PMMA core and the hemisphere mold (Figure 4.10d). The mold is then placed inside an oven at 150 ^{0}C overnight (Figure 4.10e), and the cured silicone tip can finally be released from the mold (Figure 4.10f).

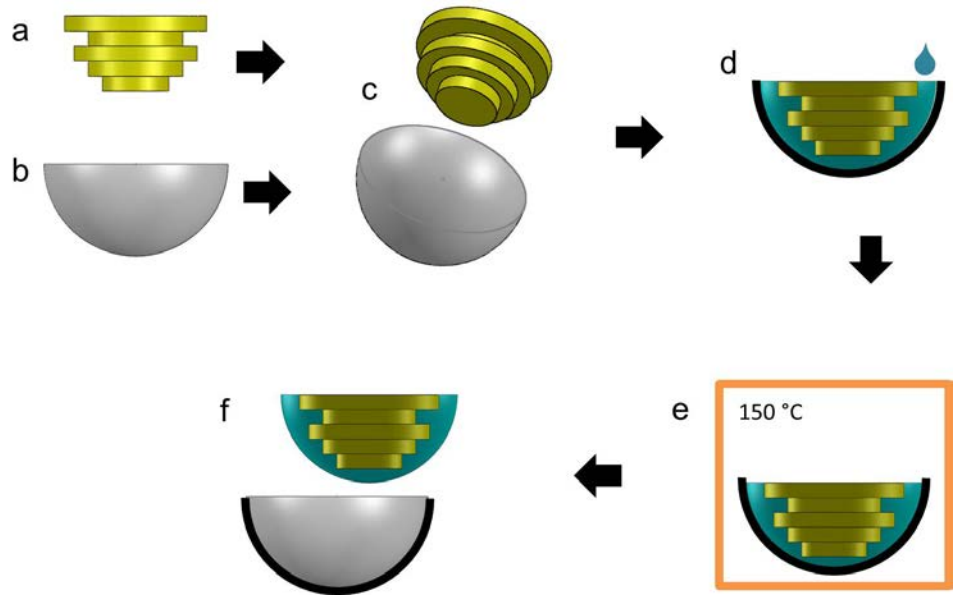

Figure 4.10. The fabrication process of the silicone tip. (a) A Poly(methyl methacrylate) (PMMA) core is assembled by gluing five pieces of PMMA disks. (b) A hemisphere mold is prepared by cutting the tip out of a polypropylene (PP) centrifuge tube. (c) The PMMA core and the hemisphere mold are assembled together for the molding process. (d) The

medical-grade silicone pre-polymer is prepared and filled between the PMMA core and the hemisphere mold. (e) The mold is placed inside an oven at 150 ^{0}C overnight. (f) The cured silicone tip is released.

After obtaining the silicone tip, the disposable tube can be fabricated with the following procedures, as shown in Figure 4.11. First, an adaptor is made by the 3D printer and attached to the silicone tip (Figure 4.11a). Then the PC tube is attached to the silicone tip via the adaptor (Figure 4.11b). Next, an extra layer of medical-grade silicone is coated around the junction between the silicone tip and the PC tube (Figure 4.11c) by following a customized coating protocol, which will be described in the next paragraph. Finally, Connector B is fixed to the other end of the PC tube (Figure 4.11d).

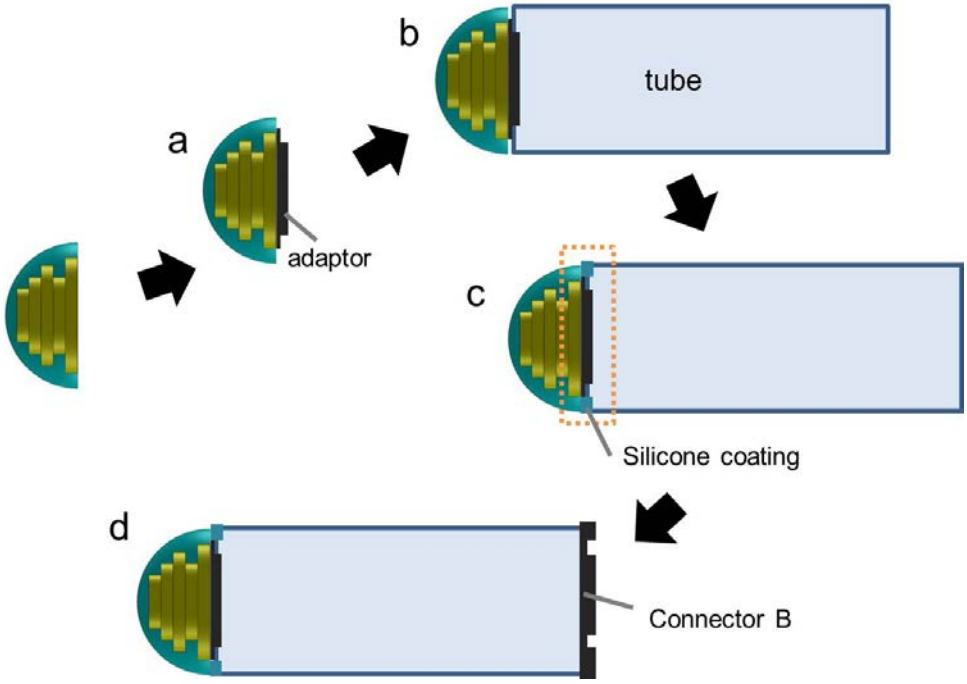

Figure 4.11. The fabrication process of the disposable tube. (a) An adaptor is attached to the silicon tip. (b) The polycarbonate tube is attached to the silicone tip via the adaptor. (c) An extra layer of medical-grade silicone is coated around the junction between the silicone tip and the PC tube (orange rectangle). (d) Connector B is fixed to the other end of the PC tube.

As previously mentioned, in order to ensure that the material in contact with the patients is biocompatible, an extra layer of silicone is coated at the junctions between the tip and the PC tube. However this process cannot be done by directly placing the assembled disposable tube in the oven, since the adaptor and Connector B are made of PLA material and cannot withstand the temperature for silicone curing. Therefore, we developed a localized heating method, as shown in Figure 4.12. First, we coated the junction with silicone pre-polymer. Then we mount the disposable tube onto a rotational stage, and a hot air gun (Aoyue 850A++) is aligned to blow the 150 ^{0}C hot air at the pre-polymer. To provide uniform heating, a stepper motor is used to control the tube to rotate in the fashion shown in Figure 4.12a: the tube rotates at a slow speed of 0.2 rad/sec within a small region (π/9 rad angle range) back and forth for 5 min (Figure 4.12a1), then moves to the next region (Figure 4.12a2). This process repeats until all the 360^0 is heated. The disposable tube before and after silicone coating is shown in Figure 4.12b and 4.12c.

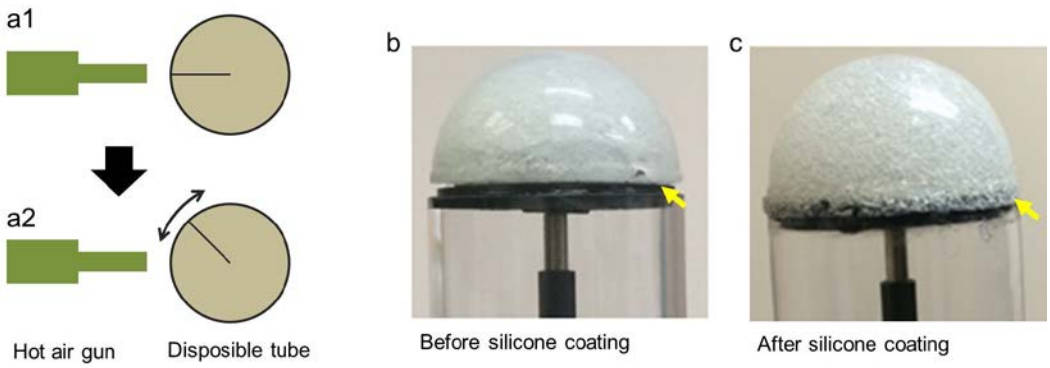

Figure 4.12 The silicone coating process. (a1─a2) The disposable tube is coated with silicone pre-polymer, and a hot air gun is used to cure the pre-polymer by the rotational movement of the disposable tube. (b─c) The disposable tube before (b) and after (c) coating the silicone layer.

4.7.3 The assembled medical AnCam prototype

The medical AnCam prototype with the disposable tube assembled to the main body is shown in Figure 4.13. A medical tubing is also connected to the motor compartment to package the cables inside, so that all the parts in contact with the patient are biocompatible and non-hazadous.

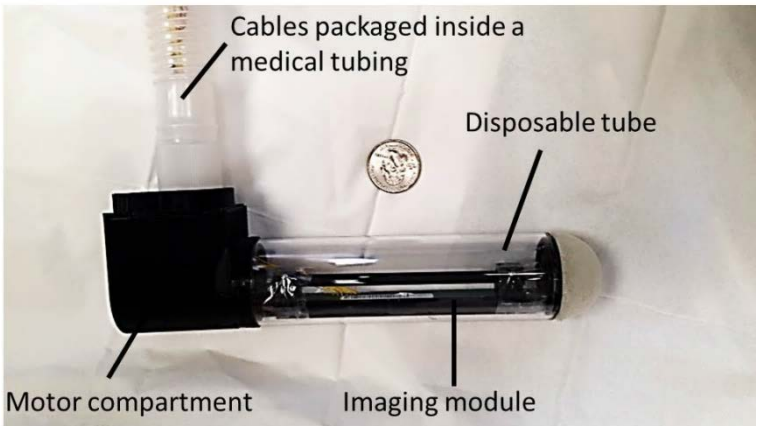

Figure 4.13. The assembled medical AnCam prototype.

4.7.4 Clinical experiment with a patient

We have applied our medical AnCam prototype to the whole anal canal screening of a patient. Figure 4.14 shows the AnCam images of the whole anal canal before (Figure 4.14a) and after (Figure 4.14c) acetic acid staining. By zooming in the same region in these two images, we can observe that the tissue was successfully whitened, providing a better contrast for further diagnosis. This also demonstrates the consistency of AnCam images.

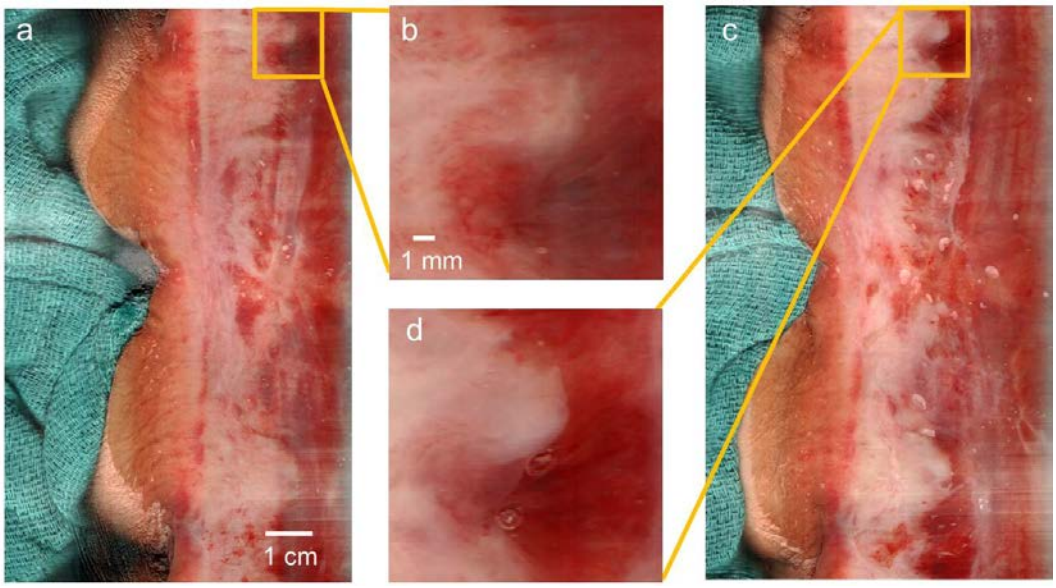

Figure 4.14. AnCam imaging of a patient before and after acetic acid staining. (a) The whole anal canal image before acetic acid staining. (b) A zoomed-in image of (a). (c) The whole anal canal image after acetic acid staining. (d) A zoomed-in image of (c).

We also compared the performance of the medical AnCam with that of a conventional colposcope (LEISEGANG OptiK Model 2 colposcope with the Canon 600D T3i DSLR camera) in the anal canal imaging of the patient, as shown in Figure 4.15. After acetic acid staining, the medical AnCam and the colposcope were used separately to get the anal canal images of the patient (Figure 4.15a,c). Zoom-in images show that the same stained structures can be discovered by both systems, as pointed by the yellow and blue arrows in Figure 4.15b, 4.15c.

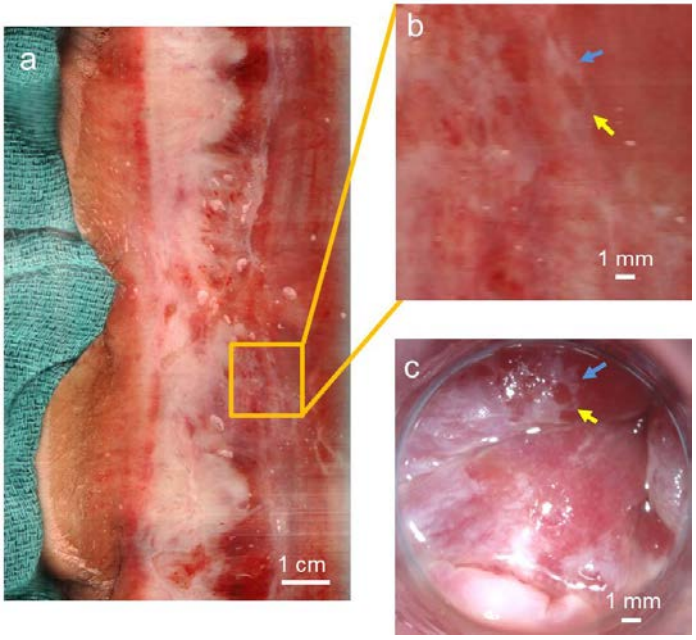

Figure 4.15. Comparison between the medical AnCam and a colposcope in the anal canal imaging of a patient. (a) The medical AnCam image of the whole anal canal. (b) A zoomed-in image of (a). (c) The colposcope image of the anal canal at the same region as (b). The arrows of the same color in (b) and (c) are pointing at the same stained structures.

4.8 Discussion

As a proof of concept, we used an image sensor with 600 dpi (equivalent to a pixel pitch of 42.3 μm) disassembled from a business card scanner, resulting in an imaging resolution of 89 μm. Conventionally, colposcope images are read out either directly from the eyepiece or captured by a CCD video camera, and the resolution of a colposcope is limited by the number of pixels in the camera (the optical resolution is usually much higher). Our current

89-μm resolution is comparable to that of mainstream colposcopes with video cameras using the National Television System Committee (NTSC) standard. For example, these cameras equipped in an Olympus OCS-3 can provide a resolution between 350 μm and 50 μm for magnifications between 3× and 17×, respectively.

Recently, up-to-date colposcopes have been shown to be able to provide improved resolution by connecting the scope to a high definition video camera or a digital single-lens reflex (DSLR) camera. For example, we have measured the resolution of the LEISEGANG OptiK Model 2 colposcope with the Canon 600D T3i DSLR camera. A USAF 1951 target was imaged by this system with its maximum 15× magnification, and the Group 5 Element 6 is clearly discernible, giving a resolution of 18 μm (Figure 4.16). In comparison, the resolution of the AnCam can also be further improved by choosing image sensors with higher pixel densities. As an example, flatbed film scanners such as CanoScan LiDE 700F have 4800 dpi (equivalent to a pixel pitch of 5.2 μm) image sensors, which potentially can improve our current resolution by 8 times. However, it is worth noting that higher resolution will also result in a significantly longer scan time. For instance, consider that we use a 4800 dpi image sensor instead of a 600 dpi one in order to get an 8× resolution improvement. We would need to reduce the frame rate to ~1/8, and also increase total scan steps by 8 times. This will result in a >10 min total scan time compared with the 10 sec for the current AnCam. On this time scale, the resolution and image quality can be deteriorated by any movement or contraction of the live tissue. Therefore, this trade-off between resolution and scan time needs to be considered when selecting the image sensors for specific needs. Actually, we envision that AnCam is aiming to further assist HRA diagnosis instead of being a competitor with current colposcopes, since the best way should be rather to combine these two methods: AnCam can act as a fast screen at the first stage to get all the information inside the anal canal, providing a map to the locations of all suspicious regions, and then the colposcope can be used to image only these regions for later biopsy examination or surgery. In this way, the total inspection time can be significantly shortened.

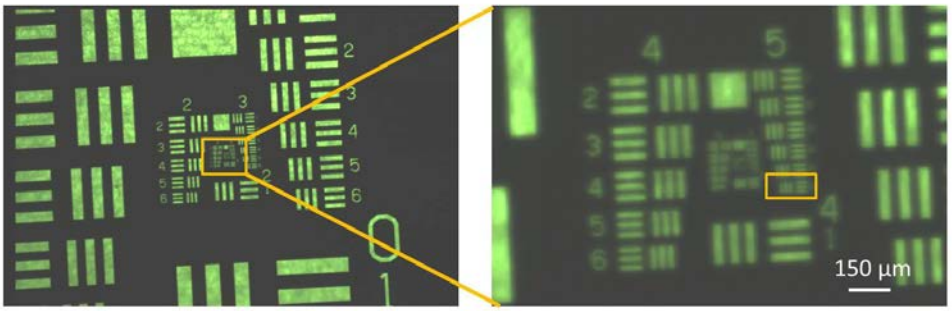

Figure 4.16. The optical resolution measurement of a typical colposcope (LEISEGANG OptiK Model 2) with a DSLR camera (Canon 600D T3i). (a) The image under 15× magnification captured by the DSLR camera. (b) The zoomed-image showing that the smallest discernible pattern is Group 5 Element 6 (57 lp/mm, or 18 µm line spacing).

The cost of our AnCam prototype is less than $150 (not including the computer), which is two orders of magnitude lower than a typical colposcope. The whole AnCam inspection simply includes the insertion of the probe and a quick 10-sec scan, with no refocusing or any extra steps needed, thus making it very easy to operate. This simplification of the anal canal examination process is highly desirable. In addition, the AnCam can be quite attractive for telemedicine applications whereby diagnoses can be made in low-resource settings where colposcopes are not affordable or specially trained personnel are not available. Under this circumstance, the AnCam can generate an objectively obtained and digitally stored image containing all of the information from the entire anal canal. This image can then be remotely transferred to specialized centers where experienced professionals can interpret it for the screening of potential anal dysplasia.

It is worth noting that the morphologies of the stained tissue in the pig experiment do not appear completely similar in the AnCam images compared with the HRA images, as shown in Figure 4d and 4f. This is because the tube of the AnCam stretches the pliable mucosa on the transparent polycarbonate tube so that the entire anal canal surface is tightly attached to the tube surface. In comparison, in HRA, the clear plastic anoscope allows the colposcope to visualize the collapsed anal mucosa through its open end. The tissue observed by the colposcope can have folded regions due to the pliable nature of the anal mucosa, thus making it difficult to inspect by HRA. On the other hand, the AnCam potentially has the

advantage of observing the details hidden in these folded regions. For this purpose, the tube diameter should be carefully chosen: a too-small diameter may not be sufficient to fully stretch the folded tissues, while a too-large diameter may cause pain or injury to patients. This can be easily addressed by designing AnCams with different tube diameters, so that a personalized tube size can be determined after evaluating the anal dimension for each particular patient. The tube part can also be made disposable to avoid cross-contamination among patients. For our current AnCam prototype, we used a polycarbonate tube fabricated by a plastic extrusion process. This process generates minor line patterns on the tube surface that sometimes can be observed in AnCam images (Fig. 4e). This can be further improved by choosing other plastic tubes made by the injection molding process, which can provide better surface quality.

In this chapter, we also demonstrated the consistency of AnCam images by tracking the dynamics of the acetowhitening process. This revealed the potential of AnCam in longitudinal follow-up of patients with potential anal canal dysplasia or who are under anal cancer treatment. Similar to the use of annual mammograms to identify new breast cancers, serial digital images of the entire anal canal can be compared when a follow-up is performed for any abnormal changes, so that any dysplasia inside the anal canal can be detected at a very early stage. Due to its simplicity and minimally invasive nature compared with HRA, the AnCam can also be suitable for regular preventive screenings among populations of patients with sexually transmitted diseases or male homosexual contact for the early diagnosis of HPV infection or anal cancer.

4.9 Conclusion

High resolution anoscopy is the gold standard for the screening of anal dysplasia. Conventional HRA is based on the use of a colposcope. The imaging geometry of the colposcope is ill-matched to the geometry of the anal canal. This results in an imaging procedure that is labor-intensive, time-consuming, and operator-dependent. To address these shortcomings, we designed and built a novel scanning endoscopic system, the AnCam, using CIS technology. The AnCam utilizes low cost and disposable parts, has a resolution of 89 μm, a DOF of 0.65 mm at 5.9 lp/mm, and a maximum FOV of 100 mm × 120 mm. The AnCam can complete a full scan of the anal canal within 10 seconds, a fraction of the time required for a conventional HRA examination (typically more than 30

min), and the images are standardized and reproducible. Lastly, the use of the device does not require specialized training. The overall imaging performance, the reproducibility of the images, and the ease-of-use render the AnCam a highly attractive potential alternative to current imaging modalities of the anal canal and other cylindrically shaped anatomic sites, such as the esophagus.

REFERENCES

1. L. G. Johnson, M. M. Madeleine, L. M. Newcomer, S. M. Schwartz, and J. R. Daling, "Anal cancer incidence and survival: The surveillance, epidemiology, and end results experience, 1973–2000," Cancer **101**, 281–288 (2004).
2. R. A. Nelson, A. M. Levine, L. Bernstein, D. D. Smith, and L. L. Lai, "Changing Patterns of Anal Canal Carcinoma in the United States," J. Clin. Oncol. **31**, 1569–1575 (2013).
3. M. Frisch, B. Glimelius, A. J. C. vandenBrule, J. Wohlfahrt, C. J. L. M. Meijer, J. M. M. Walboomers, S. Goldman, C. Svensson, H. O. Adami, and M. Melbye, "Sexually transmitted infection as a cause of anal cancer," New Engl. J. Med. **337**, 1350–1358 (1997).
4. C. E. Pineda, J. M. Berry, N. Jay, J. M. Palefsky, and M. L. Welton, "High resolution anoscopy in the planned staged treatment of anal squamous intraepithelial lesions in HIV-negative patients," J. Gastrointest. Surg. **11**, 1410–1415 (2007).
5. I. T. D. E. Silva, L. C. D. Ferreira, F. S. Gimenez, R. A. G. Guimaraes, L. B. Fujimoto, C. R. B. Cabral, R. V. Mozzer, and L. D. S. Atala, "High-resolution anoscopy in the diagnosis of anal cancer precursor lesions in renal graft recipients," Ann. Surg. Oncol. **15**, 1470–1475 (2008).
6. N. Jay, J. M. Berry, C. J. Hogeboom, E. A. Holly, T. M. Darragh, and J. M. Palefsky, "Colposcopic appearance of anal squamous intraepithelial lesions - Relationship to histopathology," Dis. Colon Rectum **40**, 919–928 (1997).
7. T. J. Wilkin, S. Palmer, K. F. Brudney, M. A. Chiasson, and T. C. Wright, "Anal intraepithelial neoplasia in heterosexual and homosexual HIV-positive men with access to antiretroviral therapy," J. Infect. Dis. **190**, 1685–1691 (2004).
8. G. A. Zheng, X. Z. Ou, and C. H. Yang, "0.5 gigapixel microscopy using a flatbed scanner," Biomed. Opt. Express **5**, 1–8 (2014).
9. Z. Göröcs, Y. Y. Ling, M. D. Yu, D. Karahalios, K. Mogharabi, K. Lu, Q. S. Wei, and A. Ozcan, "Giga-pixel fluorescent imaging over an ultra-large field-of-view using a flatbed scanner," Lab Chip **13**, 4460–4466 (2013).
10. B. Kumar and S. Gupta, "The acetowhite test in genital human papillomavirus infection in men: what does it add?," J. Eur. Acad. Dermatol. **15**, 27–29 (2001).

Chapter 5

A SMARTPHONE-BASED PANORAMIC ENDOSCOPE FOR HIGH-THROUGHPUT SCREENING

In the previous chapter, we presented the AnCam, a wide field-of-view (FOV) scanning endoscope. It significantly reduces the time and labor for anal canal screening. In this chapter, we aim to further enhance the speed of imaging by developing a new panoramic endoscope, named the PanCam. The PanCam consists of a panoramic annular lens (PAL), which is able to collect the 360° view of its surroundings, allowing the PanCam to perform the wide FOV imaging with a single shot. Additionally, the PanCam uses a camera module from a smartphone, so that the endoscopic image can be captured using the smartphone itself. In addition, we developed a novel illumination method to ensure that all the tissues within the PanCam's FOV are uniformly illuminated. The PanCam is compact, low-cost, and is potentially capable of video-rate imaging. We believe the PanCam can potentially be a simple endoscopic solution for fast-speed screening.

5.1 Background

Towards the wide FOV screening of the whole anal canal, we have developed the AnCam prototype, as presented in Chapter 4. The imaging speed of the AnCam is determined by its mechanical scanning speed, which is essentially limited by the linear image sensor's frame rate. In order to further increase the imaging speed and finally achieve video-rate imaging capability for a wide FOV endoscope, mechanical scanning is not a preferable solution and a new imaging mechanism is needed.

In recent years, new efforts have been made for building medical endoscopes with 360° side-view (panorama) capability. Ou-Yang and Jeng designed a radial imaging capsule endoscope by placing an inverted cone mirror in front of a lens, so that all the tissues surrounding the endoscope can be projected to the lens's image plane by the reflection of the cone mirror [1]. Wang *et al.* developed an endoscope that is able to capture simultaneous forward and side views, where the side view is also provided by convex mirror reflection [2]. However, these two works only focused on the lens design to improve optical performance, and did not discuss a feasible solution for the illumination. Sagawa *et*

al. built an attachment to a conventional endoscope (Olympus CF-240AI) to obtain the front and side view in a similar style [3]. They further investigated the illumination performance by using the endoscope's own light source. However, this endoscope could not provide very uniform illumination throughout its FOV, and the mirror was fixed by a holder in front of the camera, which blocked part of the FOV. Finally, these previous works either did not establish the resolution [1,3], or only have a limited resolution of ~1 mm for the side-view [2].

In addition to the combination of a cone/convex mirror and a lens, the panoramic annular lens (PAL) is another optical device for panorama imaging. The first PAL was designed by Greguss [4]. Since then it has been widely used in wide FOV scene capture [5], computer vision [6], pipe inspection endoscopes [7,8], and panoramic stereo imaging [9]. PAL is a monolithic catadioptric lens consisting of two refractive and two reflective surfaces, which is able to project its 360° surrounding scene into a 2D annular-shaped image. PAL has several intrinsic advantages for panoramic imaging. First, it is a single-element block, therefore it is compact in size and no alignment is needed between its refractive and reflective surfaces, making it easy to implement and robust in complicated environments. In addition, PAL has a single center of projection, so that the panoramic image can be reconstructed without distortion.

The advantages of PAL make it a very promising solution for building a panoramic medical endoscope. However, to our knowledge, no PAL-based medical endoscope has been built yet, to a large extent due to the illumination issue. For capturing panorama of an outdoor scene, the objects are already illuminated by ambient light; however, for endoscope uses, the samples are dark and need to be illuminated by a light source. This light source is required to provide uniform illumination throughout the entire panorama FOV, and thus it is not easy to design. Matthys *et al.* used two opposing collinear PALs in their system [10], one as an illuminator where the light path was inverted to project a light beam to the sample around the PAL, while the other one was for imaging the illuminated sample. This method can obtain a uniform illumination, however an additional PAL has to be used, so the system size is not as compact as a single PAL. Opto Engineering has a commercial boroscopic probe using PAL for panoramic cavity imaging (PCBP series, Opto Engineering). They designed an LED ring around the probe near the PAL as the light source. However, this

method requires the sample to be at a certain distance away from the probe, and the illumination will be blocked when the sample is in contact with the probe, such as in anal canal or rectum imaging. Therefore, a convenient and uniform illumination solution for the PAL-based medical endoscope is yet to be found. Another limitation preventing PAL's wide application is its cost: it has a complicated geometry with four optical surfaces, so it used to be expensive to fabricate [11].

Recently, smartphones have found increasing applications in healthcare industry [12]. Up-to-date smartphones keep demonstrating high computational performance, convenient mobile network connection, compact size, and camera sensor capability. In particular, the pixel count of mobile phone cameras has been increasing exponentially following Moore's law over the past decade [13], and the maximum pixel count is now above 40 mega-pixels (Nokia Lumia 1020). In addition, during the fast proliferation of smartphones among the global population, numerous smartphone camera accessories have been developed, and panoramic lenses have gained increasing popularity for immersive video capture. In particular, Kogeto has released a PAL for panoramic video capture using an iPhone (Kogeto Dot), and it is very low cost (~$12) due to mass production. These together make the combination of PAL and smartphone an ideal solution as a portable, high-performance, and low-cost imaging platform for endoscopic applications, as long as the illumination part can be well-addressed.

In this chapter, we introduce a panoramic endoscope, named the PanCam, for the fast imaging of the whole anal canal. The PanCam utilizes a PAL for getting the 360° panoramic view of the anal canal, and a camera sensor connected with a smart phone for high-resolution image capture and reconstruction. We also developed a novel illumination method by coupling light to the outer tube of the PanCam so that all the anal canal tissues within the FOV can be uniformly illuminated.

The structure of this chapter is as follows. We will first describe the system setup of the PanCam. We will then present the illumination method for the PanCam. Next we will introduce the image reconstruction algorithm. Then, we will establish the resolution and FOV of the PanCam. Finally, we will show a demonstrative imaging result of a tissue sample.

5.2 The imaging principle of panoramic annular lens

A typical PAL imaging system is shown in Figure 5.1. Among the four optical surfaces on PAL, 1 and 4 are refractive, and 2 and 3 are reflective. If we consider the object as a 360° cylindrical surface around the PAL, it can then be transformed onto a 2D flat surface with an annular shape on the image plane. This projection is named the flat cylinder perspective (FCP). The image is formed inside the PAL, and it can be relayed to the image sensor by using an extra relay lens. As an example in Figure 5.1, Object A is projected to A' and B is project to B' on the image plane where a CCD/CMOS sensor chip is placed. α is the blind area that the PAL cannot image, and β is the field angle of the PAL.

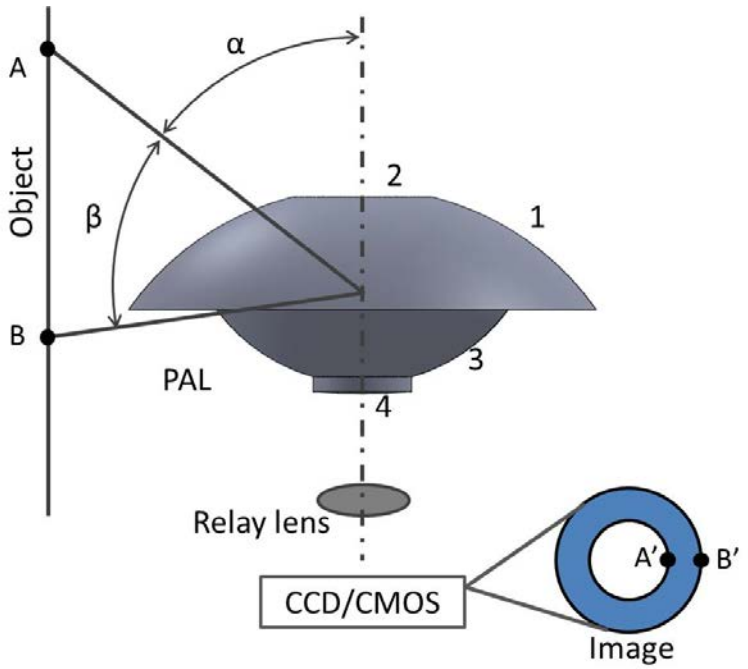

Figure 5.1. The panoramic annular lens (PAL) imaging system. Object A and B on a cylindrical surface around the PAL can be projected onto an annular image below the PAL.

Figure 5.2 illustrates the light ray tracing inside the PAL using Zemax. The parameters are from the patent of Kogeto Dot [14], and the missing data were given an estimated value. We can observe that the rays from different angles enter the PAL from the refractive surface 1, are then are reflected by surface 2 and reflected again by surface 3, and finally exit from refractive surface 4. There is also a relay lens set (RL) to transfer the intermediate

image to the exit pupil (EP) so that it can further be imaged to the camera sensor through the camera's lenses.

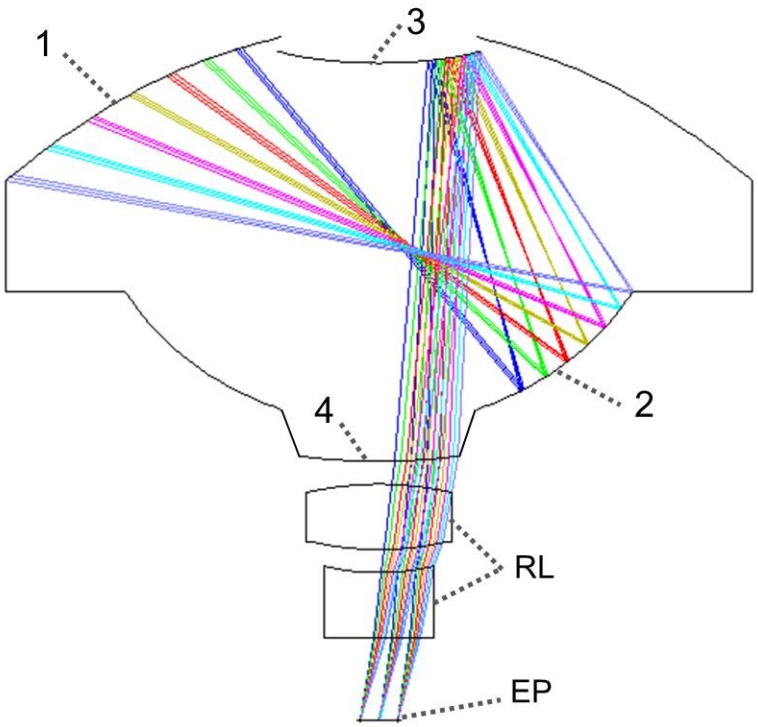

Figure 5.2. The ray tracing of a PAL. The rays from different angles are refracted and reflected by surface 1-4 of the PAL, then pass through the relay lens set (RL) to arrive at the exit pupil (EP).

5.3 System setup of the PanCam

The PanCam endoscope system we proposed is shown in Figure 5.3. It consists of a PAL with its relay lens, a LED light source, and a camera module disassembled from a smartphone (Samsung Galaxy S4). All these components are packaged inside a transparent tube. The camera module is connected backed to the smartphone using a customized extension flexible flat cable (FFC). During the imaging process, the light source uniformly illuminates the sample attached 360° around the cylindrical tube, and the PAL projects the sample into an annular image, which is then captured by the camera module and recorded by the smartphone. In this section we will discuss the illuminator, the extension FFC, and the integrated PanCam system in detail.

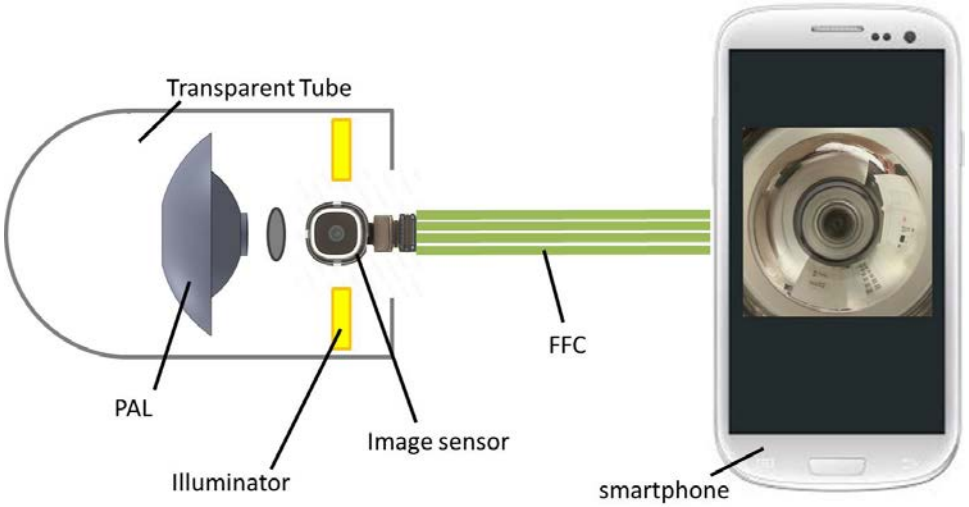

Figure 5.3. The design of the PanCam system. The probe part consists of a PAL a camera module, and an illuminator, which are all packaged in a transparent tube. The camera module is connected to the smartphone by using an extension flexible flat cable (FFC).

5.3.1 Illumination

The basic principle of our illumination method for the PanCam can be easily seen from a light decoration design, as shown in Figure 5.4. If a light source is coupled to a transparent tube, the light will keep traveling inside the tube without leaking out until it hits the end of the tube. This is due to the effect of total internal reflection (TIR), since the medium inside and outside the tube is air, which has a lower refractive index than the tube material. Interestingly, if we attach to the tube with a medium that has a similar refractive index, the light will leak out and the medium will be illuminated. In this way, if we couple our light source directly to the transparent tube in our PanCam probe, we will be able to illuminate all the tissues in contact with the tube.

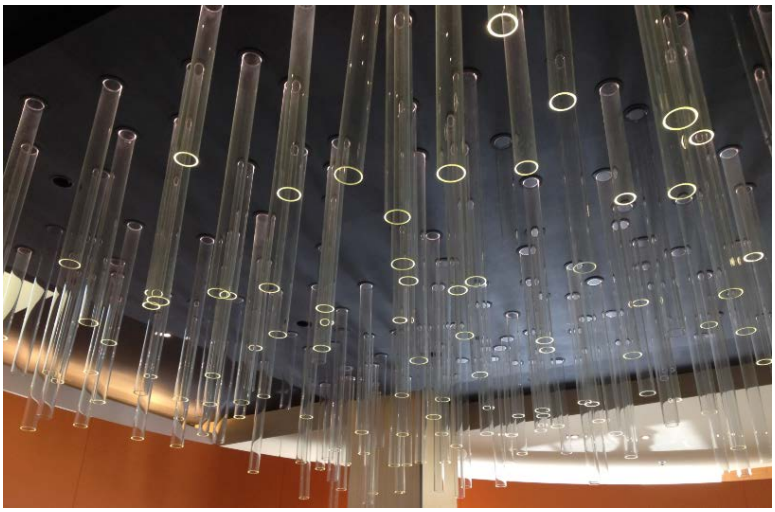

Figure 5.4. A design of transparent tubes as decoration light sources. Light can travel inside the tubes due to total internal reflection (TIR). Photo courtesy of Gia Dong.

Based on this idea, we designed the structure of our illuminator as illustrated in Figure 5.5a. The light source (e.g., LED) is uniformly distributed in a ring shape (Figure 5.5b,c), coupling light into the transparent tube. If there is nothing attached to the tube, the coupled light will be trapped inside the tube. When the sample is attached to the tube the refractive index difference will decrease so the light will leak out of the tube to illuminate the sample.

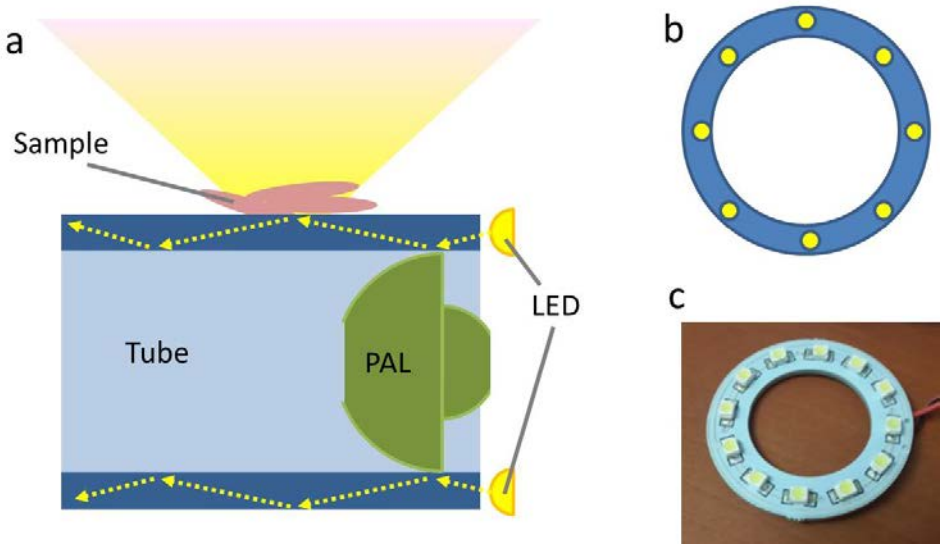

Figure 5.5. The illuminator design. (a) The illumination principle. (b) The design of the LED ring. Multiple LEDs are arranged uniformly in a circle. (c) A photo of the LED ring.

Same as the AnCam (in Chapter 4), the PanCam also needs to be coated with a water-based lubrication before it is inserted into the anal canal. This is in our favor, since this water-based lubrication can also act as our illumination medium. For this purpose, we verified the refractive index of K-Y jelly (Johnson & Johnson), which is a typical lubricant in our experiment. The measurement was conducted using a gemological refractometer (ADE Advanced Optics), with the result shown in Figure 5.6. The measured refractive index is n_{KY}=1.36 with an accuracy of 0.01. Therefore, we chose poly(methyl methacrylate) (PMMA) as the tube material, since its refractive index (n_{PMMA}=1.49) is closer to K-Y jelly compared with polycarbonate (PC) tubes (n_{PC}=1.58) and thus can provide a brighter illumination.

Figure 5.6. Refractive index measurement of K-Y jelly. Pointed by the arrow, the refractive index was measured to be $n_{K\text{-}Y}$=1.36.

The uniformity of this illumination method was measured by coating K-Y jelly around the PMMA tube of the PanCam, then wrapping a white paper around the tube. The raw image captured by the PanCam is shown in Figure 5.7a, and a cross-section of the intensity distribution in radial direction is shown in Figure 5.7b. This demonstrates that the illumination is very uniform throughout the whole imaging area, with a maximum fluctuation of ~6%.

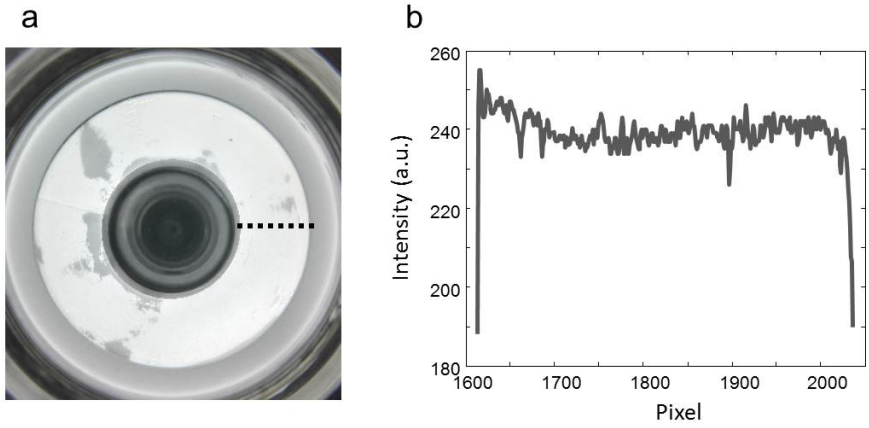

Figure 5.7 The illumination uniformity test. (a) The raw image of a white paper attached to the tube surface of the AnCam. The dashed line lables a cross-section. (b) The intensity distribution of the cross-section in (a).

5.3.2 Customized Flex Cable

Since the camera module needs to be placed within the probe, an extension cable is essential for its connection with the smartphone to allow it to work outside the phone. Here we designed a FFC in OrCAD, and made it fabricated from Tech-Etch. In order to connect to the Galaxy S4's rear camera sensor, the FFC was designed to have a length of 48.7 mm, a width of 9.3 mm, and a thickness of 0.8 mm. Its technical parameters are listed in Table 5.1. The FFC design is illustrated in Figure 5.8a─d. It has two circuit layers (Figure 5.8a,b), and there is one metal pad layer on each circuit layer, with through holes for interlayer connection (Figure 5.8c). Two plug connectors were carefully soldered onto the FFC, and the final FFC prototype is shown in Figure 5.8e.

Table 5.1. Parameters of the customized flexible flat cable (FFC).

name	Value
Wire width	0.2 mm
Pad size	0.7 mm × 0.18 mm
Through-hole diameter	0.3 mm
Insulator thickness	0.5 mil
Copper thickness	0.7 mil (0.5 oz/ft^2 copper weight)

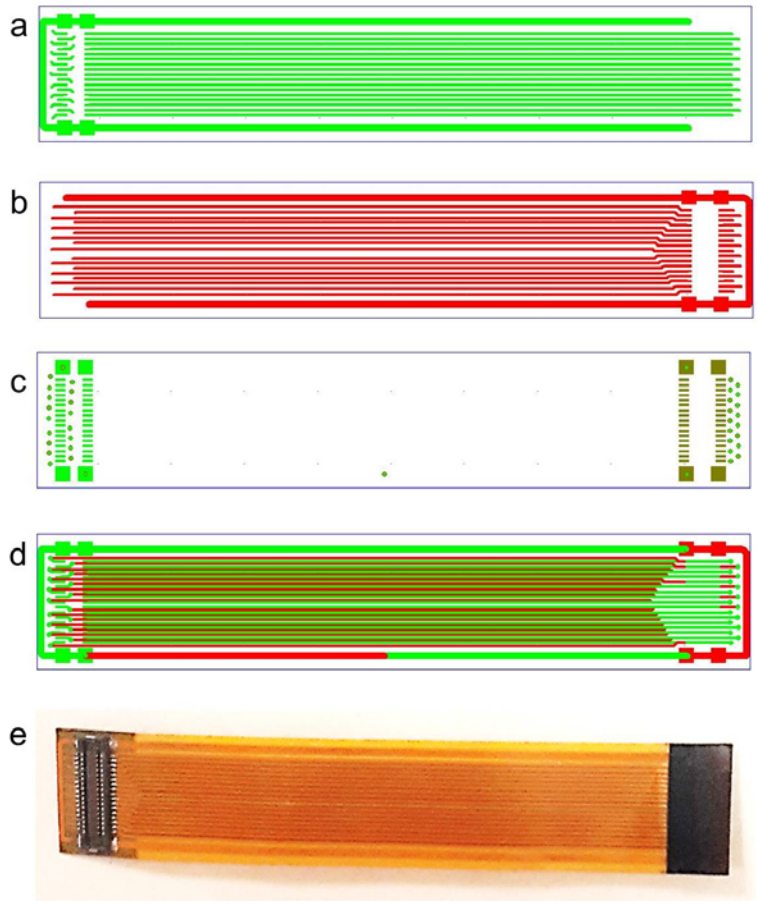

Figure 5.8. The design and fabrication of the FFC. (a) The first circuit layer. (b) The second circuit layer. (c) The metal pad layer and through-hole layer. (d) All the layers merged together. (e) The fabricated FFC with two plug connectors soldered.

5.3.3 The PanCam system

After fabricating all the needed components, the PanCam system can be assembled as shown in Figure 5.9. The PMMA tube has an outer diameter of 38.1 mm, an inner diameter of 31.8 mm, and a length of 50 mm. The tip of the tube is made of medical-grade silicone following the same method as the AnCam in Chapter 4.

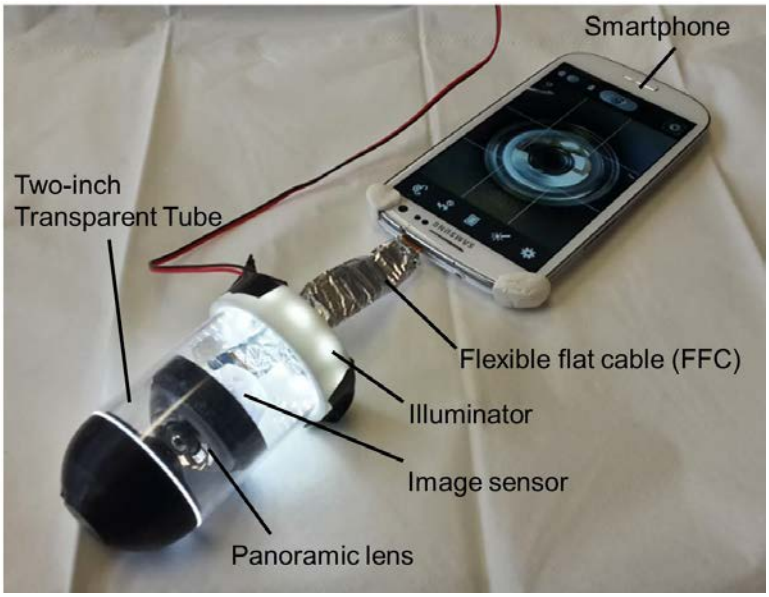

Figure 5.9. The assembled PanCam system prototype.

5.4 Image reconstruction

An annular image is collected by the CMOS sensor, which contains all the information of the sample on the cylindrical surface but with distortion. An algorithm is needed to correct all the distortions and reconstruct the annular image back to a rectangular image that correctly recovers the sample in 360°. This reconstruction includes the distortion removal both in the azimuthal and radial direction of the annular image. To address this, we developed a panorama reconstruction algorithm in MATLAB, with the flow chart illustrated in Figure 5.10.

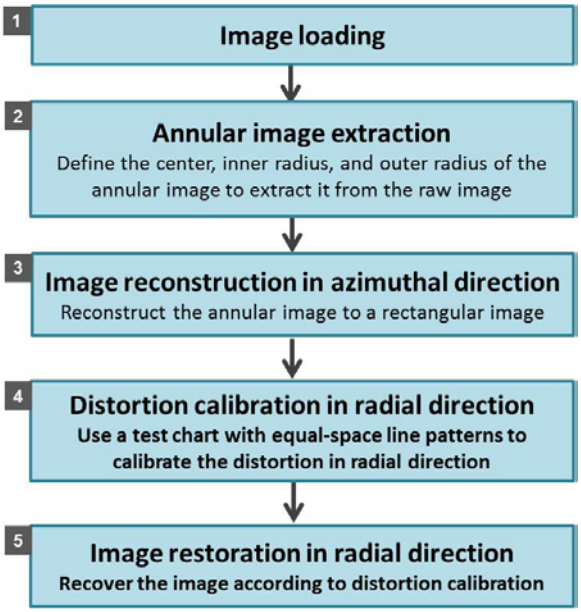

Figure 5.10. The flow chart of two reconstruction algorithms.

This algorithm has five steps, and is described as follows:

1. Image loading

A raw image captured by the PanCam is loaded into the program.

2. Annular image extraction

After loading the raw image, the annular image containing the panorama information is extracted by defining the center, inner radius, and outer radius, as shown in Figure 5.11. These parameters can be found simply by drawing two concentric rings in the raw image to make them match the inner and outer borders of the annular image. The radii of these rings define the inner and outer radius of the annular image, and the center of these rings defines the center of the annular image. It is worth noting that these parameters only need to be calculated once. Since the camera module is fixed with the PAL, these parameters will always be consistent for the same PanCam prototype.

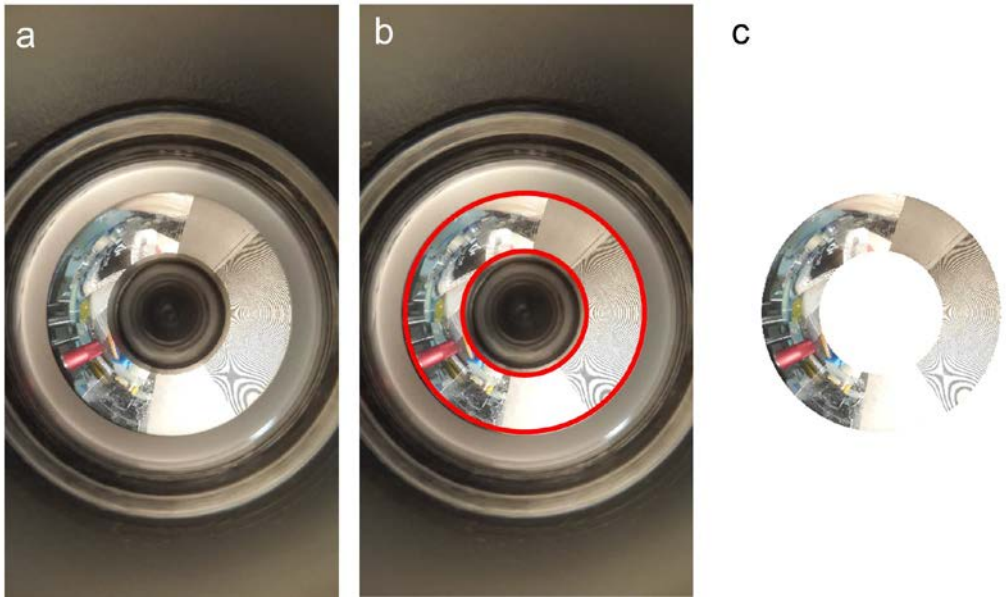

Figure 5.11. Annular image extraction process. (a) The raw image directly captured by the PanCam. (b) Two concentric rings (red) were placed in the raw image to match the inner and outer borders of the annular image. They define the center and the inner and outer radii of the annular image. (c) The annular image can then be extracted by using the center coordinates and setting the inner and outer radii.

3. Image reconstruction in the azimuthal direction

Then the annular image can be reconstructed in azimuthal direction by converting the annular shape into a rectangular shape, as shown in Figure 5.12. For a point P(x,y) in the annular image (Figure 5.12a), its projection relationship with the point P'(x',y') in the rectangular image (Figure 5.12b) can be described as:

$$\begin{cases} x_p = y'_p \cdot \cos(x_p' \cdot \Delta\theta) \\ y_p = y'_p \cdot \sin(x_p' \cdot \Delta\theta) \end{cases} \quad (5\text{—}1)$$

where $\Delta\theta$ is a constant value to make sure that $x_{p\,max}' \cdot \Delta\theta = 2\pi$.

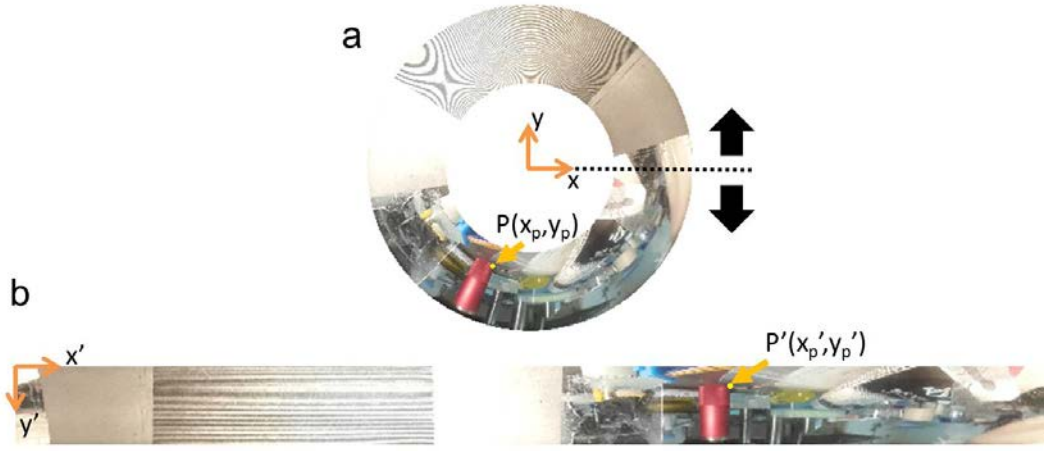

Figure 5.12. Image reconstruction in the azimuthal direction. This step converts the annular shape (a) into the rectangular shape (b).

4. Distortion calibration in the radial direction

After image reconstruction in azimuthal direction, the amount of distortion in the radial direction is calibrated using a test chart printed on a transparency film, as shown in Figure 5.13. The test chart has 1D lines with 170 μm equal separation (Figure 5.13a), and is attached to the tube surface of the PanCam to obtain the raw image (Figure 5.13b). After the azimuthal image reconstruction in Step 3, it is noticeable that the line separation becomes non-uniform (Figure 5.13c) due to the distortion in radial direction. If we can reconstruct these lines back to equal separation again, the distortion will be well-calibrated. The positions of these lines can be extracted by detecting the local minima of intensities (Figure 5.13d) [15], then the images between every two lines can be resized accordingly to make sure that all the lines have equal separation distance. In addition, the aspect ratio of the image can also be correctly recovered in this step. The recovered image of the test chart is shown in Figure 5.13e. The equivalent pixel size of the final reconstructed image is calculated to be 23 μm, by noticing that the perimeter of the tube (120 mm) is also the width of the reconstructed image (5228 pixels).

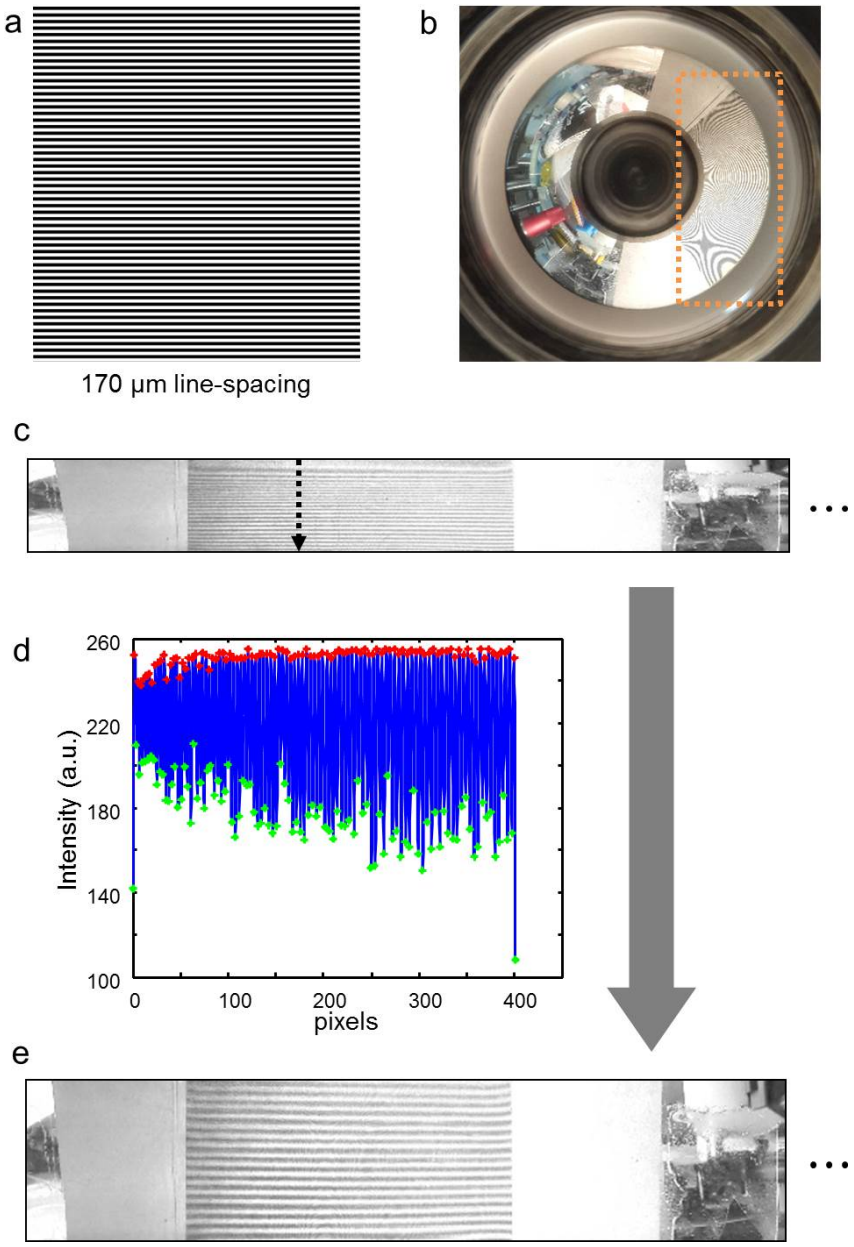

Figure 5.13. Image restoration in the radial direction. (a) The 1D line pattern in the test chart. (b) The raw image of the test chart (yellow rectangle) captured by the PanCam. (c) After the reconstruction in azimuthal direction, the lines in the image are still not uniformly distributed due to the radial distortion. (d) A cross-section of the line pattern is analyzed (dashed arrow in (c)) to extract the position of each line. (e) The spacing between each line pair is resized to make sure that all the lines have equal separation distance. As the same time the aspect ratio is also correctly recovered.

5. Image reconstruction in radial direction

The calibration parameters of the test chart in Step 4 are used in the image of the real samples to complete the reconstruction process in radial direction. After this step, the distortions in both azimuthal and radial directions are removed.

5.5 Resolution and field-of-view

To define the resolution limit of the PanCam, a transparency film containing an array of Group 2&3 patterns from the 1951 USAF resolution test chart was designed (Figure 5.14a). The tube surface of the PanCam was coated with K-Y jelly and then wrapped by the transparency film. An extra layer of K-Y jelly was then coated onto the transparency film and a white paper was attached outside to provide a white background. The raw annular image is shown in Figure 5.14b, and the reconstructed panoramic image is shown in Figure 5.14c. From all the resolution patterns, we picked five regions along the azimuthal direction (d─i) for analysis, due to the symmetrical nature of the annular image. The zoom-in images of these five regions are shown in Figure 5.14d─i. Each region can be further divided into eight sub-regions along the radial direction, as labeled by number 1─8 from inside to outside (Figure 5.14d). The measured resolution in each sub-region is defined as the minimum discernible line spacing and is illustrated in Figure 5.14j. The resolution of the PanCam is not very uniform across its FOV, ranging from 100 μm to 140 μm. The resolution is the worst near the outer border of the annular image, due to the aberration of the PAL. In conclusion, we can claim that our PanCam has a resolution of better than 140 μm. Noticing that the equivalent pixel size for the reconstructed PanCam image is 23 μm, our established resolution also satisfies the Nyquist sampling theorem. The FOV of the PanCam was measured to be 18 mm × 120 mm in a separate experiment.

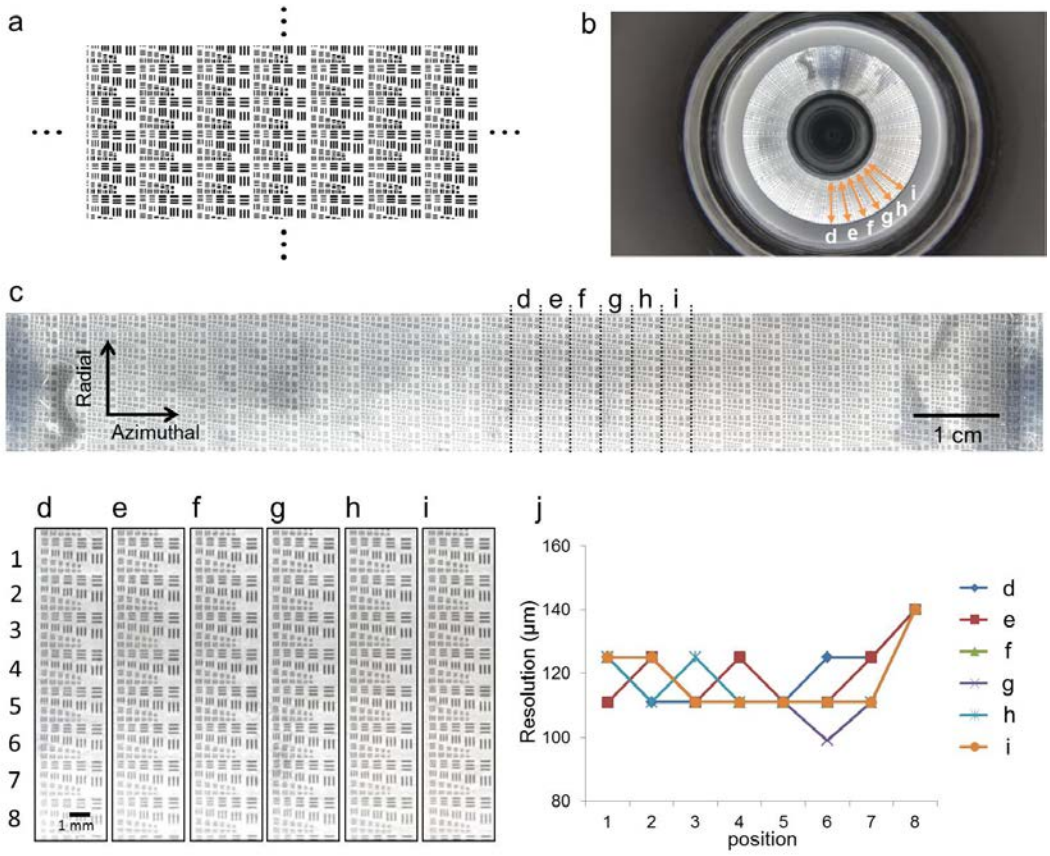

Figure 5.14. The resolution measurement of the PanCam. (a) The design of the transparency film containing an array of Group 2&3 patterns from the 1951 USAF resolution test chart. (b) The raw annular image of the resolution target. Six regions (d─i) are selected for analysis. (c) The reconstructed panoramic image. (d─i) The zoomed-in images of the selected regions. Sub-regions along the radial direction are labeled by number 1─8 from inside to outside (j) The measured resolution of the six regions.

5.6 Imaging result of a tissue sample

As a demonstration, we used the PanCam to image a piece of beef tongue tissue sample. Both the PanCam tube and the tissue were coated with K-Y jelly, and attached together for image acquisition. The reconstructed panoramic image is shown in Figure 5.15a. A region of the sample was stained by a marker pen and zoomed in in Figure 5.15b. For comparison, the same tissue was imaged by a standard colposcope (Olympus OCS-3) under 12× magnification (Figure 5.15c), and the same zoomed-in region is shown in Figure 5.15d. Three spots with 100─200 μm diameters are clearly discernible in both systems (Figure

5.15b,d). The tissue sample shows up as different colors in the two systems, due to the different light sources they use.

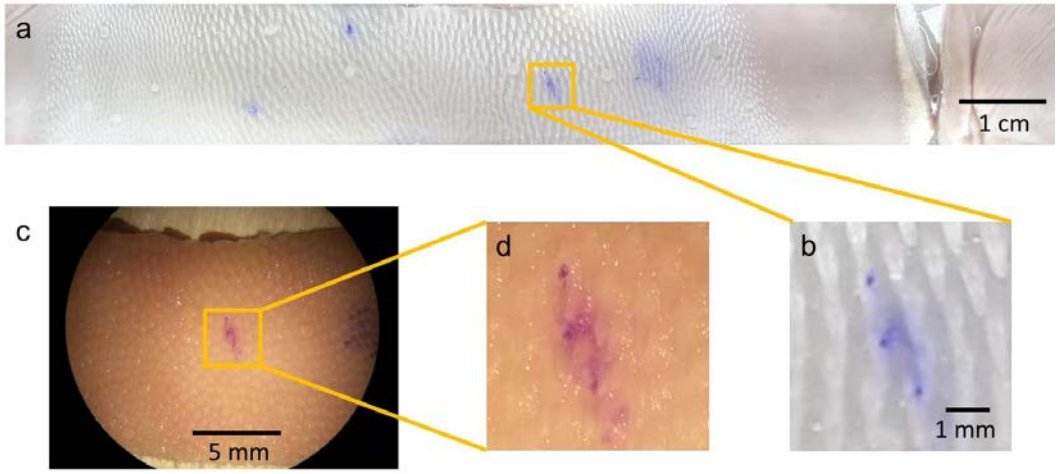

Figure 5.15. Imaging of a beef tongue tissue. (a) The reconstructed panoramic image from the PanCam. (b) A zoomed-in image of (a), showing three stained spots. (c) The colposcopic image under 12× magnification. (d) A zoomed-in image of (c), showing the same three spots as in (b).

5.7 Discussion

Typically the anal canal region has a length of ~ 2─4 cm, including squamous mucosa, dentate line, and columns of morgagni. The FOV of our PanCam allows us to capture a length of 1.8 cm at a time, and therefore the whole anal canal can be imaged by our PanCam in one or two shots. In addition, for our current work, we directly used a PAL available from the market to build the proof-of-concept PanCam prototype. In the future we can customize the PAL's optical design to further increase the FOV if needed.

The reconstruction of the distortion-free panoramic image from an annular raw image includes the restoration in both azimuthal and radial direction of the annular image. The reconstruction in the azimuthal direction can be simply achieved by converting the annular shape into the rectangular shape as described in Section 5.3.1. After this step, the panoramic image is still distorted in the radial direction. For reconstruction in the radial direction, there are several existing approaches methods. Gilbert *et al.* and Zhao *et al.*

developed different re-projection equations to correct the distortion [5,16]. However, different PALs may have different distortion distribution and the equation may not be always accurate in general cases. Here we chose another approach that directly measures the amount of distortion using a calibration test chart. Although this approach requires an extra step of calibration, it can guarantee the correct reconstruction as long as we can recover the test chart faithfully. Therefore, using the test chart can be a general solution for calibrating different designs of PALs.

In this chapter, the panoramic image reconstruction was carried out using MATLAB in a computer. For our future work, the whole image processing algorithm can be developed into an application software (app), and installed into the smartphone itself for image processing, so that no desktop/laptop will be needed for the image reconstruction process. For example, we can use Eclipse, an integrated development environment (IDE), for the software development. As a demonstration, an app's user interface is shown in Figure 5.16. The left button switches on the camera to capture the raw annular image of the tissue sample (Figure 5.16a). The middle button guides the user to the photo album to select the target raw image (Figure 5.16b). The right button reconstructs the selected raw image in both the azimuthal and radial direction to recover it to the final panoramic image, and saves it to the photo album (Figure 5.16c). We believe adding this feature can help to make the PanCam an ideal solution to the problem of finding a portable, high-performance, and low-cost imaging platform.

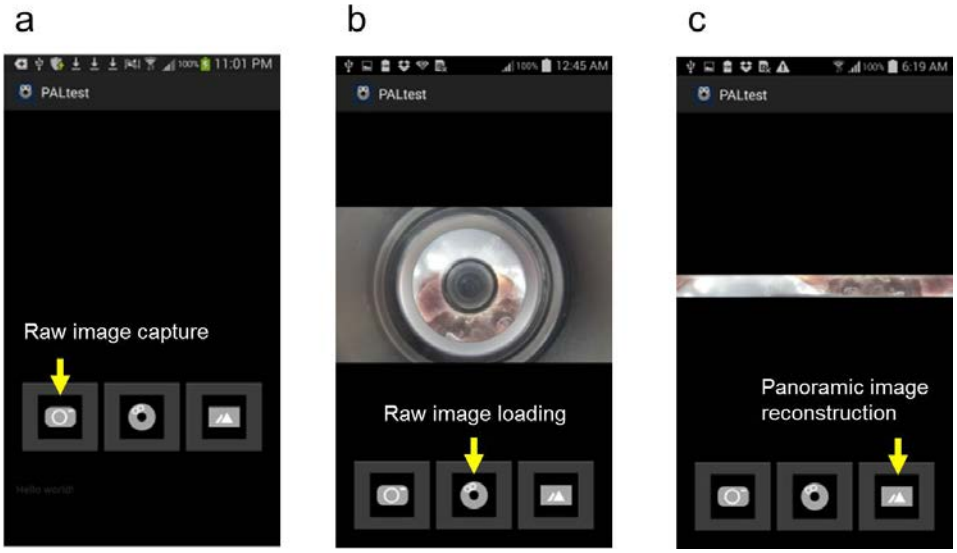

Figure 5.16. The image reconstruction software in Android system. (a) The left button switches on the camera to capture the raw annular image. (b) The middle button guides the user to select the captured annular image. (c) The right button reconstructs the annular image to the final panoramic image, and saves it to the photo album.

5.8 Conclusion

In this chapter we developed a novel smartphone-based panoramic endoscope, named the PanCam. The PanCam consists of a panoramic annular lens (PAL) for getting the 360° panoramic view of the tissue, a light source for providing uniform illumination, and a camera module connected with a smart phone for image capture, providing a resolution of 100─140 μm. The PanCam has several advantages. It captures the panorama of all the tissues around it with one single shot, making wide FOV video-rate time-lapse imaging of live tissue possible, which can also be useful for telemedicine and remote surgery. The system is low-cost, so that the endoscope probe can even be made disposable to avoid potential cross-contamination. The integration with the smartphone makes the whole system very compact and suitable for point-of-care applications. Finally, due to its compact and easily-scalable size, we believe the PanCam can potentially find broad applications for imaging multiple cavities inside the human body (including anal canal, rectum, and esophagus) for the screening and early diagnosis of cancer.

REFERENCES

1. M. Ou-Yang and W. D. Jeng, "Design and analysis of radial imaging capsule endoscope (RICE) system," Opt Express **19**, 4369-4383 (2011).
2. R. C. Wang, M. J. Deen, D. Armstrong, and Q. Fang, "Development of a catadioptric endoscope objective with forward and side views," J Biomed Opt **16**, 066015 (2011).
3. R. Sagawa, T. Echigo, K. Yagi, M. Shiba, K. Higuchi, T. Arakawa, and Y. Yagi, "Omnidirectional vision attachment for medical endoscopes," Proceedings of the 8th Workshop on Omnidirectional Vision (2008).
4. P. Greguss, "The Tube Peeper - a New Concept in Endoscopy," Opt Laser Technol **17**, 41-45 (1985).
5. L. Zhao, J. Bai, X. Liu, and H. Li, "An improved image restoration method for the high definition panoramic camera system," Opt Laser Eng **47**, 982-989 (2009).
6. I. Kopilovic, B. Vagvolgyi, and T. Sziranyi, "Application of panoramic annular lens for motion analysis tasks: Surveillance and smoke detection," Int C Patt Recog, 714-717 (2000).
7. D. Hui, M. Zhang, Z. Geng, Y. Zhang, J. Duan, A. Shi, L. Hui, Q. Fang, and Y. Liu, "Designs for high performance PAL-based imaging systems," Appl Opt **51**, 5310-5317 (2012).
8. J. A. Gilbert, D. R. Matthys, and C. M. Lindner, "Endoscopic Inspection and Measurement," P Soc Photo-Opt Ins **1771**, 106-112 (1993).
9. Z. Huang, J. Bai, and X. Y. Hou, "Design of panoramic stereo imaging with single optical system," Opt Express **20**, 6085-6096 (2012).
10. D. R. Matthys, J. A. Gilbert, and P. Greguss, "Endoscopic Measurement Using Radial Metrology with Digital Correlation," Opt Eng **30**, 1455-1460 (1991).
11. J. L. Linder, "Panoramic refracting optic," U.S. Patent, US6424470 (2002).
12. A. S. Mosa, I. Yoo, and L. Sheets, "A systematic review of healthcare applications for smartphones," BMC Med Inform Decis Mak **12**, 67 (2012).
13. A. Ozcan, "Mobile phones democratize and cultivate next-generation imaging, diagnostics and measurement tools," Lab Chip **14**, 3187-3194 (2014).
14. Jeff Glasse, "Methods and apparatus for panoramic afocal image capture," U.S. Patent, US20130194382 (2012).
15. http://www.mathworks.com/matlabcentral/fileexchange/12275-extrema-m--extrema2-m.
16. J.A. Gilbert, and K.R. Biszick, "Panoramic projection system using a panoramic annular lens," SEM Annual Conference & Exposition on Experimental and Applied Mechanics (2007).

Chapter 6

SUMMARY

In this thesis, we have presented several novel wide field-of-view (FOV) microscopic imaging systems to address the needs in high-throughput screening for biological research and clinical diagnosis.

1. We applied the ePetri Dish, a wide FOV on-chip bright-field microscope, for plaque analysis of murine norovirus 1 (MNV-1) over a wide FOV of 6 mm × 4 mm at 30 min intervals. We implemented a customized image-processing program containing a density-based clustering algorithm to identify plaques at a very early stage when they only contain several dead cells. Finally, we demonstrated the capabilities of the ePetri in viral titer count, tracking of plaque growth, and the evaluation of antiviral drugs. To our knowledge, this is the first time viral plaques can be recognized and tracked at the level of individual cell death event, due to the high-resolution-wide-FOV capability of the ePetri and the implementation of the clustering algorithm. We expect that the ePetri device can be used for many applications in virology such as the study of virus behavior and the discovery of new antiviral drugs.

2. We developed a wide FOV on-chip fluorescence imaging technique, the Talbot microscope, for high-throughput live cell imaging. The Talbot microscope takes advantage of the Talbot effect and can generate a focal spot array at the Talbot distance to scan the fluorescence samples directly on-chip at a resolution of 1.2 μm and an FOV of ~13 mm^2. We demonstrated its capability by imaging various fluorescence-stained and live green fluorescent protein (GFP)-coded cell samples. We further upgraded the Talbot microscope for the long-term time-lapse imaging of cell cultures within incubators, and named it the Talbot fluorescence ePetri. As demonstration, we obtained time-lapse images of live GFP cells, and we also employed the system to analyze the cells' dynamic response to an anticancer drug. To our knowledge, the Talbot fluorescence ePetry system is the first demonstration of automated wide FOV and high-resolution fluorescence imaging for longitudinal studies that does not rely on conventional microscopy methods. We believe the Talbot microscope can also find

significant applications in many emerging fields, such as tissue engineering and stem cell differentiation, where the longitudinal study of a large number of living samples is needed.

3. We developed a novel wide FOV scanning endoscope, named the AnCam, for the high-throughput screening of the whole anal canal tissue. The AnCam is based on contact image sensor (CIS) technology used in commercialized business card scanners, and can capture the whole image of the anal canal within 10 seconds with a resolution of 89 μm, a maximum FOV of 100 mm × 120 mm, and a depth-of-field (DOF) of 0.65 mm at 5.9 line pairs per mm (lp/mm). We demonstrated the performance of the AnCam by imaging the entire anal canal of an animal model and time-lapse tracking the dynamics of acetowhite testing. Finally, we upgraded the AnCam prototype with biocompatible materials for the anal canal screening of real patients. To our knowledge, the AnCam is the first imaging device for capturing the whole circumferential inner cylindrical surface of the whole anal canal. The overall imaging performance, the reproducibility of the images, and the ease-of-use together make the AnCam a highly attractive potential alternative to current imaging modalities of the anal canal.

4. We developed a panoramic endoscope, named the PanCam, to further enhance the speed of wide FOV endoscopic imaging. The PanCam is based on a smartphone platform integrated with a panoramic annular lens (PAL), and can capture a FOV of 18 mm × 120 mm within a single shot with 100─140 μm resolution. In addition, we developed a novel illumination method to ensure that all the tissues within the PanCam's FOV are uniformly illuminated. The fast imaging nature of the PanCam makes the wide FOV video-rate imaging of live tissue possible. In addition, the PanCam has a compact and easily-scalable size, and therefore we believe it can potentially find broad applications for imaging multiple cavities inside human body (including anal canal, rectum, and esophagus) for the screening and early diagnosis of cancer.

In summary, the wide FOV microscopes and endoscopes presented in this thesis have demonstrated their capabilities in longitudinal imaging of living organisms, on the scale of viral plaques to live cells and tissues. They can potentially have high impact in high-

throughput imaging in life sciences and medical diagnosis. In addition, all these systems are compact, low-cost, and available for mass-production, and therefore can also be quite suitable for point-of-care and telemedicine applications.